Dissertation

submitted to the

Combined Faculty of Mathematics, Engineering and Natural Sciences
of the Ruperto-Carola University of Heidelberg, Germany

for the degree of

Doctor of Natural Sciences

Put forward by

Bruno Maximilian Faigle-Cedzich

born in: Nürnberg, Germany

Oral examination: July 5th, 2022

Towards understanding the dimensional BCS-BEC crossover and its spectral properties

Referees: Prof. Dr. Jan M. Pawlowski
Prof. Dr. Tilman Enss

Towards understanding the dimensional BCS-BEC crossover and its spectral properties

In this thesis we investigate several aspects of ultracold Fermi gases within the framework of the functional renormalisation group (fRG). The first part concerns the determination of the thermodynamics and the phase structure of a Fermi gas within a dimensional crossover from three to two dimensions over the whole BCS-BEC crossover. Particular focus is put on the determination of the finite temperature phase diagram for different confinement which is then compared to recent experimental observations. In the second part, we perform an analytical continuation of the two-point functions in Euclidean space to real times. This allows us to gain knowledge about the spectral functions within the three-dimensional BCS-BEC crossover en route to obtaining transport properties of ultracold quantum gases. The third part is devoted to the access to quantitative precision within the fRG approach. We employ an approach that utilises higher order density fluctuations as the fundamental building blocks which circumvents the fine-tuning problem of the density on the microscopic level. We primarily compute the equation of state and the gap over the whole range of BEC-BCS crossover at vanishing temperature. The very good quantitative agreement with recent experimental results, particularly at unitarity, thus shows the quantitative reliability of the fRG framework.

Fortschritt zum Verständnis des dimensionalen BCS-BEC-Crossovers und seiner spektralen Eigenschaften

Mit dieser Arbeit untersuchen wir verschiedene Aspekte von ultrakalten Fermi-Gasen im Rahmen der funktionalen Renormierungsgruppe (fRG) und versuchen deren Verständnis zu erweitern. Der erste Teil beschäftigt sich mit der Bestimmung der Thermodynamik und der Phasenstruktur eines Fermi-Gases innerhalb eines dimensionellen Crossovers von drei auf zwei Dimensionen über den gesamten BCS-BEC-Crossover. Besonderes Augenmerk legen wir auf die Bestimmung des Phasendiagramms bei endlicher Temperatur für verschiedene Ausdehnungen, was mit experimentellen Beobachtungen verglichen wird. Im zweiten Teil führen wir eine analytische Fortsetzung der Zwei-Punkt-Funktionen im euklidischen Raum zu reelen Zeiten durch. Dies ermöglicht es, Erkenntnisse über Spektralfunktionen im dreidimensionalen BCS-BEC-Übergang als Zwischenschritt zu Transporteigenschaften zu gewinnen. Der dritte Teil ist der Bestimmung von Observablen quantitativer Präzision innerhalb des fRG-Ansatzes gewidmet. Wir verwenden einen Ansatz, der Dichtefluktuationen höherer Ordnung nutzt, um ein Fine-Tuning-Problem der Dichte auf mikroskopischer Ebene zu umgehen. Wir berechnen die Zustandsgleichung und die Gap über den gesamten BEC-BCS-Crossover bei verschwindender Temperatur und zeigen bei guter Übereinstimmung mit experimentellen Daten die quantitative Zuverlässigkeit des fRG-Ansatzes.

Contents

CHAPTER 1

Introduction

Ultracold quantum gases provide a rich field exhibiting a plethora of phenomena, often times going beyond the expected.The theoretical prediction of Bose-Einstein condensation by Satyendra Bose und Albert Einstein in the 1920s [4, 5] and both the experimental discovery of superfluidity in ^{4}He by Pyotr Kapitza, John Allen and Don Misener [6, 7] and the phenomenon of superconductivity by Heike Kamerlingh Onnes [8] laid the foundation for a series of experimental discoveries. These necessitated new theoretical understanding and accompanying frameworks in the field of many-body physics, sometimes coming to fruit with a rather long delay. For example, the insight by John Bardeen, Leon Cooper and Robert Schrieffer that superconductivity can be seen as a Bose-Einstein condensation of loosely bound fermions and the so-called BCS-theory came decades after its experimental discovery in 1957 [9]. With the realisation of a Bose-Einstein condensate in an ultracold trapped dilute gas of bosonic alkali atoms in 1995 [10–12] and likewise of its fermionic counterpart in 1999 [13–15], a new playground for investigating the fundamental laws of nature was born.

1.1 Motivation

Due to their near perfect tunability and experimental control, ultracold quantum gases provide a perfect test-bed for gaining understanding of the physical principles behind many effects at the interface of few- and many-body physics. A key element is the achievement of sufficiently low temperatures for quantum degeneracy where the behaviour of the particles is no longer determined by classical physics. One rather has to deal with quantum many-body phenomena, such as Bose-Einstein condensation. For the highly controlled experimental realisation, a couple of accomplishments were necessary, namely trapping atoms in a magnetic or optical trap [16], pre-cooling with laser beams [17], a subsequent evaporative cooling step [18] and imaging the gas in-situ or in momentum space after an expansion of the gas.

From a theoretical point of view the appeal of ultracold quantum gases lies in their low-energy nature. At these very low temperatures the complex interatomic potential can be successfully modelled by point-like interactions between the particles. As a consequence, ultracold atom systems can be effectively described by a simple many-body Hamiltonian with contact interactions, irrespective of their atomic and sub-atomic details.

A particularly neat property of ultracold quantum gases is the possibility of tuning both the interactions between the individual atoms, as well as their external trapping potential. This allows for creating complex systems with full control on their properties and interactions. For example, a standing wave of light, using counter-propagating laser beams, induces a conservative periodic optical lattice [19]. The shape of the induced periodic potential together with its depth and the interactions between the particles, attracted to the valleys of the potential, can be changed in a highly controlled way. This allows to emulate ionic crystals and to study condensed matter systems modelled through a regular lattice of ions, such as Hubbard model physics [20, 21]. An advantage compared to, for example, solid-state systems is the absence of unwanted impurities, making for a very clean working sample.

As an alternative to optical lattices the ability to tune the interactions between the atoms in an ultracold quantum gas is introduced by means of a so-called Feshbach resonance. In a two-body scattering process, the incoming and outgoing states have a different spin configuration such that an external magnetic field couples differently to their distinct magnetic moments. The Feshbach resonance can then be used to tune the scattering length, which sets the rate of scattering processes. Specifically when considering a gas of two-component ultracold fermions, the Feshbach resonance allows to tune from a weakly interacting gas of spatially well-separated individual fermions to strong attractive interactions where fermion pairs become tightly bound. In this situation of strong attraction, for a large positive scattering length, the pairs are much smaller than the interparticle spacing, essentially constituting a bosonic dimer. For a weak attraction the fermionic system condenses into the superfluid state via the formation of Cooper pairs in the BCS picture, while in the case of bosonic dimers the superfluid state is reached via Bose-Einstein condensation. It turns out that this evolution between the two extremes is a smooth transition, coining the term BCS-BEC crossover, as proposed in [22, 23]. Its importance lies in the fact that the entire range between the previously disconnected limits of BCS- and BEC-physics can be investigated by the turn of a knob.

The BCS-BEC crossover smoothly interpolates between a weakly interacting gas of fermions over a strongly correlated region to a region of weakly interacting bosonic dimers. For a three-dimensional system at the centre of the crossover, i.e. for a diverging three-

dimensional scattering length, a scale invariant universal system can be found. This so-called unitarity limit is of great interest, since it allows to study strongly correlated fermion matter, as relevant for a range of physical systems from electrons in metals to neutron stars [24], with ultracold atoms. All thermodynamic quantities become universal leaving only a single remaining length scale, the (inverse) Fermi momentum. As a consequence, the ground state energy is proportional to the energy of the free Fermi gas at the same density with a proportionality factor called the Bertsch parameter [25, 26]. All density derivatives of the energy, e.g. the chemical potential, the pressure, or the speed of sound, only depend on the universal Bertsch parameter. Its accurate determination has led to a great undertaking in both experiment and theory [27–34].

At the same time, the strong correlations within the BCS-BEC crossover call for a non-perturbative theoretical framework which is able to capture the rich phase structure. One such theoretical method is given by the non-perturbative functional renormalisation group (fRG) [35–44]. Built around the functional integral formalism of quantum field theories it provides a tool to describe the scale dependent evolution of effective actions, thereby including thermal and quantum fluctuations. This evolution is described by a flow equation, first proposed by Christof Wetterich [35], and essentially boils down to a description of running couplings of the theory. It thereby enables us to resolve critical phenomena, as well as the (whole) phase structure and thermodynamic quantities.

The three-dimensional BCS-BEC crossover has been studied extensively within the fRG formalism. Starting with the ground-laying works in [45–49] extensions including particle-hole effects were discussed in [50], the formation of a trion-state was investigated by [51] and further improvements in [52, 53]. Moreover, the investigation of the high momentum behaviour resulting in the Tan contact was carried out by [54], while error estimates within the fRG can be found in [55]. Spin-imbalanced systems and their phases were examined in the works of [56–58]. Extended truncation schemes and their influence on the Bertsch parameter and the critical temperature of an unitary Fermi gas were studied in [59]. For a review concerning fRG techniques applied to the BCS-BEC crossover cf. [43, 60].

Recent progress in trapping techniques for ultracold atomic gases enables investigations beyond the three-dimensional case. With the realisation of strongly anisotropic trapping potentials on the one hand, and one-dimensional optical lattices one the other hand, (quasi-) two-dimensional geometries can be implemented [61, 62]. The investigation of both zero [63–65] as well as finite temperature effects [63, 66–71] is of great relevance, since in reduced dimensions strong correlations and pair fluctuations become more pronounced. Interestingly, having an insufficient degree of anisotropy in the experimental setup leads to a quantum gas restricted to a not well-defined dimensional geometry. Although initially an

unwanted deficiency, it may lead to interesting effects and further insight into the physics of dimensional crossovers. In the context of reduced dimensional systems, the Berezinskii–Kosterlitz–Thouless (BKT) phase transition in (quasi-) two-dimensional systems has been observed in bosonic [66, 69, 72–75], as well as fermionic systems [67, 76] where algebraically, instead of exponentially, decaying correlations have been found.

Apart from the study of static, thermodynamic properties, such as the phase diagram, the determination of transport properties or decay rates within cold atomic systems is of great relevance. Essential quantities for determining transport coefficients are spectral functions, from which one can, for example, obtain (quasi-) particle spectra to characterise collective excitations. In general one can infer real-time information about the physical system using spectral functions.

There are many interesting (novel) directions in the field of ultracold atomic physics, which we did not pursue in this thesis. For example, the study of breathing modes and the accompanied violation of scale invariance [64, 77–86], mixtures of fermions and bosons [87–89], spin- and mass-imbalanced gases [90–95], as well as dipolar quantum gases, cf. e.g. [96] for a review on experimental techniques, are further phenomena worth studying in greater detail. Moreover, the transition from few- to many-body physics can be investigated with cold atoms, as has been shown in recent measurements [97, 98]. Another promising facet of recent interest is the simulation of gauge theories using ultracold atomic systems in the field of quantum simulation, e.g. in [99–103].

In this thesis we expand the knowledge on the three topics outlined above. In particular we study (1) the dependency of the BCS-BEC crossover on dimensionality, (2) spectral functions of ultracold Fermi gases and (3) improve on the quantitative precision of zero temperature observables, including the Bertsch parameter. More concretely, working in the framework of the functional renormalisation group we first extend the investigation of the three-dimensional BCS-BEC crossover to the situation of a dimensional crossover from three to two dimensions. Zero and finite temperature results allow for a qualitative comparison to the experimental data measured in [67]. The second aspect involves the calculation of spectral functions where an analytical continuation from imaginary to real time is performed. Our results serve as a first step to obtain transport coefficients for ultracold quantum gases within the framework of the fRG. Finally, in order to better the quantitative precision within the fRG framework we apply an improved method to obtain the (flow of the) density. We elaborate on an ultraviolet safe way of determining densities via their higher order correlations. Our approach allows us to compute the equation of state and the gap at zero temperature in a quantitative manner.

1.2 Publications

This dissertation was written solely by the author using the referenced sources as indicated in the corresponding passages. The results were obtained together with my collaborators and are either published, or are contained in so far unpublished articles. We do not mark texts and figures taken from these articles explicitly, but refer to them at the beginning of the individual chapters.

The publications are:

[1] **Dimensional crossover in ultracold Fermi gases from Functional Renormalisation**
Bruno M. Faigle-Cedzich, Jan M. Pawlowski, Christof Wetterich
Published in Phys. Rev. A 103, 033320 (2021)
E-Print: arXiv:1910.07365 [cond-mat.quant-gas]
Comment: This article is mainly contained in Chapter 5, yet portions of Chapter 3 and Chapter 4 build on it as well.

[2] **Spectral function of ultracold Fermi gases from functional renormalisation**
Bruno M. Faigle-Cedzich, Jan M. Pawlowski
In preparation.
Comment: This work in preparation is the basis for Chapter 6.

[3] **Towards quantitative precision in ultracold atoms with functional renormalisation**
Bruno M. Faigle-Cedzich, Jan M. Pawlowski
In preparation.
Comment: Chapter 7 relies on this work.

1.3 Outline

This thesis is organised as follows: Chapter 2 and Chapter 3 introduce the basic concepts of ultracold atom physics and functional methods which are relevant for this thesis. We describe the construction of an effective Hamiltonian and after introducing the framework of the functional renormalisation group apply it to our situation of a two-component ultracold Fermi gas. In Chapter 4 the flow equations for a fixed d-dimensional setup and for a confinement from three to two dimensions are derived in general so that they can be easily adopted to other situations and truncation schemes.

The physics of an ultracold Fermi gas in the dimensional crossover from three to two dimensions is reflected on in Chapter 5. Here, we confine the system in the transverse direction by means of periodic boundary conditions and the equation of state and the

superfluid gap at zero temperature are calculated. Particular focus is put on the determination of the superfluid transition temperature resulting in the finite temperature phase diagram at different confinement of the Fermi gas. We compare these results with recent experimental observations in the end.

In Chapter 6 we perform an analytical continuation of the flow equation for the Euclidean propagators to obtain (real-time) spectral functions. After some general remarks on analytical continuation within the fRG framework, we show results for the fermionic spectral functions in the symmetry broken phase.

Chapter 7 is dedicated to gaining quantitative precision within the fRG framework. We formulate an iterative, ultraviolet safe procedure to obtain the density. The desired reduction of the scaling dimension is accomplished by first solving for the flow of higher moments of the density and subsequent integration such that we arrive at the density in the end. We elaborate on the shortcomings of this procedure for our choice of regulators and lay out a way to circumvent these. In the end, we present results for the equation of state and superfluid gap at zero temperature, thereby obtaining a Bertsch parameter which is in good agreement with recent experimental data.

Finally, our main findings are summarised in Chapter 8. Technical details and further information on calculations are moved to Appendices A – F.

CHAPTER 2

Fundamentals of ultracold atoms physics

In this Chapter we provide a short overview of the basics of ultracold atom physics relevant for this thesis. We start by discussing the length scales involved in a system of cold quantum gases resulting in a general scale hierarchy. This enables us to define an effective low-energy Hamiltonian which is then the starting point for the later considerations. After shortly reviewing the basic principles of Bose-Einstein condensation and Cooper pairing we end with a discussion of the transition from spatially separated fermions to tightly bound bosonic dimers in an ultracold Fermi gas, the so-called BCS-BEC crossover. A central ingredient for this is the ability to tune the interactions within a gas of ultracold atoms which is given by the concept of Feshbach resonances.

There are many pedagogical introductions to the field of condensed matter and ultracold atoms physics, for some recent reviews from a field theory perspective cf. e.g. [43, 104–107] out of which this Chapter draws a lot of inspiration.

2.1 Length scales in ultracold atom physics

We start by introducing the typical length scales involved in systems of ultracold quantum gases. This will also enable us to define an effective microscopic theory which can be used as a starting point of our later calculations in this thesis. These considerations are valid model independently and applicable to all (single valence electron) alkali systems, as they are used in cold atom experiments.

Typically, in an ultracold atoms system one can distinguish the following scales:

Interparticle spacing

For a homogeneous system with density n in d dimensions the interparticle spacing ℓ can be defined as

$$n = \ell^{-d}\,, \tag{2.1}$$

where one can view this as equally distributing N particles in boxes of volume $V = \ell^d$ such that $N = V/\ell^d$. This is, of course, an approximation to the real situation at hand in ultracold gases experiments since in most cases the trapping potential is in general space dependent. One thus has a space dependent density $n = n(\vec{x})$ and consequently chemical potential $\mu = \mu(\vec{x})$.

Oscillator length of the trapping potential

Let us consider a time-dependent (harmonic) potential of the form

$$V_{\text{trap}}(\vec{x}) = \frac{m}{2}\,\omega_0\, r^2\,, \tag{2.2}$$

with trapping frequency ω_0 and $r = |\vec{x}|$. Eq. (2.2) can be rewritten in terms of the oscillator length

$$\ell_{\text{osc}} = \left(\frac{\hbar}{m\,\omega_0}\right)^{1/2}. \tag{2.3}$$

This allows for a formulation in terms of the relevant length scale, to wit

$$V_{\text{trap}}(\vec{x}) = \frac{\hbar}{2}\,\omega_0\,\left(\frac{r}{\ell_{\text{osc}}}\right)^2. \tag{2.4}$$

From Eq. (2.4) we immediately see that our homogeneous assumption is valid if the physics takes place at much smaller length scales than the oscillator length of the trap ℓ_{osc}. This so-called local density approximation (LDA) enables one to neglect small corrections for points $\vec{x}$ and $\vec{y}$ being close to each other, as $n(\vec{x}) = n(\vec{y})\ (1 + \mathcal{O}(|\vec{x} - \vec{y}|)/\ell_{\text{osc}})$.

Thermal wavelength

The statistical behaviour of the gas is determined by the thermal de Broglie wavelength λ_{th} or rather its dimensionless ratio with the interparticle spacing. We can define the thermal de Broglie wavelength by

$$\lambda_{\text{th}} = \frac{h}{p} = \left(\frac{2\,\pi\,\hbar^2}{M\,k_B\,T}\right)^{1/2}. \tag{2.5}$$

The thermal de Broglie wavelength describes how a massive particle with momentum $p^2/2M = \pi\,k_B\,T$ and mass M coupled to a heat bath of temperature T behaves. We can now characterise the state of the ultracold quantum gas in terms of the interparticle spacing and its de Broglie wavelength. Associating the thermal wavelength λ_{th} with the spread of a particle pictured as wave-packet which has the interparticle distance ℓ as separation we see that below a certain temperature the wave-packets start to overlap. The gas then becomes quantum degenerate or ultracold for $\ell/\lambda_{\text{th}} \lesssim 1$. The system cannot be described

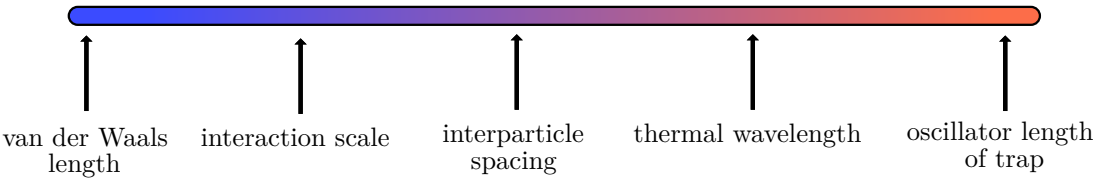

Figure 2.1: A typical scale hierarchy found in ultracold quantum gases. The system is bound on the one side by the length scale associated with the van der Waals potential an on the other side by the oscillator length of the trap $\ell_{\mathrm{vdW}} < \ell < \ell_{\mathrm{osc}}$. In a setting away from a Feshbach resonance the system is in a weakly interacting regime with the scattering length $a < \ell_{\mathrm{th}}$. Figure adapted from [43].

by a single-particle wave any more and one has to account for the many-body system in the context of quantum mechanics (or quantum field theory). The statistical behaviour is then determined by the spin of the particles resulting in Bose-Einstein or Fermi-Dirac distributions for bosons and fermions, respectively. Note that $\ell = \ell(n)$ and $\lambda_{\mathrm{th}} = \lambda_{\mathrm{th}}(T)$ represent the many-body length scales due to non-zero density and non-zero temperature.

Van der Waals length

The interaction effects for neutral alkali atoms used in cold atom experiments are electromagnetic through van der Waals forces. A typical interaction potential has a repulsive part $U(r) \sim 1/r^{12}$ on short distances r due to Pauli's principle inhibiting the electron clouds of two atoms to overlap. We will see that a hard core repulsion with infinite interaction strength works as well and yields the same scattering length. The attractive part, for large distances r, can be modelled as $U(r) \sim -1/r^6$ where the mutual polarisation of the electron clouds causes the attraction. This generic interatomic interaction is well described by the Lennard-Jones potential and can be approximated as

$$U_{\mathrm{vdW}}(r) = \begin{cases} \infty & \text{for } r \leq r_0 \\ -C/r^6 & \text{for } r > r_0 \,. \end{cases} \tag{2.6}$$

We then define the van der Walls length scale associated with the potential in Eq. (2.6) by

$$\ell_{\mathrm{vdW}} = \left(\frac{m\,C}{\hbar^2} \right)^{1/4} . \tag{2.7}$$

One finds that one never resolves physics beyond the van der Waals length ℓ_{vdW} since it is much smaller than the interparticle spacing, as well as the thermal wavelength. Thus, we can define an effective (low-energy) Hamiltonian valid on all scales $\gtrsim \ell_{\mathrm{vdW}}$. This microscopic Hamiltonian will later constitute the starting point for our calculation at an ultraviolet scale.

Scattering length

The relevant parameter to characterise the two-body scattering is the scattering length a which can be extracted from experiment. Here, we limit our discussion to the case of a three-dimensional system. For scattering theory in two spatial dimensions cf. e.g. [107] and references therein. The scattering length emerges as universal sole parameter for low-energy collisions in potentials of sufficiently short range, see e.g. [43]. Starting from the Schrödinger equation for the relative motion of the two particles we can define the collision state as a superposition of an incident plane wave and of a scattered wavefunction, cf. e.g. [108], to wit

$$\psi_k(\vec{x}) \sim e^{\mathrm{i}\, p\, z/\hbar} + f(p,\theta)\, \frac{e^{\mathrm{i}\, p\, r/\hbar}}{r}\,,$$

where the collision takes place in the z-direction. For a radial potential the scattering amplitude $f(p,\theta)$ depends on the centre of mass energy $p^2/(2\,M_{\mathrm{red}})$ with reduced mass M_{red}, as well as on the scattering angle θ. To solve this scattering problem one usually expands the scattering amplitude in partial waves $f(p,\theta) = \sum_{l=0}^{\infty}(2l+1) f_l(p) P_l(\cos\theta)$ with Legendre polynomials $P_l(\cos\theta)$ and determines the partial wave amplitudes $f_l(p)$. Due to the low energies present in ultracold atom physics, the expansion can be restricted to the case of $l = 0$ s-wave scattering. Higher angular momentum contributions with $l \neq 0$ introduce an additional barrier into the Schrödinger equation of the form $\hbar^2\, l\,(l+1)/(2\,M_{\mathrm{red}}\, r^2)$ where we can approximate $r^2 = \ell_{\mathrm{vdW}}^2$. Thus particles with energy $p^2/(2\,M_{\mathrm{red}}) \ll \hbar^2/\ell_{\mathrm{vdW}}^2$ can never overcome this barrier and we find ourselves in the situation of s-wave scattering. Due to the low-energy regime one can then approximate the scattering amplitude as [108]

$$f_{l=0} = \frac{1}{-\frac{1}{a} + 1/2\, r_e\, p^2 - \mathrm{i}\, p + \ldots}\,. \tag{2.8}$$

Here r_e refers to the effective range of the scattering and a denotes the scattering length. In ultracold quantum gases the corrections for the momentum p is subleading such that $f \simeq -a$. Thus the scattering length a is the universal (scattering) parameter describing ultracold physics. With the scattering length at hand, in Eq. (2.8), we can define a criterion for a weakly-interacting gas keeping in mind that the scattering length provides the typical extent of the collisional properties of a particle,

$$|a|\, n^{1/d} \ll 1\,.$$

In order to calculate the scattering for our system of a short range potential and low-energy scattering we can use the Born approximation. It expresses the scattering length as the Fourier transform of the interaction potential

$$a = \frac{M}{4\pi\hbar^2} \int d^3 r\, U(r)\, e^{\mathrm{i}\,\vec{q}\,\vec{r}}\,, \tag{2.9}$$

with $\vec{q}$ being the transferred momentum. From Eq. (2.9) we find immediately that the same scattering length is reproduced by very different interaction potentials.

One can show that one can replace the more complicated Lennard-Jones potential in Eq. (2.6) by a convenient local contact potential

$$U_\Lambda(r) = g_\Lambda \, \delta(\vec{x}) \, . \tag{2.10}$$

This potential in Eq. (2.10) has to be regularised at short distances and requires the usual renormalisation procedure afterwards. This is denoted by the index Λ referring to the ultraviolet cutoff. Lastly, we can relate the renormalised coupling g to scattering length a which can be measured in experiment

$$a = \frac{M}{4\pi\hbar^2} \, g \, .$$

In Fig. 2.1 we summarise the aforementioned scale hierarchy present in ultracold quantum gases. Here, we have with the scales defined by Eq. (2.1), Eq. (2.3), Eq. (2.5), Eq. (2.7) and Eq. (2.8)

$$\ell_{\mathrm{vdW}} \lesssim |a| < \ell < \ell_{\mathrm{th}} < \ell_{\mathrm{osc}} \, . \tag{2.11}$$

Due to the fact that all physics takes place at length scales larger than the van der Waals length one can write down an effective low-energy Hamiltonian

$$\hat{H} = \int_{\vec{x}} \left(\hat{a}^\dagger(\vec{x}) \left(-\frac{\nabla^2}{2M} + V_{\mathrm{ext}}(\vec{x}) \right) \hat{a}(\vec{x}) + g_\Lambda \, \hat{n}(\vec{x})^2 \right) , \tag{2.12}$$

with the usual creation and annihilation operators $\hat{a}^\dagger$ and $\hat{a}$. The local density operator is given by $\hat{n}(\vec{x}) = \hat{a}^\dagger(\vec{x}) \, \hat{a}(\vec{x})$. The squared density operator $\hat{n}(\vec{x})^2$ in Eq. (2.12) comes from the fact that at least two particles are needed to meet at point $\vec{x}$ in order to interact. It is an important property of ultracold alkali atoms that they can be described by this universal Hamiltonian (2.12) where we also find that the system has the natural ultraviolet cutoff $\Lambda^{-1} \ll \ell_{\mathrm{vdW}}$. No many-body length scales can resolve physics on shorter length scales and thus microscopic details beyond Λ^{-1} are irrelevant.

It is very appealing that the interaction strength between the individual particles can be tuned in dilute ultracold alkali atoms. Magnetically tunable Feshbach resonances allow for changing the interaction between two different (hyperfine) species of fermions with the help of an external magnetic field. For a more detailed description see e.g. [106, 109]. On a general level, Feshbach resonances occur when a bound state in a closed channel is coupled resonantly with the scattering continuum of an open channel in a two-body collision. An external magnetic field couples differently to the distinct magnetic moments of the closed and open channel, thus allowing to tune the scattering length, i.e. the strength of the interaction [106]. Feshbach resonances enable a violation in the scale hierarchy in

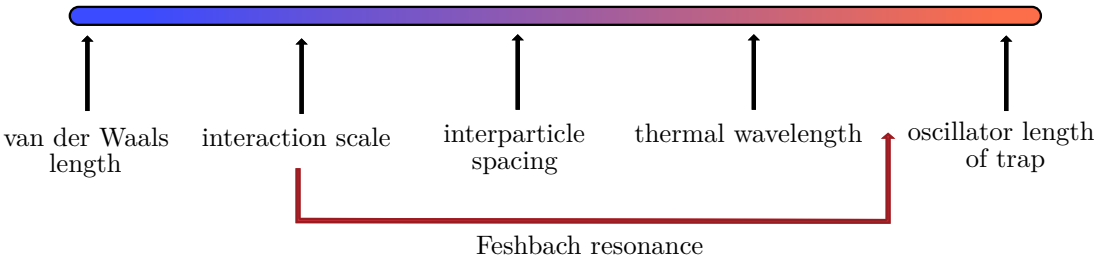

Figure 2.2: A typical scale hierarchy found in ultracold quantum gases. The system is bound on the one side by the length scale associated with the van der Waals potential an on the other side by the oscillator length of the trap $\ell_{\mathrm{vdW}} < \ell < \ell_{\mathrm{osc}}$. In the vicinity of a Feshbach resonance the system is strongly interacting with $\ell_{\mathrm{vdW}} << |a|$. Figure adapted from [43].

Eq. (2.11) and Fig. 2.1 by increasing the scattering length a compared to the interparticle spacing such that

$$\ell_{\mathrm{vdW}} \lesssim \ell < \ell_{\mathrm{th}} < |a| < \ell_{\mathrm{osc}} \,.$$

Thereby the ultracold atoms system changes from a weakly to a strongly interacting system, cf. Fig. 2.2. A more detailed description of Feshbach resonances can be found in Sec. 2.4. Note however, that the argument for the effective Hamiltonian remains valid, as the physics still takes places on length scales larger than the van der Waals length.

2.2 Thermodynamics

In this Section we give a very brief summary of the relevant thermodynamic variables involved in ultracold quantum systems. These considerations will be model independent and we will find that the phase diagram together with the equation of state encode important aspects of the equilibrium state. These are experimentally accessible and it is therefore desirable to compute them in a fashion comparable with experiment.

In its pure form, thermodynamic relations are only valid in infinitely expanded volume, which is not the case in experiments. However, formulated in terms of intensive quantities, like particle or entropy densities, this shortcoming is overcome and we can define the thermodynamic laws for subsystems at finite volume and particle number.

The equation of state $P(\mu, T)$ is a central quantity in thermodynamics as it stores the full thermodynamic information in terms of the pressure as a function of the chemical potential μ and the temperature T. One can then express all other thermodynamic quantities by using the Gibbs-Duhem relations $\mathrm{d}P = n\,\mathrm{d}\mu + s\,\mathrm{d}T$ and $\varepsilon = Ts - P + \mu n$ with the particle number density $n = N/V$, the entropy density $s = S/V$ and the energy density $\varepsilon = E/V$. The chemical potential at a given temperature determines the particle number

$N(\mu)$. When formulating the chemical potential in terms of the density $n(\mu, T)$ we can express the equation of state as a Legendre transform of the pressure, i.e. the free energy density $f(n, T)$ according to $f(n, T) = \mu\, n - P$ from which all desired equilibrium quantities can be derived.

For non-homogeneous trapping potentials $V_{\text{ext}}(\vec{x})$ one usually turns to the local density approximation (LDA) which has been successfully applied in many experimental measurements. Here, one assumes that there exists a mesoscopic scale ℓ_{mes}, smaller than the extent of the system but larger than the interparticle spacing ℓ or the scattering length a, over which the system can be thought of as homogeneous. Consider two neighbouring sub-volumes V_1 and V_2 inside the trapped gas with each their local temperature and chemical potential. Thermal and chemical processes will lead to an equilibration of the two subsystems resulting in an overall constant chemical potential inside the trap (since the two subsystems were picked arbitrarily). One can use the (grand canonical) partition function to show that the pressure of the system inside the inhomogeneous trap is given by the homogenous one with the chemical potential shifted w.r.t. the trapping potential

$$P = P_{\text{hom}}(\mu - V_{\text{ext}}(\vec{x}), T)\,, \tag{2.13}$$

and consequently for the chemical potential itself

$$\mu = \mu_{\text{hom}}(n(\vec{x}), T) + V_{\text{ext}}(\vec{x})\,. \tag{2.14}$$

The relations (2.13) and (2.14) are also valid per spin component σ of e.g. a two-component Fermi gas.

The equation of state also contains information about the phases the system is in, i.e. its phase diagram. One can distinguish different phases by macroscopic observables which change (abruptly) at a phase transition. These feature discontinuities in thermodynamic variables, typically in higher derivatives of the (grand canonical) potential or the pressure $P(\mu, T)$. In order to more formally characterise phase transitions, order parameters $\rho_0(\mu, T)$ can be defined which yield a non-vanishing value in one and a vanishing value in a different phase. Using this, one is able to calculate the phase diagram in the (μ, T)- or equivalently (n, T)-plane. We can then define the critical temperature $T_c(\mu)$ at a fixed chemical potential μ at which the phase transition takes places as $\rho_0(\mu, T_c(\mu)) = 0^+$. This provides us with a simply way to calculate the phase structure of the system.

2.3 Bose Einstein condensation and Cooper pairing

Having introduced the concept of phase transitions in Sec. 2.2 we can now turn to the case of Bose and Fermi gases. They both exhibit a (second order) phase transition below a critical temperature T_c, at the on hand by Bose-Einstein condensation for bosons and by Cooper pairing on the other hand for weakly interacting fermions. Here, we want to very briefly recap on the fundamental concepts.

The statistics of bosons and fermions differs fundamentally. While the many-body wavefunction of bosons is symmetric under the exchange of two particles, it is anti-symmetric for fermions, thus leading to two very different probability distributions. For bosons the occupation probability of a state with energy ε and temperature $T = k_B/\beta$ is given by the Bose-Einstein distribution ($\zeta = 1$), while fermions obey the Fermi-Dirac distribution ($\zeta = -1$)

$$n(\varepsilon, \mu, T) = \frac{1}{e^{\beta(\varepsilon-\mu)} - \zeta} \,. \tag{2.15}$$

As a consequence, at most one fermion can occupy a quantum state, while for bosons there exists no restriction on the number of particles per state.
Furthermore, we know from statistical physics that the equation of state for both bosons (with no condensate present) and fermions is given by

$$P(\mu, T) = -\zeta \, g \, k_B \, T \int \frac{\mathrm{d}^d p}{(2\pi\hbar)^d} \log\left(1 - \zeta \, e^{-\beta(\varepsilon_p - \mu)}\right) , \tag{2.16}$$

with the energy $\varepsilon_p = \vec{p}^2/(2M)$, g the spin degeneracy and $\zeta = 1$ ($\zeta = -1$) for bosons (fermions).

2.3.1 Bose-Einstein condensation of bosons

For a non-interaction bosonic system at zero temperature, the lowest energy state is macroscopically occupied, i.e. all bosons are condensed in the $\vec{p} = 0$ state forming a Bose-Einstein condensate. Increasing the temperature causes the particles to be excited into higher energy states until at very high temperatures no state is macroscopically occupied and we arrive at a Boltzmann distributed gas. This suggests that there exists a critical temperature at which the free Bose gas becomes a Bose-Einstein condensate. By starting from the density, i.e. μ-derivative of the equation of state in Eq. (2.16), we can compute the critical temperature T_c in three dimensions by setting $\mu = 0$,

$$n = \frac{1}{\lambda_{\mathrm{th}}^3 \, \Gamma(3/2)} \int_0^\infty \mathrm{d}\varepsilon \, \frac{\varepsilon^{1/2}}{e^{\varepsilon/(k_B \, T_c)} - 1} \,. \tag{2.17}$$

Here, we already used the three-dimensional density of states $\rho(\varepsilon) \sim \varepsilon^{1/2}$. Eq. (2.17) can be evaluated by the using the Riemann zeta function, yielding for the critical temperature

$$T_c = 3.31 \, n^{2/3}/M \,.$$

Lowering the temperature below the critical temperature, the number of excited particles becomes smaller and the condensate fraction N_0/N, i.e. the number of particles in the zero-momentum state w.r.t. the total particle number, follows the form

$$N_0(T)/N = 1 - \left(\frac{T}{T_c}\right)^{3/2} \qquad \text{for } T \leq T_c \,.$$

The condensate fraction is an order parameter for the phase transition and vanishes continuously for $T \to T_c$ signalling a second order phase transition.

In dimensions below three we find that, by using the general expression for the density of states in d spatial dimensions $\rho(\varepsilon) \sim \varepsilon^{d/2-1}$, that there exists no phase transition at a non-zero critical temperature for $d \leq 2$. This can be more generally formulated as the Mermin-Wagner theorem [110, 111] which states that there is no spontaneous breaking of a continuous symmetry and thus there exists no long-range order in $d \leq 2$. However, quasi-long-range order, as in the Berezinski-Kosterlitz-Thouless (BKT) transition, may exist. Furthermore, the trapping potential in ultracold experiments prohibits long wavelength fluctuations destroying the long-range order such that phase transitions can be nonetheless observed, even in lower dimensions.

For weakly interacting bosons one usually turns to the Bogoliubov theory which is equivalent to mean field theory and Gaussian approximation and captures most of the physics at hand. One finds the Bogoliubov excitation spectrum yielding a linear dispersion for long wavelength excitations and a quadratic particle-like spectrum at short scales. The low momentum behaviour signals a second order phase transition into the superfluid phase for the case of a three-dimensional weakly interaction Bose gas. Here, the superfluidity can be characterised by the Landau criterion [43]. Note that superfluidity and condensation are distinct phenomena, as can be seen in the case of a BKT transition where superfluidity but no condensate is present below a critical temperature. For a comprehensive overview of the physics of weakly interacting bosons cf. [43].

2.3.2 Fermi surface and Cooper pairing

Fermions obey the Fermi-Dirac distribution in Eq. (2.15) and thus two or more fermions cannot occupy the same quantum state. The ground-state of N non-interacting fermions is then given by a Fermi sea where the N energetically lowest states are occupied. Due to rotational symmetry all occupied states lie inside a sphere of radius $\hbar\, k_F$ bounded by the Fermi surface. Dividing the phase space into cells of volume h^d we can count the states

$$n = \frac{g}{(2\pi\hbar)^3}\, V_d(p_F)\,,$$

where $V_3(p_F) = 4\pi/3\, p_F^3$ in three and $V_2(p_F) = \pi\, p_F^2$ in two dimensions. $p_F = \hbar\, k_F$ is called the Fermi momentum and in three and two spatial dimensions we have

$$k_F = (3\,\pi^2\, n)^{1/3} \qquad \text{for } d = 3\,,$$

$$k_F = (2\,\pi\, n)^{1/2} \qquad \text{for } d = 2\,.$$

From this, the Fermi energy $\varepsilon_F = p_F^2/(2M)$ and the Fermi temperature $T_F = \varepsilon_F/k_B$ can easily be derived. We thus see that the lowest energy excitations are not close to zero-momentum, but to the Fermi surface $|\vec{p}| = p_F$. As a consequence of the Pauli principle an ideal Fermi gas does not undergo Bose-Einstein condensation.

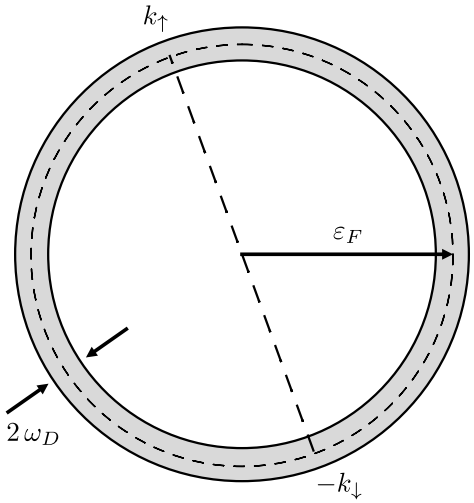

Figure 2.3: Two fermions with (near) opposite momentum and spin may form a pair on top of the Fermi sea which is energetically favourable. The range of the attraction is limited to energies of the order of the Debye frequency $\sim \omega_D$ around the Fermi surface, depicted by the grey shell. Figure adapted from [105].

The situation however changes fundamentally for attractively interacting fermions, no matter how weak the attraction is. As pointed out by Cooper in the presence of a Fermi sea it is energetically favourable for two fermions interacting via a phonon mediated interaction to form a bound state, called a Cooper pair. The new many-body ground-state consists of a 'Bose-Einstein condensate' of Cooper pairs and the Fermi sea is unstable towards the formation of it [104]. The tendency to form Cooper pairs on opposite points of the Fermi surface for an arbitrarily weak interaction is shown in Fig. 2.3. The locality in momentum space implies that the Cooper pairs have a large spatial extent in position space. It can be shown in BCS-theory (named after Baardeen, Cooper and Schrieffer) that the formation of Cooper pairs opens a gap, usually denoted Δ, in the continuous excitation spectrum.

The second order phase transition into the BCS state of condensed Cooper pairs is characterised by a critical temperature

$$T_c/T_F = \frac{8\,e^{\gamma-2}}{\pi}\, e^{-\pi/(2\,|k_F\,a_{3\mathrm{D}}|)} \qquad \text{for } d=3\,,$$
$$T_c/T_F = \frac{2\,e^{\gamma}}{\pi\,k_F\,a_{2\mathrm{D}}} \qquad \text{for } d=2\,,$$

with $\gamma = 0.577$ being Euler's constant. These are typically obtained from a (renormalised) gap equation demanding that the superconducting (or superfluid) gap Δ vanishes at the critical temperature T_c as $\Delta \xrightarrow{T\to T_c^-} 0^+$.

2.4 The BCS-BEC crossover

In this Section we give a short overview of the physics of a two-component Fermi gas with tunable interactions. As mentioned above one may make use of Feshbach resonances in order to tune the scattering properties, thereby going from a purely fermionic system with weak attractive interactions and large spatial separation to an effectively bosonic one with bosonic dimers consisting of two tightly bound fermions. Below a critical temperature a second order phase transition into the superfluid phase takes place by either the formation of Cooper pairs for weakly interacting fermions or by Bose-Einstein condensation for weakly repulsive bosons.

On a general level, a two-channel model is needed to describe a Feshbach resonance where two fermions in the open channel are coupled to a bound state in the closed channel. The scattering length can be tuned by an external magnetic field B and we can write on a phenomenological level

$$a = a_{\mathrm{bg}} \left(1 - \frac{\Delta B}{B - B_0}\right) ,$$

where a_{bg} is the off-resonant background scattering length without coupling to the closed channel. The position and width of the resonance in the external magnetic field are given by B_0 and ΔB, respectively. We consider two alkali atoms, in ultracold Fermi gases usually ^{6}Li and ^{40}K, with a hyperfine splitting of the ground-state, due to coupling of the electron spin to the spin of the nucleus. When scattering of each other in a multi-channel scattering, the two-body system will in general be a superposition of a singlet and a triplet state with different energy levels. The two particles can then resonantly tunnel from the ingoing open channel into the bound state of the closed channel situated close to the scattering threshold, as depicted in Fig. 2.4a. Here, the energetic distance of the bound state to the scattering threshold $E = 0$ is called detuning

$$\nu(B) = \Delta\mu \, (B - B_0) \, . \tag{2.18}$$

The external magnetic field B can then couple differently to the open and closed channels due to their difference in magnetic moment $\Delta\mu$. Consequently, the relative energy between the channels can be tuned $\Delta E \to \Delta E + \Delta\mu \, B$ such that in particular the detuning vanishes $\nu(B) \to 0$. Then both channels couple resonantly and the the system becomes strongly interacting, see Fig. 2.4b. In most cases the Feshbach resonance is a so-called 'broad' resonance where the width of the resonance is much larger than the Fermi energy. In this case it is sufficient to describe the scattering by a single-channel model, instead of the two-channel model above. For a detailed description of Feshbach resonances cf. e.g. [109].

Feshbach resonances give an experimental knob for tuning a gas of ultracold fermions across a wide range of interaction strengths from a purely fermionic system described by the Bardeen-Cooper-Schrieffer (BCS) theory to a effectively bosonic system described

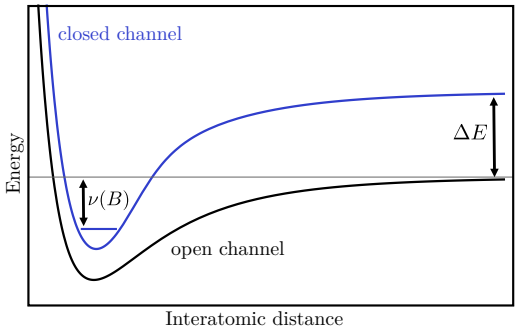

(a) The open and closed channel of the two-body scattering process. The detuning $\nu(B)$ denotes the energetic distance of the closed channel bound state from the scattering threshold, while the difference in energies between both channels ΔE can be tuned according to $\Delta E \to \Delta E + \Delta\mu\, B$. Adapted from [43].

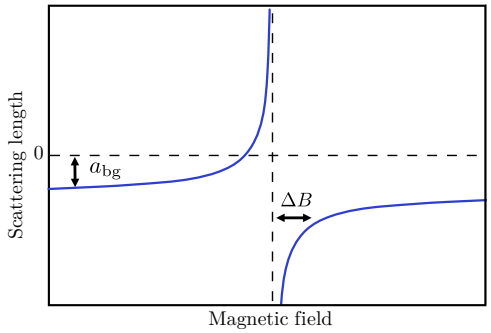

(b) Schematic picture of the magnetic field dependence of the scattering length. It can be characterised by an off-resonant scattering length a_{bg} and the width of the resonance ΔB. The scattering length diverges at the resonance position of the magnetic field. Adapted from [109].

Figure 2.4: Properties of Feshbach resonances.

by Bose-Einstein condensation (BEC). One obtains a smooth crossover from the weakly interacting BCS theory over a region of strong interactions to the weakly interacting BEC theory. At the centre of the three-dimensional BCS-BEC crossover, at diverging scattering length $a_{3\mathrm{D}}$, the system is in the unitarity limit which behaves in a scale invariant universal way.

As the interparticle spacing is well approximated by the inverse of the Fermi momentum $\ell \simeq k_F^{-1}$, we can build the dimensionless quantity $(k_F\, a_{3\mathrm{D}})^{-1}$, sometimes also called the inverse concentration. We can then identify three regimes within the three-dimensional BCS-BEC crossover:

$$
\begin{aligned}
(k_F\, a)^{-1} \to -\infty \;: &\qquad \text{weakly interacting fermions}\,,\\
|(k_F\, a)^{-1}| \leq 1 \;: &\qquad \text{strongly correlated regime}\,,\\
(k_F\, a)^{-1} \to \infty \;: &\qquad \text{weakly interacting bosonic dimers}\,.
\end{aligned}
$$

For the strongly correlated regime, near the unitarity limit, perturbative methods can no longer be applied and we will turn to the non-perturbative functional renormalisation group in the following.

It is of great importance for the understanding of many-body theory to determine the phase diagrams in three and two dimensions from first principles, as well as the calculation of the equation of state, especially the Bertsch parameter, and the critical temperature T_c/T_F at unitarity in a quantitative manner.

CHAPTER 3

Functional methods

This Chapter is in some parts based on [1].

In this Chapter we review some basic principles of functional approaches to quantum field theory viewed from a path integral perspective. We then introduce the functional renormalisation group which can be seen as a continuous version of the Kadanoff block spinning method with finiteness as an inherent feature. Applying these considerations to our situation of an ultracold Fermi gas within the BCS-BEC crossover we present a starting point for the work in this thesis.

In general, a quantum field theory (QFT) is fully determined by its complete set of correlation functions. We work in a Wick-rotated Euclidean space-time with imaginary time where the QFTs correspond to a quantum statistical theories.

The considerations in this Chapter present no original work and are mostly well-known relations. The version presented here relies on formulations in typical reviews, e.g. [36–44, 112].

3.1 Generating functionals

The central object of a QFT is its generating functional $\mathcal{Z}[J]$ depending on the external source $J(x)$. The derivation presented here is done for a scalar field $\varphi(x)$, but can be generalised to complex and Grassmann fields in a straightforward manner. In the path integral formalism the partition function $\mathcal{Z}[J]$ for a scalar field $\varphi(x)$ in d-dimensional Euclidean space-time can be defined as

$$\mathcal{Z}[J] = \frac{1}{\mathcal{N}} \int [\mathcal{D}\varphi]_{\text{ren}} \exp\left\{-S[\varphi] + J \cdot \varphi\right\}. \tag{3.1}$$

Here, we introduced the (functional) measure $[\mathcal{D}\varphi]_{\text{ren}}$ which has to be regularised and renormalised appropriately. The classical bare action is given by $S[\varphi]$ and we used the

shorthand notation $J \cdot \varphi = \int_x J(x)\,\varphi(x)$. From Eq. (3.1) all correlation functions can be calculated, thereby cancelling the arbitrary normalisation factor $\mathcal{N}$

$$\langle \varphi_1 \dots \varphi_n \rangle_J = \frac{1}{\mathcal{Z}[J]} \frac{\delta^n \mathcal{Z}[J]}{\delta J_1 \dots \delta J_n} \,. \tag{3.2}$$

We summarised the space-time dependence in the field index $\varphi_i = \varphi(x_i)$. We now proceed by removing all redundancies present in the definition of the generating functional in Eq. (3.1) and consequently in the correlation functions in Eq. (3.2). The correlation functions in Eq. (3.2) can be expressed as a sum of connected and disconnected terms, or diagrams, where the latter can be re-expressed in terms of lower order correlation functions. These redundancies are cured by defining the Schwinger functional as the logarithm of the generating functional, Eq. (3.1), to wit

$$\mathcal{W}[J] = \log \mathcal{Z}[J] \,. \tag{3.3}$$

One finds that the Schwinger functional, Eq. (3.3), is a convex functional, which can be proven by using Hölder's inequality, and likewise to Eq. (3.2) the correlation functions can be derived from $\mathcal{W}[J]$ as

$$\langle \varphi_1 \dots \varphi_n \rangle_{\text{con}} = \frac{\delta^n \mathcal{W}[J]}{\delta J_1 \dots \delta J_n} \,. \tag{3.4}$$

The correlation functions in Eq. (3.4) are connected correlation functions. Of particular interest is its two-point function, since, as the propagator, it is a fundamental quantity in QFTs encoding its dispersion

$$G(x_1, x_2) = \frac{\delta^2 \mathcal{W}[J]}{\delta J_1 \delta J_2} = \langle \varphi_1 \varphi_2 \rangle - \langle \varphi_1 \rangle \langle \varphi_2 \rangle = \langle \varphi_1 \varphi_2 \rangle_{\text{con}} \,. \tag{3.5}$$

Due to the convex Schwinger functional the propagator is necessarily positive semi-definite and its spectrum larger than or equal to zero.

Despite the reduction in redundant information by defining the Schwinger functional, it itself contains redundancies since the connected correlation functions can be divided into one-particle irreducible (1PI) and one-particle reducible ones. In a diagrammatic language 1PI diagrams cannot be separated into one-particle reducible diagrams by cutting a single line. They thus contain all relevant information of the QFT at hand and the generating functional of 1PI correlation function, called the (quantum) effective action $\Gamma[\phi]$, is given by the Legendre transform of the Schwinger functional

$$\Gamma[\phi] = \sup_J \{J \cdot \phi - \mathcal{W}[J]\} = J_{\text{sup}} \cdot \phi - \mathcal{W}[J_{\text{sup}}] \,. \tag{3.6}$$

We introduced the expectation value of the field $\phi(x) =< \varphi(x) >$ and the field dependent current $J_{\text{sup}} = J_{\text{sup}}[\phi]$. Out of convenience, we drop the subscript $(\cdot)_{\text{sup}}$ from here on, understanding it implicitly. Of further importance is the convexity of the effective action

Eq. (3.6) which stems directly from the Legendre transform and the convexity of the Schwinger functional. The effective action is the central object when dealing with QFTs from a functional perspective. It is the quantum analogue of the classical action with its one-point function given by taking a functional derivative of Eq. (3.6),

$$\frac{\delta\Gamma[\phi]}{\delta\phi(x)} = J(x)\,. \tag{3.7}$$

Equation (3.7) are the quantum equations of motion in a given background J reducing to the quantum analogue of the classical equations of motion in the vacuum for a vanishing source J. We can define the general moments or vertices of the effective action $\Gamma[\phi]$ as

$$\Gamma^{(n)}(x_1,\ldots,x_n) = \frac{\delta\Gamma[\phi]}{\delta\phi_1\ldots\delta\phi_n}\,, \tag{3.8}$$

with $\Gamma^{(2)}[\phi]$ being just the inverse of the propagator as defined in Eq. (3.5), since

$$\int_{x_3} G(x_1,x_3)\,\Gamma^{(2)}(x_3,x_2) = \int_{x_3} \frac{\delta^2\mathcal{W}[J]}{\delta J_1\delta J_3}\,\frac{\delta^2\Gamma[\phi]}{\delta\phi_3\delta\phi_2} = \delta(x_1-x_2)\,. \tag{3.9}$$

Equation (3.8) contains all knowledge about the connected correlation functions which can be used to easily calculate the expectation value of arbitrary operators.

3.2 Functional renormalisation group

The non-perturbative functional renormalisation group (fRG) allows for a scale dependent study of physical systems and theoretical models. It is a modern implementation of Wilson's RG and enables one to go beyond perturbative methods, i.e. it is also applicable in strongly-correlated regimes. The fRG is based upon an exact functional flow-equation of a coarse-grained effective action (or Gibb's free energy in the language of statistical physics) which allows for the inclusion of (thermal and quantum) fluctuations on all scales. It encompasses both Bogoliubov theory and the hydrodynamic approach of Popov and is inherently free of divergences [44]. It has the advantage that several effects can be included simultaneously, and all known limits are directly realised. For reviews of the functional renormalisation group approach see e.g. [36–44, 112].

The microscopic action associated with the effective Hamiltonian given by Eq. (2.12) is related to an ultraviolet (UV) momentum scale $k = \Lambda$ at length scales much smaller than the van der Waals length ℓ_{vdW}. However, the relevant physics takes place at scales $\ll \Lambda$ where the thermal and quantum fluctuations are included. To incorporate these fluctuations and furthermore to obtain results in the strongly coupled regime the a scale dependent procedure is implemented via the functional renormalisation group, which includes these fluctuations successively at each momentum scale k.

For the scale dependent treatment the integration is grouped in frequency and momentum shells according to

$$q_0^2 + \left(\vec{q}^{\,2} - \mu\right)^2 \simeq k^4$$

with external momentum scale k. The infrared regularised partition function is then defined by

$$\mathcal{Z}_k[J] = \frac{1}{\mathcal{N}} \int [\mathcal{D}\varphi]_{\mathrm{ren},Q^2\geq k^2} \, \exp\left\{-S[\varphi] + J\cdot\varphi\right\}. \tag{3.10}$$

The scale dependent integration measure in Eq. (3.10) can be defined via a soft cutoff procedure

$$\int [\mathcal{D}\varphi]_{\mathrm{ren},Q^2\geq k^2} = \int [\mathcal{D}\varphi]_{\mathrm{ren}} \, \exp\left\{-\Delta S_k[\varphi]\right\},$$

where we introduced an infrared cutoff term

$$\Delta S_k[\varphi] = \frac{1}{2}\int_Q \varphi(Q)\, R_k(Q)\, \varphi(-Q).$$

The regulator $R_k(Q)$ may be chosen freely within the requirement that it suppresses low momentum modes $Q^2 \leq k^2$, while leaving high momentum modes unchanged

$$\lim_{q^2/k^2\to 0} R_k(Q) = k^2, \qquad \lim_{q^2/k^2\to\infty} R_k(Q) = 0. \tag{3.11}$$

The first condition in of Eq. (3.11) amounts to an effective infrared regularisation and introduces an additional mass in the path integral. The second condition ensures the physical limit in the limit $k \to 0$. Solving the theory at hand amounts to lowering the cutoff scale infinitesimally and successively integrating out momentum shells towards the infrared. Starting at a ultraviolet cutoff scale Λ with a finite generating function the infrared regularised one is finite as well. The flow equation for $\mathcal{Z}_k[J]$ is given by

$$k\,\partial_k\,\mathcal{Z}_k[J] = -\left\langle k\,\partial_k\,\Delta S_k[\varphi]\right\rangle\,\mathcal{Z}_k[J].$$

We can define the RG-time $t = \log\frac{k}{\Lambda}$ with respect to the reference scale, usually taken as the ultraviolet cutoff scale Λ. As outlined in Sec. 3.1 we are eventually interested in the flow equation for the (1PI) effective action. We define the scale dependent effective action $\Gamma_k[\phi]$ in the fashion of Eq. (3.6) as the Legendre transform of a scale dependent Schwinger functional $\mathcal{W}_k[J]$,

$$\Gamma_k[\phi] = J\cdot\phi - \mathcal{W}_k[J] - \Delta S_k[\phi].$$

The full quantum effective action is reached in the infrared $k \to 0$ when all (quantum and thermal) fluctuations are integrated out. For the flow equation of the effective action we then find

$$\begin{aligned}\partial_t\Gamma_k[\phi] &= -\partial_t\mathcal{W}_k[J] - \partial_t\Delta S_k[\phi] - \partial_t J\cdot\left(\phi - \mathcal{W}^{(1)}[J]\right)\\ &= \frac{1}{2}\,\mathrm{Tr}\,G_k[\phi]\,\partial_t R_k.\end{aligned}$$

In order to show this relation the flow equation of the scale dependent Schwinger functional $\mathcal{W}_k[J]$, the Polchinski equation, is used together with the fact that the first moment of the Schwinger functional $\mathcal{W}^{(1)}[J]$ gives the expectation value of the field. Formulating the scale dependent inverse propagator in terms of the two-point function of the Legendre transform

$$\Big[G_k[\phi]\Big]^{-1} = \Gamma_k^{(2)}[\phi] + \Delta S_k^{(2)} = \Gamma_k^{(2)}[\phi] + R_k\,, \tag{3.12}$$

we arrive at the usual form of flow equation of the effective action, the Wetterich equation [35]

$$\partial_t \Gamma_k[\phi] = \frac{1}{2}\,\mathrm{Tr}\,\Big(\Gamma_k^{(2)}[\phi] + R_k\Big)\,\partial_t R_k\,. \tag{3.13}$$

Equation (3.13) is the central component in the functional methods approach in this thesis, since all correlation functions can be derived from Eq. (3.13). Starting at $\Gamma_\Lambda = S$, the full effective action is reached after the inclusion of all fluctuations where Γ_k smoothly interpolates between the microscopic action Γ_Λ and the full effective action $\Gamma_{k=0} = \Gamma$. Each infinitesimal change of the average effective action is described by the flow equation, Eq. (3.13). In the end fluctuations with large wavelengths are included. Since the functional renormalisation group includes the fluctuations stepwise, there are no infrared divergences when approaching the inclusion of long wavelength modes. It is furthermore a remarkable feature of the flow Eq. (3.13) that it is a non-perturbatively exact equation with a one-loop structure. Higher moments can be obtained from Eq. (3.13) by taking functional derivatives. However, this procedure leads to an infinite tower of coupled differential equations where the n-point function depends on both the $(n+1)$- and $(n+2)$-point function. In order to circumvent this problem and to keep the numerical effort to an manageable level, truncation schemes are employed, see below.
Analogous to defining the quantum theory by means of the classical action in the path integral formulation, the initial effective action Γ_Λ together with the flow equation Eq. (3.13) determines the full quantum theory. We show a diagrammatic representation of the flow Eq. (3.13) in Fig. 3.1.

Due to the aforementioned infinite hierarchy of coupled differential equations and the fact that the flow equation (3.13) is an integro-differential equation, its full solution is in most cases out of reach. One therefore relies on approximation schemes to the full effective action Γ_k which should incorporate the examined physics already at lower order of the approximation and reduce the number of flow equations to a manageable set of couplings. Here we touch shortly upon expansion schemes typically employed for the solution of the flow equation of the effective action and higher moments.

3.2.1 Perturbative expansion

All orders of renormalised perturbation theory can be calculated iteratively within the flow equation framework. The $(N+1)$-loop is obtained by insertion of the N-loop result on the

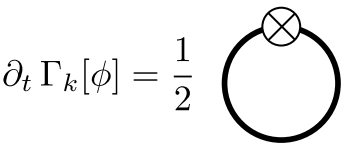

Figure 3.1: Diagrammatic depiction of the flow equation of the effective action Eq. (3.13). The solid line denotes the full propagator Eq. (3.12) and the cross the regulator insertion $\partial_t R_k$.

right hand side of the flow equation Eq. (3.13). We write the the scale dependent effective action within a loop expansion as

$$\Gamma_k = \lim_{N\to\infty} \Gamma_k^{\text{N-loop}}\,, \qquad \Gamma_k^{\text{N-loop}} = S + \sum_{n=1}^{N} \Delta\Gamma_{k,n}\,,$$

where S is the bare classical action and $\Delta\Gamma_{n,k}$ constitute the corrections due to quantum fluctuations at n-th order. One can then show that

$$\frac{1}{2}\,\mathrm{Tr}\,\frac{1}{\Gamma_k^{(2),N\text{-loop}} + R_k}\,\partial_t R_k = \partial_t\,\Gamma_k^{(N+1)\text{-loop}} + \mathcal{O}\left((N+2)\text{-loop}\right)\,. \tag{3.14}$$

Thus, starting at the classing two-point function $S^{(2)}[\phi]$ for $N = 0$ all higher loop contributions can be computed by this iterative procedure.

3.2.2 Vertex expansion

In the vertex expansion the scale dependent effective action $\Gamma_k[\phi]$ is expanded in powers of fields around a, in general, non-vanishing background $\bar{\phi}$. The information of Γ_k then lies in the vertices $\Gamma_k^{(n)}$,

$$\Gamma_k[\phi] = \sum_n \frac{1}{n!}\int \Gamma_k^{(n)}[\bar{\phi}](X_1,\dots X_N)\prod_{i=1}^{n}\left(\phi(X_i) - \bar{\phi}(X_i)\right)\,.$$

The infinite tower of coupled partial differential equations is cured by truncating the flow equations at a given order n, i.e. one approximates $\Gamma_k^{(m>n)} \equiv 0$. Vertex expansions are mostly used in the field of quantum chromodynamics and quantum gravity and allow for some error control in terms of convergence.

3.2.3 Derivative expansion

For low effective energy theories, like ultracold quantum gases, the derivative expansion is the standard expansions scheme. The basic idea is to expand the vertices in powers of the

momenta in momentum space where, contrary to the vertex expansion, already at lowest order all vertices are present. Assuming a mass gap m_{gap} of the theory, the derivative expansion is valid as long as the physical scales of the system q^2 are small compared to the mass gap

$$\frac{q^2}{m_{\text{gap}}^2} \ll 1\,, \tag{3.15}$$

which is valid in good approximation for ultracold atom systems. Within the fRG framework the regulator introduces an additional mass gap of order $\sim k^2$, thus improving the situation. Even without the existence of a physical mass gap, we find that the condition Eq. (3.15) is approximately fulfilled, since the regulator suppresses terms for $q^2 \leq k^2$. Generally speaking, the derivative expansion yields an expansion of the effective action around the low energy effective action where it is well described by the shape of the microscopic action.

3.3 QFTs at finite temperature and density

In this Section we briefly comment on how to introduce finite temperature and a non-zero density to a quantum field theory. We refrain from giving a complete account of the formalism summarising only the main results for this thesis and direct to the standard references, e.g. [113–116].

For a QFT at finite temperature in the imaginary time formalism the temperature is associated with a finite extent in the imaginary time direction. The imaginary time is then compactified to a torus of circumference β. Accordingly, bosonic and fermionic fields $\chi(\tau, x)$ have to be (anti-) periodic in the imaginary time direction $\tau = \mathrm{i}\beta$,

$$\chi(\tau = 0, x) = \zeta\, \chi(\tau = \beta, x)\,,$$

where $\zeta = 1$ for bosonic fields $\chi = \phi$ and $\zeta = -1$ for fermionic fields $\chi = \psi$. As a consequence all correlation functions inherit the (anti-) periodicity in imaginary time

$$\langle \chi(\tau_1, x_1) \ldots \chi(\tau_i + \beta, x_i) \ldots \chi(\tau_n, x_n)\rangle = \zeta\, \langle \chi(\tau_1, x_1) \ldots \chi(\tau_i, x_i) \ldots \chi(\tau_n, x_n)\rangle\,.$$

The (anti-) periodicity gives rise to an expansion of the fields in eigenmodes of the time resulting into corresponding discrete Matsubara frequencies

$$\begin{aligned} \omega_n &= 2\,n\,\pi\,T && \text{for bosonic fields } \phi\,, \\ \varepsilon_n &= (2n+1)\,\pi\,T && \text{for fermionic fields } \psi\,. \end{aligned} \tag{3.16}$$

Due to these discrete Matsubara modes the integration along the imaginary time p_0 in momentum space turns into a so-called Matsubara sum over all $n \in \mathbb{Z}$,

$$\int_{-\infty}^{\infty} \frac{\mathrm{d}p_0}{2\pi} \to T \sum_{n=-\infty}^{\infty}\,. \tag{3.17}$$

Technically, the Matsubara sums in Eq. (3.17) over the bosonic or fermionic Matsubara frequencies in Eq. (3.16) can be evaluated using the residue theorem by introducing additional functions which have poles at the discrete Matsubara frequencies.

In the grand canonical ensemble the particle number is given by a derivative of the effective action $\Omega(\mu, T) = \Gamma[\phi_{\mathrm{EoM}}; \mu, T]$ w.r.t. to the chemical potential

$$N = \frac{\partial \Gamma[\phi_{\mathrm{EoM}}; \mu, T]}{\partial \mu} ,$$

such that the effective potential contains a term $\Gamma \sim -\mu N$. This introduces a chemical potential μ into the microscopic action and together with the Matsubara formalism, we can describe equilibrium properties of QFTs at finite temperature and density.

3.4 Basics of the BCS-BEC crossover from functional renormalisation

In this Section we come back to our case of a two-component ultracold Fermi gas within the BCS-BEC crossover and apply the fRG formalism to this situation. We start by defining the microscopic action derived from Eq. (2.12) and elucidate some general aspects of the fRG for the BCS-BEC crossover, leaving the explicit derivation of the flow equations and the truncation to Chapter 4.

3.4.1 Model

Although the Hamiltonian in Eq. (2.12) defines a quantum field theory with creation and annihilation operators $\hat{a}^\dagger(\vec{x})$ and $\hat{a}(\vec{x})$, a formulation of the theory in terms of a functional integral is favourable, especially when applying functional methods to it. The derivation in terms of a complex field $\varphi(x)$ starts from the grand canonical partition function with temperature $\beta = 1/(k_B\, T)$ and chemical potential μ which is directly related to the generating functional in Eq. (3.1),

$$\mathcal{Z}(\mu, T) = \mathrm{Tr}\, \left(\exp\{-\beta(\hat{H} - \mu \hat{N})\} \right) = \int \mathcal{D}\varphi^*\, \mathcal{D}\varphi \exp\left\{-S[\varphi^*, \varphi]\right\} .$$

One then finds that the normal ordered Hamiltonian $\hat{H}(\hat{a}^\dagger, \hat{a})$ is connected to the microscopic action as

$$S[\varphi^*, \varphi] = \int_0^\beta \mathrm{d}\tau \left(\int_{\vec{x}} \varphi^*(\tau, \vec{x})\ (\partial_\tau - \mu)\ \varphi(\tau, \vec{x}) + H[\varphi^*(\tau, \vec{x}), \varphi(\tau, \vec{x})] \right) .$$

For our case of an ultracold Fermi gas close to a broad Feshbach resonance, as found in quantum gases consisting of ^{6}Li and ^{40}K, details of the (sub-) atomic interactions in

ultracold Fermi gases become irrelevant for the description of the macrophysics. The system can then be described by the universal action derived from Eq. (2.12)

$$S[\psi^*,\psi] = \int_X \left[\sum_{\sigma=1,2} \psi^*_\sigma (\partial_\tau - \nabla^2 - \bar{\mu})\psi_\sigma + \bar{\lambda}_\psi \psi^*_1 \psi^*_2 \psi_2 \psi_1 \right] . \tag{3.18}$$

Here ψ_σ and ψ^*_σ denote Grassmann fermions in the hyperfine state $\sigma = 1, 2$. We introduce $X = (\tau, \vec{x})$ with τ being the Euclidean time and $\int_X = \int_0^\beta d\tau \int d^d x$ with spatial dimension d. Moreover, the chemical potential $\bar{\mu}$ and the four-Fermi coupling $\bar{\lambda}_\psi \to \lambda_\psi = 8\,\pi\, a_{3\mathrm{D}}$ are related to the physical chemical potential and the scattering length through an appropriate vacuum renormalisation.

We use $\hbar = k_B = 2M = 1$ with M being the mass of the fermionic atoms. For sufficiently low temperatures, the ultracold Fermi gas may develop many-body instabilities resulting in the formation of a macroscopic anomalous self-energy Δ which is related to the non-vanishing expectation value $\langle \psi_1\, \psi_2 \rangle$. This is signalled by a divergence of the frequency- and momentum-dependent four-Fermi vertex at lower momentum scales and causes the breaking of the global $U(1)$-symmetry. In particular, in the strongly coupled regime, i.e. for a diverging three-dimensional s-wave scattering length $a_{3\mathrm{D}}$, the quantitative determination of this phase transition is complicated by the frequency and momentum dependence of the vertex. In order to resolve this difficulty, a scale dependent treatment in the path integral formulation is appropriate, as described by the flow equation in Sec. 3.2.

Furthermore, it is convenient to rewrite the four-Fermi interaction λ_ψ in Eq. (3.18) at a large cutoff Λ in terms of a bosonic degree of freedom ϕ via a Hubbard-Stratonovich transformation. The Hubbard-Stratonovich transformation basically amounts to inserting a functional one into the path integral such that the action becomes

$$S[\psi,\phi] = \int_X \left[\sum_{\sigma=1,2} \psi^*_\sigma \left(\partial_\tau - \nabla^2 - \bar{\mu}\right) \psi_\sigma + m^2_\phi\, \phi^*\phi - h\, \left(\phi^*\, \psi_1\, \psi_2 - \phi\, \psi^*_1\, \psi^*_2\right) \right], \tag{3.19}$$

with $\bar{\lambda}_\psi = -h^2/m^2_\phi$. This can be seen via a Gaussian integration over the bosonic field ϕ. The advantage is that it naturally accounts for the bosonic degrees of freedom over the BCS-BEC crossover enabling a unified description for the superfluid transition. The Yukawa-type Feshbach coupling h accounts for the interconversion of two fermionic atoms ψ with different spin to a bosonic dimer ϕ. In Equation (3.19) we neglected the four-Fermi interaction λ_ψ. For negative $\lambda_{\psi,\Lambda}$ at the microscopic scale it can absorbed via a rescaling of the Feshbach coupling h and the bosonic mass m^2_ϕ, but it would be generated during the flow to the infrared nonetheless. So, this approximation ignores some screening effects, yet catches the qualitative pictures accurately.

Connecting the above action to the experimental setup we explicitly introduce the closed channel in the context of Feshbach resonances, cf. Section 2.4, via the bosonic field ϕ. The physical detuning $\nu = \nu(B)$, which depends on the external magnetic field of the

trap in the experiment, denotes the distance of the closed-channel bound state from the scattering threshold. In the kinetic term of the bosonic dimer ϕ the factor of $\nabla^2/2$ reflects the composite mass of the dimer, while this composition also yields twice the chemical potential for the bosons

$$S[\psi,\phi] = \int_X \left[\psi^* \left(\partial_\tau - \nabla^2 - \mu\right) \psi + \phi^* \left(\partial_\tau - \frac{\nabla^2}{2} + \nu - 2\mu\right) \phi - h \left(\phi^* \psi_1 \psi_2 - \phi \psi_1^* \psi_2^*\right) \right] . \tag{3.20}$$

As we will see in more detail in Chapter 4, applying a derivative expansion within the functional renormalisation group approach, one can make the following ansatz for the scale dependent effective action.

3.4.2 Ansatz and ultraviolet renormalisation

The following considerations are, in general valid in three spatial dimensions. Potential generalisations to the case of a dimensional crossover from three to two dimensions are discussed in Chapter 5.

We employ the following ansatz for the effective action in derivative expansion

$$\Gamma_k[\psi,\phi] = \int_X \left[\sum_{\sigma=\{1,2\}} \psi_\sigma^* P_{\psi,\sigma}(Q) \psi_\sigma + \phi^* P_\phi(Q) \phi + V_k(\rho) - h(\phi^* \psi_1 \psi_2 - \phi \psi_1^* \psi_2^*) \right] , \tag{3.21}$$

with bare, unrenormalised (unrescaled) fields ψ, ϕ and inverse propagators $P_{\psi,\sigma}(Q), P_\phi(Q)$. The connection to the experiment is then given by the initial condition of the effective potential $V_k(\rho)$ in Eq. (3.21) at the ultraviolet scale Λ, which may only depend on the $U(1)$-invariant quantity $\rho = \phi^*\phi$,

$$V_\Lambda(\rho) = (\nu_\Lambda - 2\mu)\,\rho\,. \tag{3.22}$$

The solution of the flow equations derived from Eq. (3.21) then yields to the equation of state $n(\mu,T)$ and phase diagram $\rho_0(\mu,T)$ as function of the microscopic parameters, the detuning ν_Λ and the Feshbach coupling h. We thus need to map these microscopic parameters to the experimentally measurable scattering length $a_{3\mathrm{D}}$. To accomplish this, we (artificially) split the chemical potential into a vacuum and a many-body part $\mu = \mu_{\mathrm{vac}} + \mu_{\mathrm{mb}}$ and follow the RG-flow twice. In a first step, we solve the flow equations in vacuum for $\mu = \mu_{\mathrm{vac}}$ at zero temperature $T = 0$ where the many-body scales are never reached. This establishes the connection of the microscopic parameters to the scattering length. Afterwards, in the second step, we go beyond zero density and temperature, i.e. with the full chemical potential $\mu = \mu_{\mathrm{vac}} + \mu_{\mathrm{mb}}$ and $T \geq 0$, in order to obtain the physical equation of state $n(\mu,T,a_{3\mathrm{D}})$ and the phase diagram $\rho_0(\mu,T,a_{3\mathrm{D}})$ as function of experimentally measurable parameters. We can identify the following constraints for the different branches in

vacuum by considering the momentum independent parts of the propagators

$$\begin{aligned} &(i) && \text{atom sector } (a_{3\mathrm{D}} < 0): && m^2_{\phi,k=0} > 0,\ \mu_{\mathrm{vac}} = 0\,, \\ &(ii) && \text{resonance } (a^{-1}_{3\mathrm{D}} = 0): && m^2_{\phi,k=0} = 0,\ \mu_{\mathrm{vac}} = 0\,, \\ &(iii) && \text{dimer sector } (a_{3\mathrm{D}} > 0): && m^2_{\phi,k=0} = 0,\ \mu_{\mathrm{vac}} < 0\,. \end{aligned} \tag{3.23}$$

Here, the chemical potential $-\mu$ and the bosonic mass m^2_ϕ act as gaps in the propagation for fermions and bosons. In order to connect to the physical parameters one solves the flow equations for the bosonic mass m^2_ϕ and the Feshbach coupling in vacuum such that the physical quantities, i.e. at $k = 0$, match the conditions in Eq. (3.23). From Eq. (3.22) the initial value of the boson mass is given by

$$m^2_\phi = \nu(B) - 2\,\mu + \delta\nu(\Lambda)$$

where $\nu(B) = \Delta\mu\ (B - B_0)$ denotes the physical detuning from the scattering threshold with $\Delta\mu$ the relative magnetic moment of the molecules, cf. Eq. (2.18). The renormalisation counter term $\delta\nu(\Lambda)$ has to be adjusted such that the e.g. the resonance condition (ii) in Eq. (3.23) is satisfied. The two-body scattering length $a_{3\mathrm{D}}$ is then extracted from the analytic solution of the bosonic mass m^2_ϕ and the Feshbach coupling h, see e.g. [54],

$$a_{3\mathrm{D}} = a_{3\mathrm{D}}(B) = \frac{h^2_\Lambda}{8\,\pi\,\nu(B)}\,, \qquad \nu(B) = \nu_\Lambda - \delta\nu(\Lambda) = \nu_\Lambda - \frac{h^2_\Lambda}{6\,\pi^2}\,\Lambda\,,$$

allowing us to translate $(\nu_\Lambda, h_\Lambda) \to a_{3\mathrm{D}}$. Furthermore, one finds that the chemical potential only contributes on the BEC-side for the vacuum flow and can be interpreted as half the binding energy of a bosonic dimer

$$\mu_{\mathrm{vac}} = \frac{\varepsilon_B}{2}\,.$$

Having established the relation between the microscopic parameters and the physical scattering length in vacuum, it is now possible to go to finite density and temperature and determine the equation of state and the phase diagram. The results of which can be found in the following chapters.

CHAPTER 4

BCS-BEC crossover from functional renormalisation

This Chapter is in parts based on Ref. [1].

In this Chapter we derive the flow equations in the fRG framework, introduced in Section 3.2, for an ultracold Fermi gas for a d-dimensional system. Furthermore, we allow for a dimensional reduction in the form of a dimensional crossover in Section 4.6. By defining a Master equation all flow equations of the individual couplings can be obtained by suitable projection descriptions. Furthermore, for the flow equations in finite volume we only consider the isotropic case where the flow of the couplings in transversal direction equal the ones in the plane $g_i = g_{i,z}$, since this distinction is negligible [117]. A similar formulation can be found in [59].

4.1 Ansatz for the effective action and truncation

As outlined in Section 3.4.1 it is useful to perform a Hubbard-Stratonovich transformation in order to describe the relevant degrees of freedom of the physics at hand. Having introduced the physical detuning $\nu = \nu(B)$ in Eq. (3.20), for an explicit map to the experimental parameters, the full microscopic action is given by

$$S[\psi,\phi] = \int_X \left[\psi^* \left(\partial_\tau - \nabla^2 - \mu\right)\psi + \phi^* \left(\partial_\tau - \frac{\nabla^2}{2} + \nu - 2\mu\right)\phi - h(\phi^*\,\psi_1\,\psi_2 - \phi\,\psi_1^*\,\psi_2^*)\right]. \tag{4.1}$$

The kinetic term of the bosonic dimer ϕ reflects the composite mass of the dimer, while also accounting for twice the chemical potential for the bosons.

Our ansatz for the effective average action can be divided into a kinetic part and an interaction part

$$\Gamma_k = \Gamma_{\text{kin}} + \Gamma_{\text{int}}. \tag{4.2}$$

The kinetic part describes the fermion and boson dynamics and following Eq. (4.1) is within a derivative expansion given by

$$\Gamma_{\text{kin}} = \int_X \left[\sum_{\sigma=\{1,2\}} \overline{\psi}^*_\sigma \, \overline{P}_{\psi,\sigma}(Q) \, \overline{\psi}_\sigma + \overline{\phi}^* \, \overline{P}_\phi(Q) \, \overline{\phi} \right] . \tag{4.3}$$

The unrenormalised (unrescaled) fields $\overline{\psi}$, $\overline{\phi}$ and inverse propagators introduced in Eq. (4.3) follow the form of the microscopic action Eq. (4.1) and can be defined as

$$\begin{aligned} \overline{P}_{\psi\sigma}(Q) &= Z_{\psi\sigma} \, \mathrm{i} \, q_0 + A_{\psi\sigma} \, q^2 - \bar{\mu} \, , \\ \overline{P}_\phi(Q) &= Z_\phi \, \mathrm{i} \, q_0 - W_\phi \, q_0^2 + A_\phi \, q^2/2 \, . \end{aligned} \tag{4.4}$$

In this work we set $W_\phi = 0$. In terms of the renormalised (rescaled) fields $\psi = A_\psi^{1/2} \, \overline{\psi}$ and $\phi = A_\phi^{1/2} \, \overline{\phi}$ the kinetic part can be formulated as

$$\Gamma_{\text{kin}}[\psi, \phi] = \int_X \left[\sum_{\sigma=\{1,2\}} \psi^*_\sigma \left(S_\psi \, \partial_\tau - \nabla^2 - \mu \right) \psi_\sigma + \phi^* \left(S_\phi \, \partial_\tau - \frac{1}{2} \nabla^2 \right) \phi \right] . \tag{4.5}$$

We normalised the coefficients of the gradient terms by means of the wavefunction renormalisations A_ψ and A_ϕ which enter the renormalisation group flow via the anomalous dimensions

$$\eta_\psi = - \, \partial_t \, \log A_\psi , \quad \eta_\phi = - \, \partial_t \, \log A_\phi \, .$$

Moreover, coming from the inverse propagators in Eq. (4.4) we defined $S_{\psi,\phi} = Z_{\psi,\phi}/A_{\psi,\phi}$ and the renormalised chemical potential $\mu = \bar{\mu}/A_{\psi,\sigma}$ for Eq. (4.5). In general, the renormalised couplings are defined such that

$$\overline{\Gamma}[\overline{\psi}, \overline{\phi}] = \Gamma[\psi, \phi] \, .$$

The interactions in Eq. (4.2) can, after the Hubbard-Stratonovich transformation, be written as

$$\Gamma_{\text{int}}[\psi, \phi] = \int_X \left[V \left(\phi^* \, \phi \right) - h \, \left(\phi^* \, \psi_1 \, \psi_2 - \phi \, \psi_1^* \, \psi_2^* \right) \right] . \tag{4.6}$$

The effective average potential $V(\rho)$ depends only on the $U(1)$-invariant quantity $\rho = \phi^* \, \phi$ and describes bosonic scattering processes. The $U(1)$-symmetry is spontaneously broken for a non-zero minimum ρ_0 of the effective average potential and thus describes superfluidity. In a Taylor-expansion we write

$$V(\rho) = m_\phi^2 \, (\rho - \rho_0) + \frac{\lambda_\phi}{2} \, (\rho - \rho_0)^2 + \sum_{n=3}^{N} \frac{v_n}{n!} \, (\rho - \rho_0)^n \, . \tag{4.7}$$

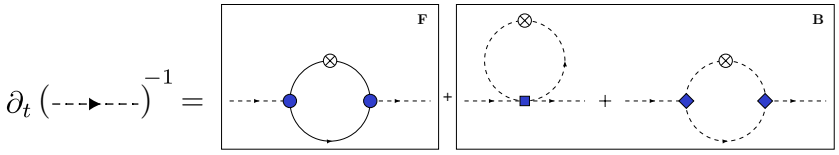

Figure 4.1: (F)- and (B)-truncation schemes of the flow equations. The flow of the inverse boson propagator incorporates both fermionic and bosonic diagrams. Bosonic propagators correspond to dashed and fermionic propagators to solid lines, while the distinct vertices are shown in different shapes. The regulator insertion is denoted by a cross.

where we need to include at least up to the second order in ρ to reproduce the second order phase transition to superfluidity. In the symmetric regime we therefore have $\rho_0 = 0$ and positive bosonic mass $m_\phi^2 > 0$, whereas the symmetry-broken regime is realised for $\rho_0 > 0$ and vanishing bosonic mass $m_\phi^2 = 0$. In the following we restrict this work to order ϕ^4.

The truncation can be classified by the diagrams in Fig. 4.1 included on the right hand side of the flow equation (3.13). By including only fermionic diagrams (F) we arrive at the mean-field result. Bosonic fluctuations enter the flow equation by including diagrams with two internal bosonic lines (B). In this thesis we only include effects from the renormalisation of the boson propagator in Fig. 4.1. The renormalisation of the fermion propagator depicted in Fig. 4.2 will be used in Chapter 6 to derive the analytically continued flow of the fermion two-point function.

Furthermore, baring in mind that $\bar{\Gamma}[\bar{\phi}] = \beta \operatorname{Vol}_d V(\rho)$, the flow of the (negative) density of the Fermi gas is calculated via a derivative of the effective action with respect to the chemical potential

$$\partial_k n_k = -\partial_k \frac{\partial V(\rho)}{\partial \mu} \,. \tag{4.8}$$

In practice, we approximate the dependence of the effective average action on the chemical potential by an expansion in ρ and μ [53]

$$V(\rho) = \sum_{n=1}^{2} \frac{v_n}{n!} (\rho - \rho_0)^n - n_k \, \delta\mu + \alpha_k (\rho - \rho_0) \, \delta\mu \,. \tag{4.9}$$

Here the chemical potential is split into a reference part μ_0 and an offset $\delta\mu$, such that $\mu = \mu_0 + \delta\mu$. This definition in Eq. (4.9) via Eq. (4.8) captures the density, and derived quantities, in a qualitative manner and constitutes an approximation. In Chapter 7 we expand on this simple approximation in order to gain quantitative results.

The inverse propagators $\overline{G}_{\phi}^{-1}(Q)$ and $\overline{G}_{\psi}^{-1}(Q)$ are calculated by functional derivatives of the effective action w.r.t. the corresponding fields

$$\begin{aligned}\bar{\Gamma}^{(2)}_{\bar{\phi}_i,\bar{\phi}_j}(X,Y,\bar{\rho}) &= \frac{\delta^2\,\bar{\Gamma}}{\delta\bar{\phi}_i(X)\,\delta\bar{\phi}_j(Y)}[\bar{\phi}] \\ \bar{\Gamma}^{(2)}_{\bar{\psi}_\alpha^{(*)},\bar{\psi}_\beta^{(*)}}(X,Y,\bar{\rho}) &= \frac{\overrightarrow{\delta}}{\delta\bar{\psi}_\alpha^{(*)}(X)}\,\bar{\Gamma}\,\frac{\overleftarrow{\delta}}{\delta\bar{\psi}_\beta^{(*)}(Y)}\,[\bar{\phi}]\,.\end{aligned} \tag{4.10}$$

The direction of the arrow for the inverse fermion propagator denotes derivatives acting from left and right on the effective potential. In momentum space we arrive after a Fourier transform of Eq. (4.10) at

$$\begin{aligned}\bar{\Gamma}^{(2)}_{BB}(Q,Q') &= \delta(Q+Q')\,\overline{G}_{\phi}^{-1}(Q)\,, \\ \bar{\Gamma}^{(2)}_{FF}(Q,Q') &= \delta(Q+Q')\,\overline{G}_{\psi}^{-1}(Q)\,.\end{aligned} \tag{4.11}$$

After performing the functional derivatives according to Eq. (4.11) of our ansatz in Eq. (4.5) and Eq. (4.6) we obtain in the $\{\phi_1,\phi_2\}$-basis for a constant bosonic background field $\phi=\sqrt{\rho}$

$$\begin{aligned}\overline{G}_{\phi}^{-1}(Q) &= A_\phi \begin{pmatrix} P_\phi^{S,Q} + V' + 2\,\rho\,V'' & \mathrm{i}\,P_\phi^{A,Q} \\ -\mathrm{i}\,P_\phi^{A,Q} & P_\phi^{S,Q} + V' \end{pmatrix}, \\ \overline{G}_{\psi}^{-1}(Q) &= A_\psi \begin{pmatrix} -h\,\sqrt{\rho}\,\varepsilon & -P_\psi^{-Q}\,\mathbb{1} \\ P_\psi^{Q}\,\mathbb{1} & h\,\sqrt{\rho}\,\varepsilon \end{pmatrix}.\end{aligned} \tag{4.12}$$

Here $\mathbb{1}$ is the 2-dimensional unity matrix, $\varepsilon=((0,1),(-1,0))$ the fully antisymmetric tensor and a prime denotes a derivative with respect to ρ. The regulators in the $\{\phi_1,\phi_2\}$-basis are likewise given by

$$\begin{aligned}\overline{R}_{\phi}^{Q} &= A_\phi\,R_\phi^Q = A_\phi \begin{pmatrix} R_\phi^S(Q) & \mathrm{i}\,R_\phi^A(Q) \\ -\mathrm{i}\,R_\phi^A(Q) & R_\phi^S(Q) \end{pmatrix}, \\ \overline{R}_{\psi}^{Q} &= A_\psi\,R_\psi^Q = A_\psi \begin{pmatrix} 0 & -R_\psi^{-Q}\mathbb{1} \\ R_\psi^Q\,\mathbb{1} & 0 \end{pmatrix}.\end{aligned} \tag{4.13}$$

Moreover we defined the symmetrised and anti-symmetrised components of the propagators and regulator functions as

$$f^{S,A}(Q) = \frac{f(Q)\pm f(-Q)}{2}\,. \tag{4.14}$$

For a more streamlined notation we define the short-hand abbreviation for the sum of

propagator and regulator, as well as the determinants

$$\begin{aligned} L_\psi^Q &= P_\psi^Q + R_\psi^Q \,, \\ \det{}_F^Q &= L_\psi^Q \, L_\psi^{-Q} + h^2 \, \rho \,, \\ L_\phi^Q &= P_\phi^Q + R_\phi^Q + V' + \rho \, V'' \,, \\ \tilde{L}_\phi^Q &= P_\phi^Q + R_\phi^Q \,, \\ \det{}_B^Q &= L_\phi^Q \, L_\phi^{-Q} - (\rho V'')^2 \,. \end{aligned} \tag{4.15}$$

We then may write the regularised propagators with the definitions in Eq. (4.15) as

$$\begin{aligned} G_\phi^Q &= A_\phi \, \overline{G}_\phi^Q = \frac{1}{\det{}_{\mathrm{B}}^Q} \begin{pmatrix} \tilde{L}_\phi^{S,Q} + V' & -\mathrm{i} \, \tilde{L}_\phi^{A,Q} \\ \mathrm{i} \, \tilde{L}_\phi^{A,Q} & \tilde{L}_\phi^{S,Q} + V' + 2 \, \rho \, V'' \end{pmatrix} , \\ G_\psi^Q &= A_\psi \, \overline{G}_\psi^Q = \frac{1}{\det{}_{\mathrm{F}}^Q} \begin{pmatrix} (h^2 \, \rho)^{1/2} \, \varepsilon & L_\psi^{-Q} \, \mathbb{1} \\ -L_\psi^Q \, \mathbb{1} & -(h^2 \, \rho)^{1/2} \, \varepsilon \end{pmatrix} . \end{aligned} \tag{4.16}$$

We can also represent the boson propagator in Eq. (4.16) in the conjugate field basis $\{\phi, \phi^*\}$ where the corresponding matrix will be labelled by a hat. For $\phi = (\phi_1 + \mathrm{i} \, \phi_2)/\sqrt{2}$ we have

$$\begin{pmatrix} \phi \\ \phi^* \end{pmatrix} = \frac{1}{\sqrt{2}} \begin{pmatrix} 1 & \mathrm{i} \\ 1 & -\mathrm{i} \end{pmatrix} \begin{pmatrix} \phi_1 \\ \phi_2 \end{pmatrix} ,$$

and thus arrive the inverse propagator in the conjugate field basis

$$\widehat{G}_\phi^{-1} = U \, G_\phi^{-1} \, U^t \,.$$

Here, we used the definitions

$$U = \frac{1}{\sqrt{2}} \begin{pmatrix} 1 & -\mathrm{i} \\ 1 & \mathrm{i} \end{pmatrix} , \quad U^t = \frac{1}{\sqrt{2}} \begin{pmatrix} 1 & 1 \\ -\mathrm{i} & \mathrm{i} \end{pmatrix} .$$

Explicitly, we then obtain for the inverse boson propagator in the $\{\phi, \phi^*\}$-basis

$$\widehat{G}_\phi^{-1} = \begin{pmatrix} \rho \, V'' & L_\phi^{-Q} \\ L_\phi^Q & \rho \, V'' \end{pmatrix} , \quad \widehat{R}_\phi(Q) = \begin{pmatrix} 0 & R_\phi^{-Q} \\ R_\phi^Q & 0 \end{pmatrix}$$

and

$$\widehat{G}_\phi^Q = \frac{1}{\det{}_{\mathrm{B}}^Q} \begin{pmatrix} -\rho \, V'' & L_\phi^{-Q} \\ L_\phi^Q & -\rho \, V'' \end{pmatrix}$$

To generate higher n-point functions further functional derivatives have to be applied, once again paying attention to the correct ordering for fermionic derivatives.

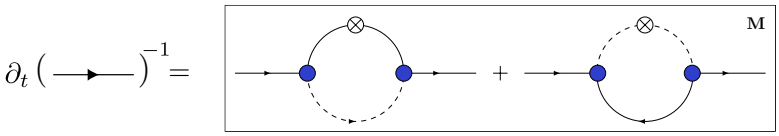

Figure 4.2: The mixed diagrams describing the flow of the inverse fermion propagator. Bosonic propagators correspond to dashed and fermionic propagators to solid lines, distinct vertices are shown in different shapes. The regulator insertion is denoted by a cross. Here, we both have bosonic, as well as fermionic internal lines.

Since we assume momentum and frequency independent vertices to close our set of equation, the complexity of the system of differential equations is drastically reduced

$$\bar{\Gamma}_k^{(n>2)}(Q_1,\ldots,Q_n) = \bar{\gamma}_k^{(n)}\,\delta(Q_1,\ldots,Q_n)\,. \tag{4.17}$$

Given our ansatz in Eq. (4.5) and Eq. (4.6) the three- and four-point vertices are given in Appendix D according to Eq. (4.17).

Explicitly, the truncation used in this thesis includes the following running couplings:

$$V(\rho),\ A_\phi,\ S_\phi\,. \tag{4.18}$$

The running of the renormalised Feshbach coupling is then given via the anomalous dimension $\eta_\phi = -\dot{A}_\phi/A_\phi$. The running of the effective potential then includes $m_\phi^2, \rho_0, \lambda_\phi, \alpha, n$ in Chapter 5 and Chapter 6 and $m_\phi^2, \rho_0, \lambda_\phi$ in Chapter 7, where the density is obtained by an iterative computation.

4.2 Regulator scheme

In this work we choose the optimised three-dimensional Litim-type regulator [118–120] for the cutoff function $R(Q)$ in three spatial dimensions. It is given for bosons and fermions, respectively, by

$$\begin{aligned} R_{\phi,k}(q^2) &= \left(k^2 - q^2/2\right)\,\theta\left(k^2 - q^2/2\right)\,, \\ R_{\psi,k}(q^2) &= k^2\,\left(\mathrm{sgn}\,(z) - z\right)\,\theta\left(1 - |z|\right)\,, \end{aligned} \tag{4.19}$$

where $\theta(x)$ represents the Heaviside-Theta function, $\mathrm{sgn}(x)$ the sign function and we used $z = (q^2 - \mu)/k^2$. Here, the fermionic regulator takes into account that fermions have to be regularised around the Fermi surface, while the bosonic regulator includes the fact that the boson mass is twice the fermion mass. Note, that only spatial momenta $q^2 = |\vec{q}|^2$ are regularised for this type of regulator. However, a particular neat property of (4.19) is that the finite temperature Matsubara sums can be performed analytically.

4.3 Master equations

In order to solve the Wetterich equation Eq. (3.13) in practice we need to convert it into a set of coupled differential equations of the correlation functions. We therefore start from a few Master equations, namely for the inverse fermion and boson propagators and the effective average potential. The following two Sections are valid for a general regulator scheme and we only specialise to the case of Eq. (4.19) in Section 4.5.
In the next step these equation are projected appropriately to arrive at flow equations for the running couplings $\{g_k\}$.

With the definitions from Eq. (4.15), general regulators the flow equation of the effective average potential is then given by

$$\begin{aligned}\dot{\bar{V}}_k(\bar{\rho}) &= \frac{1}{2}\mathrm{Tr}\int_Q \overline{G}_\phi^Q \dot{\bar{R}}_\phi^Q - \frac{1}{2}\mathrm{Tr}\int_Q \overline{G}_\psi^Q \dot{\bar{R}}_\psi^Q \\ &= \frac{1}{2}\int_Q \frac{1}{A_\phi}\frac{L_\phi^Q\,\dot{\bar{R}}_\phi^{-Q} + L_\phi^{-Q}\,\dot{\bar{R}}_\phi^Q}{\det{}_B^Q} - \frac{1}{2}\int_Q \frac{1}{A_\psi}\frac{L_\psi^Q\,\dot{\bar{R}}_\psi^{-Q} + L_\psi^{-Q}\,\dot{\bar{R}}_\psi^Q}{\det{}_F^Q}\,.\end{aligned} \tag{4.20}$$

The (unrenormalised) flow equations can be divided into a bosonic and a fermionic contribution resulting from bosonic (B) and fermionic (F) diagrams, respectively

$$\dot{\bar{V}}(\bar{\rho}) = \dot{V}^{(B)} + \dot{V}^{(F)}\,. \tag{4.21}$$

Including the additional term of the anomalous dimension in Eq. (4.21) we find the flow for the renormalised quantities, e.g.

$$\dot{V}(\rho) = \dot{V}^{(B)} + \dot{V}^{(F)} + \eta_\phi\,\rho\,V'(\rho)\,.$$

For the flow of the inverse boson propagator in the $\{\phi_1,\phi_2\}$-basis we find

$$\begin{aligned}\dot{\bar{G}}^{-1}_{\bar{\phi}_i\bar{\phi}_j}(P) =& \frac{1}{2}\,\mathrm{Tr}\int_Q \overline{G}_\phi(Q)\,\bar{\gamma}^{(3)}_{\bar{\phi}_i BB}\,\overline{G}_\phi(Q+P)\,\bar{\gamma}^{(3)}_{\bar{\phi}_j BB}\,\overline{G}_\phi(Q)\dot{\bar{R}}_\phi(Q) \\ &+\frac{1}{2}\,\mathrm{Tr}\int_Q \overline{G}_\phi(Q)\,\bar{\gamma}^{(3)}_{\bar{\phi}_j BB}\,\overline{G}_\phi(Q-P)\,\bar{\gamma}^{(3)}_{\bar{\phi}_i BB}\,\overline{G}_\phi(Q)\dot{\bar{R}}_\phi(Q) \\ &-\frac{1}{2}\,\mathrm{Tr}\int_Q \overline{G}_\phi(Q)\,\bar{\gamma}^{(4)}_{\bar{\phi}_i\bar{\phi}_j BB}\,\overline{G}_\phi(Q) \\ &-\frac{1}{2}\,\mathrm{Tr}\int_Q \overline{G}_\psi(Q)\,\bar{\gamma}^{(3)}_{\bar{\phi}_i F|F}\,\overline{G}_\psi(Q+P)\,\bar{\gamma}^{(3)}_{\bar{\phi}_j F|F}\,\overline{G}_\psi(Q)\dot{\bar{R}}_\psi(Q) \\ &-\frac{1}{2}\,\mathrm{Tr}\int_Q \overline{G}_\psi(Q)\,\bar{\gamma}^{(3)}_{\bar{\phi}_j F|F}\,\overline{G}_\psi(Q-P)\,\bar{\gamma}^{(3)}_{\bar{\phi}_i F|F}\,\overline{G}_\psi(Q)\dot{\bar{R}}_\psi(Q)\,.\end{aligned} \tag{4.22}$$

Likewise the flow of the inverse fermion propagator is obtained, taking the Grassmannian

nature of fermions in account,

$$\begin{aligned}\dot{\bar{G}}^{-1}_{\bar{\psi}_\alpha\bar{\psi}_\beta}(P) = &\frac{1}{2}\,\mathrm{Tr}\int_Q \overline{G}_\phi(Q)\,\bar{\gamma}^{(3)}_{\bar{\psi}_\alpha B|F}\,\overline{G}_\psi(Q+P)\,\bar{\gamma}^{(3)}_{F|B\bar{\psi}_\beta}\,\overline{G}_\phi(Q)\dot{\bar{R}}_\phi(Q)\\ &-\frac{1}{2}\,\mathrm{Tr}\int_Q \overline{G}_\phi(Q)\,\bar{\gamma}^{(3)}_{BF|\bar{\psi}_\beta}\,\overline{G}_\psi(Q-P)\,\bar{\gamma}^{(3)}_{\bar{\psi}_\alpha|FB}\,\overline{G}_\phi(Q)\dot{\bar{R}}_\phi(Q)\\ &-\frac{1}{2}\,\mathrm{Tr}\int_Q \overline{G}_\psi(Q)\,\bar{\gamma}^{(3)}_{\bar{\psi}_\alpha|FB}\,\overline{G}_\phi(Q+P)\,\bar{\gamma}^{(3)}_{BF|\bar{\psi}_\phi}\,\overline{G}_\psi(Q)\dot{\bar{R}}_\psi(Q)\\ &+\frac{1}{2}\,\mathrm{Tr}\int_Q \overline{G}_\psi(Q)\,\bar{\gamma}^{(3)}_{F|B\bar{\psi}_\beta}\,\overline{G}_\phi(Q-P)\,\bar{\gamma}^{(3)}_{\bar{\psi}_\alpha B|F}\,\overline{G}_\psi(Q)\dot{\bar{R}}_\psi(Q)\,.\end{aligned} \tag{4.23}$$

Equations (4.20), (4.22) and (4.23) will be used to obtain the flow equations of the relevant couplings via an appropriate projection description in Section 4.4. Furthermore, in Chapter 6 the flow of the inverse propagators is calculated from Eq. (4.23) and after an analytical continuation to real-time the spectral functions. The three- and four-point vertices are explicitly shown in Appendix D.

4.4 Projection description for the running couplings

In this Section we derive suitable projection descriptions for the flow equations of the running couplings $\{g_k\}$ and expansion coefficients of the effective average potential $V(\rho)$. We recall that we use a derivative expansion of the inverse fermion and boson propagators

$$\begin{aligned}\overline{P}_{\psi\sigma}(Q) &= Z_{\psi\sigma}\,\mathrm{i}\,q_0 + A_{\psi\sigma}\,q^2 - \bar{\mu} = A_{\psi\sigma}\left(S_{\psi\sigma}\,\mathrm{i}\,q_0 + q^2 - \mu\right)\,,\\ \overline{P}_{\phi}(Q) &= Z_{\phi}\,\mathrm{i}\,q_0 + A_{\phi}\,q^2/2 = A_{\phi}\left(S_{\phi}\,\mathrm{i}\,q_0 + q^2/2\right)\,.\end{aligned} \tag{4.24}$$

Here we defined $S_{\psi,\phi} = Z_{\psi,\phi}/A_{\psi,\phi}$ and the renormalised chemical potential $\mu = \bar{\mu}/A_{\psi,\sigma}$. Since the effective potential is expanded in a Taylor series (here excluding an explicit contribution containing the density), we can easily project the flow equation (4.20) onto the coefficients

$$V_k(\rho) = m_\phi^2\,(\rho-\rho_0) + \frac{\lambda_\phi}{2}\,(\rho-\rho_0)^2 + \sum_{n>2}^{N}\frac{v_n}{n!}\,(\rho-\rho_0)^n\,. \tag{4.25}$$

There are several candidates for projection descriptions for the running couplings which may at a first glance seem equal. However, as the flow equation is an exact equation incorporating all orders of the effective average action, every projection neglects certain higher order couplings and thus results in different flows. We expect though that our truncation includes the most important effects and a precise projection would only yield negligible modifications. The distinction between different projection descriptions may also be used for an error estimate.

In the symmetric regime of the flow we have $\dot{\bar{m}}_\phi^2 = \dot{\bar{V}}'(\rho = 0)$ which makes place for the flow of $\dot{\bar{\rho}}_0 = -\dot{\bar{V}}'(\rho_0)/\bar{\lambda}_\phi$ in the symmetry broken regime. For the flow of higher expansion coefficients one finds

$$\dot{\bar{v}}_n = \partial_t \left(\bar{V}^{(n)}(\bar{\rho}_0) \right) = \dot{\bar{V}}^{(n)}(\bar{\rho}_0) + \bar{v}_{n+1}\, \dot{\bar{\rho}}_0 \,. \tag{4.26}$$

Using the expansion of the effective potential Eq. (4.25) together with Eq. (4.26) we then obtain the flow of the renormalised couplings via

$$m_\phi^2 = \frac{\bar{m}_\phi^2}{A_\phi} \,, \quad \rho_0 = A_\phi\, \bar{\rho}_0 \,, \quad v_n = \frac{\bar{v}_n}{A_\phi^n} \,. \tag{4.27}$$

Again this means that including a term proportional to the anomalous dimension yields the flow of the renormalised couplings in Eq. (4.27), to wit

$$\begin{aligned} \dot{m}_\phi^2 &= \eta_\phi\, m_\phi^2 + \frac{\dot{\bar{m}}_\phi^2}{A_\phi} \,, \\ \dot{\rho}_0 &= -\eta_\phi\, \rho_0 + A_\phi\, \dot{\bar{\rho}}_0 \,, \\ \dot{v}_n &= n\, \eta_\phi\, v_n + \frac{\dot{\bar{v}}_n}{A_\phi^n} \,. \end{aligned} \tag{4.28}$$

Since we restrict ourselves to purely fermionic and bosonic diagrams, we have no running of the couplings entering the fermionic propagator, yet they are obtained via the same construction. For the couplings associated with the boson propagator we make use of the derivative expansion of the inverse propagator, cf. Eq. (4.24) and arrive at

$$\begin{aligned} \dot{Z}_\phi &= -\partial_{p_0}\, \dot{\bar{G}}^{-1}_{\phi_1\phi_2}(P, \rho_0)\Big|_{P=0,\rho_0} \,, \\ \dot{A}_\phi &= 2\, \partial_{p^2}\, \dot{\bar{G}}^{-1}_{\phi_2\phi_2}(P, \rho_0)\Big|_{P=0,\rho_0} \,. \end{aligned} \tag{4.29}$$

From Eq. (4.29) the flow equations for the renormalised quantities are then given with the anomalous dimension $\eta_\phi = -\dot{A}_\phi/A_\phi$ by

$$\dot{S}_\phi = \eta_\phi\, S_\phi + \frac{\dot{Z}_\phi}{A_\phi} \,. \tag{4.30}$$

In the flow equations for the running couplings we neglected a term proportional to $\dot{\bar{\rho}}_0$ which would be generated if one took the RG-time derivative after performing the projections. Equations (4.28) and (4.30) together with the bosonic anomalous dimension are the set of coupled differential equations for our truncation, cf. Section 4.1 needed to be solved. A discussion concerning the initial conditions for this set of coupled differential equations is postponed to Section 4.7.2.

4.5 Flow equations using the optimised regulator

So far, our considerations were general and especially independent of the specific regulator scheme used. In this Section we now specialise to the case of the optimised regulator (4.19) for deriving the flow equations of the running couplings. These equations will be our main starting point in studying the BCS-BEC crossover in dimensions $2 \leq d \leq 3$ in the later Section 4.6.

4.5.1 Expansion scheme

The advantage of the optimised regulator stems from the possibility of analytically performing the Matsubara summations due to a purely spatial cutoff $q^2 = |\vec{q}|^2$.
The procedure may, however, further be simplified by interchanging the order of the derivative projection and the Matsubara summation. We therefore start again from the general form of the flow of the inverse propagators with the trace not being evaluated so that we can expand the inverse propagators $G(Q \pm P)$ in powers of p_0 and p and perform the projections afterwards.

Fermionic contributions

In this spirit we expand the inverse fermionic propagator from Eq. (4.15) according to

$$\begin{aligned} L_\psi^{Q+P} &= L_\psi^Q + \mathrm{i}\, S_\psi\, p_0 + \left(1 + R_\psi^{(1)}\right)\, \left(2\, q\, p\, x + p^2\right) + \frac{1}{2}\, R_\psi^{(2)}\, \left(2\, p\, q\, x\right)^2 \,, \\ \det{}_{\mathrm{F}}^{Q+P} &= \det{}_{\mathrm{F}}^{Q} + 2\, L_\psi^{S,Q} \left(\left(1 + R_\psi^{(1)}\right)\, \left(p^2 + 2\, p\, q\, x\right) + \frac{1}{2}\, R_\psi^{(2)}\, \left(2\, p\, q\, x\right)^2 \right) \\ &\quad + S_\psi^2\, p_0^2 + 2\, S_\psi\, p_0\, q_0 + \left(1 + R_\psi^{(1)}\right)^2\, \left(2\, p\, q\, x\right)^2 \end{aligned} \tag{4.31}$$

where the superscript S denotes the symmetrised contribution (4.14) and we defined

$$\vec{p}\,\vec{q} = p\, q\, x\,, \quad R_\psi^{(1)}(q^2) = \frac{\partial\, R_\psi}{\partial\, q^2}(q^2)\,, \quad R_\psi^{(2)}(q^2) = \frac{\partial\, R_\psi^{(1)}}{\partial\, q^2}(q^2)\,.$$

We obtain the respective expansions for momenta $Q - P$ by transforming $x \to -x$ and $p_0 \to -p_0$. In order to apply the projection descriptions in Sec. 4.4 we introduce the notation which directly act on the expansion in Eq. (4.31)

$$A^{(\pm)} = -\frac{\partial}{\partial\, p_0}\, G_\psi^{Q\pm P}\Big|_{P=0}\,, \quad B^{(\pm)} = -\frac{\partial^2}{\partial\, p^2}\, G_\psi^{Q\pm P}\Big|_{P=0}\,, \quad C^{(\pm)} = \frac{1}{2}\, \frac{\partial}{\partial\, p_0^2}\, G_\psi^{Q\pm P}\Big|_{P=0}\,.$$

With the general definition of the flow equation of the inverse propagators in Sec. 4.3 this yields the projections on the wavefunction renormalisation $S_\phi = Z_\phi / A_\phi$ and the boson

anomalous dimension

$$\begin{aligned}\dot{S}_\phi^{(F)} &= -\frac{1}{2}\int_Q \mathrm{Tr}\left(\gamma^{(3)}_{\phi_1 FF}\, A^{(+)}\, \gamma^{(3)}_{\phi_2 FF} + \gamma^{(3)}_{\phi_2 FF}\, A^{(-)}\, \gamma^{(3)}_{\phi_1 FF}\right) \frac{1}{A_\psi}\, G^Q_\psi\, \dot{\bar{R}}^Q_\psi\, G^Q_\psi\,, \\ \eta_\phi^{(F)} &= -\frac{1}{2}\int_Q \mathrm{Tr}\left(\gamma^{(3)}_{\phi_2 FF}\, B^{(+)}\, \gamma^{(3)}_{\phi_2 FF} + \gamma^{(3)}_{\phi_2 FF}\, B^{(-)}\, \gamma^{(3)}_{\phi_2 FF}\right) \frac{1}{A_\psi}\, G^Q_\psi\, \dot{\bar{R}}^Q_\psi\, G^Q_\psi\,.\end{aligned} \tag{4.32}$$

Together with the explicit forms of the three-point functions $\gamma^{(3)}$, cf. Appendix D, Equation (4.32) then yields the general flow equations given the optimised regulator with the loop integration still unevaluated

$$\begin{aligned}\dot{S}_\phi^{(F)} &= -2\,h^2\, S_\psi \int_Q \frac{\dot{\bar{R}}_\psi(q^2)}{A_\psi}\left(\frac{1}{\left(\det{}^Q_{\mathrm{F}}\right)^2} - \frac{2\,h^2\,\rho}{\left(\det{}^Q_{\mathrm{F}}\right)^3}\right), \\ \eta_\phi^{(F)} &= \frac{8\,h^2}{d}\int_Q \frac{\dot{\bar{R}}_\psi(q^2)}{A_\psi}\,\frac{q^2\,R^{(2)}_\psi}{\left(\det{}^Q_{\mathrm{F}}\right)^3}\,.\end{aligned} \tag{4.33}$$

Bosonic contributions

For the bosonic contribution with linear frequency dependence we find as before

$$\begin{aligned}L_\phi^{Q+P} &= L_\phi^Q + i\,S_\phi\,p_0 + \left(\frac{1}{2} + R^{(1)}_\phi\right)\left(2\,p\,q\,x + p^2\right) + \frac{1}{2}\,R^{(2)}_\phi\,\left(2\,p\,q\,x\right)^2\,, \\ \det{}^{Q+P}_{\mathrm{B}} &= L_\phi^{-(Q+P)}\,L_\phi^{Q+P} - \left(\rho\,V''\right)^2 + \left(\det{}^Q_{\mathrm{B}} - L_\phi^{-Q}\,L_\phi^Q + \left(\rho\,V''\right)^2\right)\,.\end{aligned} \tag{4.34}$$

Given the flow equations for the propagators in Sec. 4.3 and the explicit forms of the three-point functions $\gamma^{(3)}$, cf. Appendix D, Equation (4.34) then results in the flow equations for a linear frequency dependence

$$\begin{aligned}\dot{S}_\phi^{(B)} = &-4\,S_\phi\,\rho\,V''\int_Q \frac{\dot{\bar{R}}_\phi(q^2)}{A_\phi}\left(\frac{V'' + \rho\,V^{(3)}}{\det{}^2_{\mathrm{B}}(Q)}\right. \\ &\left. + \frac{2\,\rho\,V''\left[\rho\,V''\left(V'' + \rho\,V^{(3)}\right) - \left(2\,V'' + \rho\,V^{(3)}\right)\,L^S_\phi(Q)\right]}{\det{}^3_{\mathrm{B}}(Q)}\right),\end{aligned} \tag{4.35}$$

$$\eta_\phi^{(B)} = 4\,\rho\,\left(V''\right)^2\int_Q \frac{\dot{\bar{R}}_\phi(q^2)}{A_\phi}\left(\frac{1 + 2\,R^{(1)}_\phi + 4\,q^2\,x^2\,R^{(2)}_\phi}{\det{}^2_{\mathrm{B}}(Q)} - \frac{2\,q^2\,x^2\,\left(1 + 2\,R^{(1)}_\phi\right)^2\,L^S_\phi(Q)}{\det{}^3_{\mathrm{B}}(Q)}\right).$$

Equations (4.33) and (4.35) together with the flow equations of the couplings derived from the effective action are then (after momentum integration) solved numerically and thus define our theory at hand.

The loop integrations still need to be performed in (4.33) and (4.35). For this we use the Matsubara formalism outlined in Section 3.3 for the summation over the discrete Matsubara

frequencies at finite temperature. The spatial momentum integration has to account for the fermionic regularisation around the Fermi surface. The explicit calculations are moved to Appendix E.

4.5.2 Final flow equations

After performing the Matsubara sums and the momentum integrations in Appendix E the overall flow equations in our truncation can be cast into the form

$$\begin{aligned}\dot{V}^{(F)}(\rho) &= -\frac{16\,v_d}{d}\,k^{d+2}\,\ell_F^{(1,1)}\,,\\ \dot{V}^{(B)}(\rho) &= \frac{8\,v_d\,2^{d/2}}{d}\,k^{d+2}\,\ell_B^{(1,1)}\,.\end{aligned} \tag{4.36}$$

The fermionic contributions to the boson propagator are found to be

$$\begin{aligned}\dot{S}_\phi^{(F)} &= -\frac{16\,h^2\,v_d}{d}\,k^{d-4}\left(\ell_F^{(0,2)} - 2\,w_3\,\ell_F^{(0,3)}\right)\,,\\ \eta_\phi^{(F)} &= \frac{16\,h^2\,v_d}{d}\,k^{d-4}\,\ell_{F,2}^{(0,2)}\,,\end{aligned} \tag{4.37}$$

while the bosonic contributions are given by

$$\begin{aligned}\dot{S}_\phi^{(B)} =& -\frac{32\,S_\phi}{d}\,\rho\,V''\,v_d\,2^{d/2}\,k^{d-4}\Big[\left(V''+\rho V^{(3)}\right)\ell_B^{(0,2)}\\ &+2\left(\rho V''\right)^2\left(V''+\rho V^{(3)}\right)k^{-4}\ell_B^{(0,3)} - 2\rho V''\left(2\,V''+\rho\,V^{(3)}\right)\,k^{-2}\,\ell_B^{(1,3)}\Big],\end{aligned} \tag{4.38}$$

$$\eta_\phi^{(B)} = 8\,\rho\,\left(V''\right)^2\,\frac{v_d\,2^{d/2}}{d}\,k^{d-4}\,\ell_{B,2}^{(0,2)}\,.$$

Here we used the definitions for fermionic contributions

$$\ell_F^{(n,m)}\left(\tilde{\mu},\tilde{T},w_3\right) = \begin{cases}\ell_2(\tilde{\mu})\,\mathcal{F}_m\big(\sqrt{1+w_3}\big) & n \text{ even}\\ \ell_1(\tilde{\mu})\,\mathcal{F}_m\big(\sqrt{1+w_3}\big) & n \text{ odd}\end{cases} \tag{4.39}$$

and

$$\ell_{F,2}^{(n,m)}\left(\tilde{\mu},\tilde{T},w_3\right) = \begin{cases}\ell_3(\tilde{\mu})\,\mathcal{F}_m\big(\sqrt{1+w_3}\big) & n \text{ even}\\ \ell_1(\tilde{\mu})\,\mathcal{F}_m\big(\sqrt{1+w_3}\big) & n \text{ odd}\end{cases}\,, \tag{4.40}$$

where we made use of $w_1 = V'/k^2$ and $w_2 = \rho\,V''/k^2$, as well as $w_3 = h^2\,\rho/k^4$. For bosonic diagrams we defined

$$\ell_B^{(n,m)}\left(\tilde{T},w_1,w_2\right) = \frac{1}{S_\phi^{2m}}\left(1-\frac{\eta_\phi}{d+2}\right)\,(1+w_1+w_2)^n\,\mathcal{B}_m\Big(\sqrt{(1+w_1)(1+w_1+2\,w_2)}/S_\phi\Big)$$

and

$$\ell_{B,2}^{(0,m)}\left(\tilde{T}, w_1, w_2\right) = \frac{1}{S_\phi^{2m}}\,\mathcal{B}_m\Big(\sqrt{(1+w_1)(1+w_1+2\,w_2)}/S_\phi\Big) = \ell_B^{(0,m)}\Big|_{\eta_\phi=0}\,.$$

$\mathcal{F}_m(z)$ and $\mathcal{B}_m(z)$ label the fermionic and bosonic Matsubara sums of order m given in (E.1) and (E.3), respectively. The functions ℓ_i are defined as in Eq. (E.5)

$$\begin{aligned}
\ell_1(x) &= \theta(x+1)\,(x+1)^{d/2} - \theta(x-1)\,(x-1)^{d/2}\,,\\
\ell_3(x) &= \theta(x+1)\,(x+1)^{d/2} + \theta(x-1)\,(x-1)^{d/2}\,,\\
\ell_2(x) &= \ell_3(x) - 2\,\theta(x)\,x^{d/2}\,,
\end{aligned} \tag{4.41}$$

and the d-dimensional volume integral is given by $v_d^{-1} = 2^{d+1}\,\pi^{d/2}\,\Gamma(d/2)$.

The flow of the density $n = n_{k\to 0}$ is approximated via an expansion of the effective potential (4.7) with respect to the offset chemical potential $\delta\mu$ with $\mu = \mu_0 + \delta\mu$ according to (4.9) and (4.8). The differentiation with respect to μ acts rather on $\delta\mu$ as the reference chemical potential is fixed

$$\dot{n}_k = -\frac{\partial\,\dot{V}}{\partial\,\delta\mu}\,. \tag{4.42}$$

According to the Master equation for the effective average potential (4.20) we now expand $L_\psi^{S,Q}$ and $\det_{\mathrm{F}}^{Q}$ in terms of $\delta\mu$ while the fermionic cutoff still regularises around the Fermi surface, i.e. the reference chemical potential μ_0. As mentioned below Eq. (4.9) we will improve on this approximation in Chapter 7 in order to obtain quantitative results.

The (4.36) – (4.38) together with Eq. (4.42) comprise the set of coupled differential equations we need to solve starting at an ultraviolet scale Λ to the infrared $k \to 0$. We will extend them to finite volume in the next Section 4.6 and comment on the procedure for their solution in Section 4.7.

4.6 Flow equations for finite volume

The flow equations obtained for the Litim-type regulator in Section 4.5 only account for a fixed dimension d. Here, we extend the calculation to a confined system by means of a compactifation of one spatial dimension. As we will argue in Chapter 5 the Fermi gas is then essentially in a dimensional crossover from a three-dimensional to two-dimensional system where we define a confinement length scale L. By adopting periodic boundary conditions we restrict our system to a torus in one spatial direction

$$\psi(L) = \psi(0)\,.$$

Note, that anti-periodic boundary conditions do not yield a two-dimensional limit, as is discussed in Section 5.1. The compactification results in a 'spatial Matsubara sum' over

discrete momenta $k_n = 2\pi n/L$ with $n \in \mathbb{Z}$. Accompanying this quantisation of energy levels the bosonic and fermionic regulators are modified accordingly, cf. Appendix F, and thus, the d-dimensional spatial integration splits up into a sum over the discrete momenta k_n and a momentum integral in $d-1$ dimensions

$$\int \frac{d^d\, q}{(2\,\pi)^d} = \frac{1}{L} \sum_{k_n} \int \frac{d^{d-1}\, q}{(2\,\pi)^{d-1}}\,.$$

We therefore find that all bosonic flow equations of Section 4.5.2 still hold when applying the replacements

$$\left(1 - \frac{\eta_\phi}{d+2}\right) \to C_L\,, \qquad d \to d-1\,,$$

where we defined

$$C_L = \frac{1}{L} \sum_{k_n} \left(1 - \frac{k_n^2}{2\,k^2}\right)^{d/2} \left(1 - \frac{\eta_\phi}{d+2}\left(1 - \frac{k_n^2}{2\,k^2}\right)\right) \theta\left(k^2 - \frac{k_n^2}{2}\right)\,.$$

The fermionic flow equations for finite volume with periodic boundary conditions can then be inferred from the d-dimensional case in Section 4.5.2 with the replacement

$$\ell_i \to \ell_{i,L} = \frac{k}{\tilde{L}} \sum_{k_n} \ell_i\,, \qquad d \to d-1\,,$$

where the ℓ_i where defined in Eq. (4.41). We show the explicit form of C_L and $\ell_{i,L}$ in Appendix F.

The generalisations of the flow equations from Section 4.5.2 given here to a system confined to a torus of circumference L constitute the starting point for our discussion of the dimensional crossover from three to two dimensions in Chapter 5. The set of coupled flow equations is then solved numerically enabling us to gain knowledge about thermodynamic quantities, especially the equation of state and the finite temperature phase diagram for a arbitrary confinement length L.

4.7 Solving the flow equations

Here we shall briefly comment on solving the flow equations as given in Sec. 4.5.2 and 4.6. The flow equations as given above constitute a set of coupled differential equations which can, with the exception of the vacuum case, cf. Section 3.4.1, only be solved numerically. In particular, we are interested in determining the superfluid gap Δ and the equation of state for the density μ/ε_F. The superfluid gap is, according to our action in Eq. (4.1), given by

$$\Delta = \lim_{k\to 0} \Delta_k = \left(h_k^2\, \rho_{0,k}\right)^{1/2}\,,$$

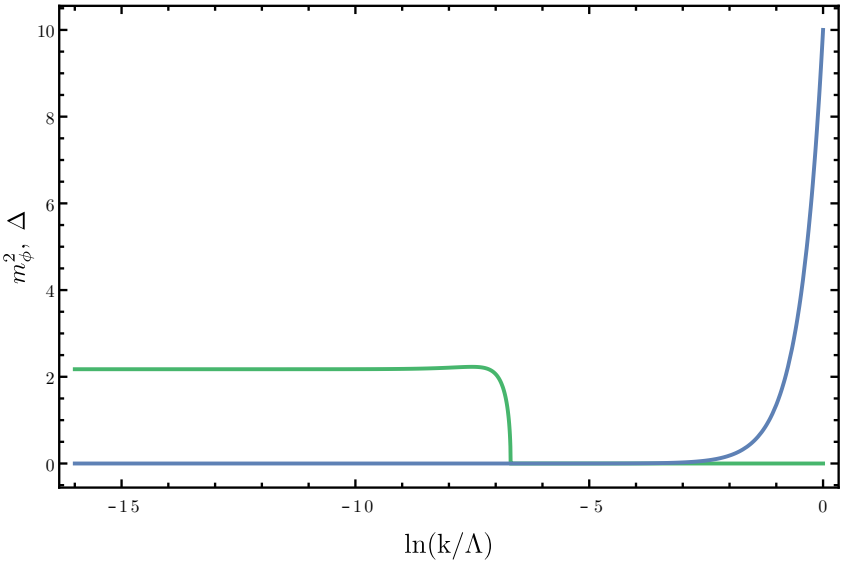

Figure 4.3: The typical (zero temperature) running of the bosonic mass m_ϕ^2 (in blue) and the gap parameter Δ (in green) with respect to the RG time $t = \ln(k/\Lambda)$. The flow is initialised at the ultraviolet scale Λ and runs towards the infrared $k \to 0$. The gap Δ is generated in the symmetry broken phase, where the bosonic mass m_ϕ^2 vanishes. Here, all contributions to the running of the couplings stem from infrared Goldstone fluctuations. At unitarity, $a_{3D} = \infty$, the units are chosen such that $\mu = 1$ and we rescaled the curves for better visibility. In these units, the phase transition occurs at $t \simeq -6.8$ and many-body effects strongly influence the physics at $k^2 \simeq \mu$ which is equivalent to $t \simeq -6.9$ in this plot.

with h_k being the scale dependent Feshbach coupling and $\rho_{0,k}$ the scale dependent minimum of the effective potential. The gap constitutes the order parameter for the superfluid phase. At zero temperature the superfluid ground state yields in a non-zero $\rho_{0,k\to 0}$ resulting in a non-vanishing gap $\Delta_{k\to 0} > 0$. At finite temperature, long range order may be destroyed by thermal fluctuations such that the gap vanishes $\Delta = 0$ and one arrives at the normal phase. In addition, there exists a temperature regime at which the intermediate $\rho_{0,k>0}$ is non-zero, but vanishes for $k \to 0$. This is often called the precondensation region. Concerning the nomenclature, we will use superfluid gap, gap parameter and simply gap interchangeably in the following.

4.7.1 Numerical procedure

The set of coupled differential equations for the projected flow equations is evaluated numerically for both zero and finite temperature. However, it is a useful feature of the functional renormalisation group that for large scales $k^2 \gg T$ the finite temperature flow can be approximated by the zero temperature system [59]. For a practical computation we choose $k_{\text{switch},T} = 6\,\pi\,T$, i.e. we follow the zero temperature flow until $k_{\text{switch},T}$, where

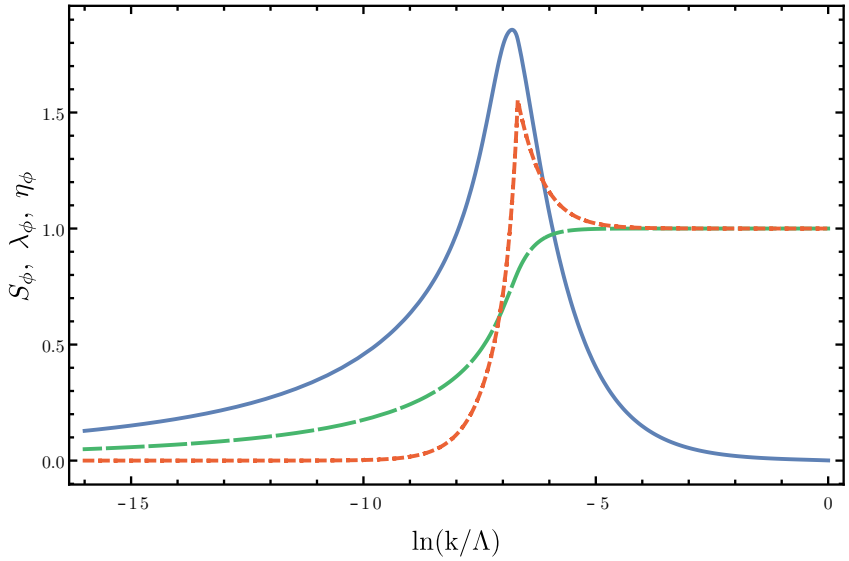

Figure 4.4: The typical (zero temperature) running of the bosonic mass S_ϕ (in blue), the bosonic coupling λ_ϕ (in green) and the bosonic anomalous dimension η_ϕ (in red) with respect to the RG time $t = \ln(k/\Lambda)$. The units are chosen such that $\mu = 1$ at unitarity $a_{3D} = \infty$. For better visibility we rescale the curves.

the temperature starts to become an important scale. Afterwards we switch to the finite temperature flow equations.

The critical temperature is determined as the largest temperature for which the gap of the fermion spectrum is non-vanishing. Numerically, we use the following algorithm

$$0 < \Delta_{t_{\text{final}}}(T_c, \mu, a) < \frac{1}{100}\Delta_{t_{\text{final}}}(T = 0, \mu, a) \ . \tag{4.43}$$

Using this algorithm is very efficient as it accounts for both the large gap on the BEC-side, as well as for the smaller gap on the BCS-side (especially in the three-dimensional case). It was checked numerically that a further limitation to $< 1\%$ of the zero temperature gap yields identical results in $d \leq 3$ within the numerical precision.

For a three-dimensional Fermi gas we choose for the ultraviolet cutoff $\Lambda/\sqrt{\mu_{\text{mb}}} = 1000$ in the following, with $\mu_{\text{mb}} = \mu - \varepsilon_B/2$ in the many-body problem, cf. Section 3.4.1. This is to be slightly modified for the case of the dimensional crossover, as we will detail in Section 5.3.

Hence, solving the flow equations for the couplings necessitates correct initial conditions at the ultraviolet scale Λ.

4.7.2 Initial conditions and universality

In three dimensions the running couplings approach fixed points in the renormalisation group flow of the Fermi gas. As a result, the macrophysics (on the length scales of the

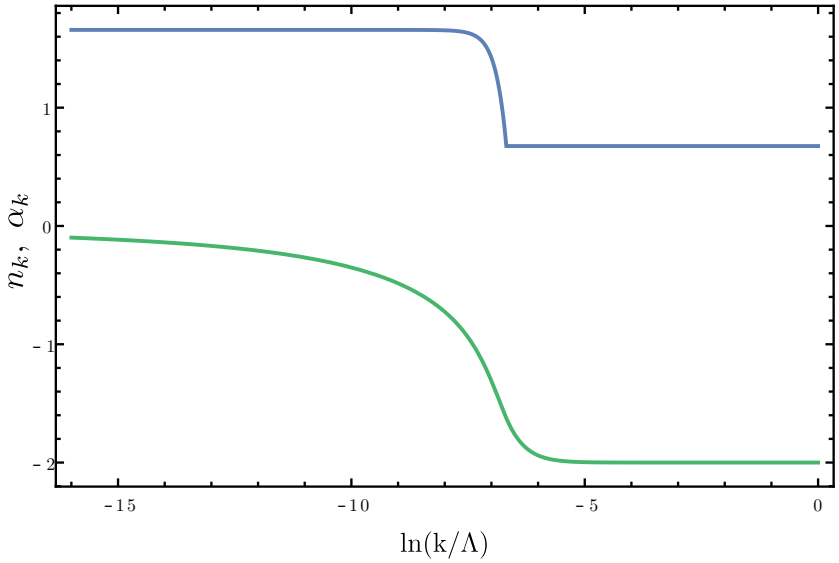

Figure 4.5: The typical running for the density n_k (blue curve) and α_k (green curve) with respect to the RG time $t = \ln(k/\Lambda)$ for a truncation including these couplings explicitly. At unitarity, $a_{3D} = \infty$, with the units are chosen such that $\mu = 1$ we rescaled the curves for better visibility.

inter-particle spacing) becomes independent of the microphysics (on the molecular scales) to a large extent, cf. e.g. [53, 59].

When reaching the fixed points, the system loses its memory of the microphysics with its initial conditions. Consequently, the initial conditions of the running couplings are irrelevant and we may essentially start at the fixed point values in the ultraviolet. Even if we had not done so, they would be immediately generated.

An exception constitutes the bosonic mass term m_ϕ^2 whose fixed point is unstable towards the infrared. Hence, for the effective potential we set as initial condition in the ultraviolet

$$V_\Lambda(\rho) = (\nu_\Lambda - 2\,\mu)\ \rho\,.$$

As mentioned in Section 3.4.2 it is advantageous to artificially split the chemical potential μ into a vacuum component μ_{vac} and a many-body contribution μ_{mb} such that the vacuum part μ_{vac} equals half the binding energy of a bosonic dimer $\varepsilon_B/2$ in three spatial dimensions. In Section 3.4.2 we described how the detuning ν_Λ, the chemical potential μ and the Feshbach coupling h_Λ are related to the experimental parameters via an appropriate vacuum renormalisation. In Section 5.2 we will comment on the case of the dimensional crossover.

In three dimensions, with these initial conditions we show the characteristic running of the couplings in Fig. 4.3 for the rescaled bosonic mass m_ϕ^2 and the gap Δ and for the rescaled couplings S_ϕ, λ_ϕ and η_ϕ in Fig. 4.4 at zero temperature and unitarity, $a_{3D}^{-1} = 0$. For a truncation including the density n_k and α_k explicitly, cf. Eq. (4.9), the initial condition

for the density has to chosen as $n_\Lambda = \mu^{3/2}/(3\pi^2)$ according to the definition of the Fermi momentum in three dimensions. Their running is illustrated in Fig. 4.5. For better visibility we rescaled the curves and find that all couplings saturate quickly towards the infrared at sufficiently small k-scales.

CHAPTER 5

Dimensional crossover

This Chapter is in parts based on Ref. [1].

Lower-dimensional systems are of particular interest both in condensed matter and statistical physics as they feature a pronounced influence of fluctuations. Furthermore, they are of experimental and technological importance with examples ranging from high temperature superconductors over layered semiconductors to graphene. Disentangling the effects of the dimensionality from other many-body physics effects constitutes a key challenge in the study of systems of reduced dimensionality.

With the recent progress in trapping ultracold atomic gases in quasi-two-dimensional geometries [61, 62] both zero [63–65] as well as finite temperature effects [63, 66–71] have been measured. Hereby, strongly anisotropic trapping potentials on the one hand and one-dimensional optical lattices one the other hand allow for the experimental realisation of quasi-two-dimensional quantum gases.

For example, the algebraic correlations associated with the Berezinskii–Kosterlitz–Thouless (BKT) phase transition in (quasi-) two-dimensional systems have been observed in bosonic [66, 69, 72–75], as well as fermionic systems [67, 76]. In addition, (quasi-) two-dimensional systems exhibit the breaking of the scale invariance in the strongly interacting regime of the BCS-BEC crossover. Here, extensive progress both in theory [77–84], as well as in experiment [64, 85, 86] has been achieved in recent years. For a fRG study of the BKT transition see e.g. [121].

Due to an insufficient degree of anisotropy in the experimental setup one may not be restricted to a particular dimension, but finds oneself in a dimensional crossover without a well-defined dimensionality. Apart from being an undesired effect for the investigation of pure two-dimensional systems, the crossover may also lead to new materials with physically interesting properties.

In this Chapter we study the dimensionality behaviour of ultracold Fermi gases, specifically the BCS-BEC crossover. A comparable quasi-two-dimensional setup has been studied

in [122, 123] in a mean-field approach, for a Fermi gas at unitarity and zero temperature in [124], using the Luttinger-Ward approach in two dimensions in [125] and using Quantum Monte Carlo (QMC) calculations in two dimensions in [126]. Furthermore, two-dimensional fermionic systems have been addressed in [127–134].

Apart from featuring the transition to the superfluid phase, the normal-state 'pseudo-gap' behaviour can also be studied within the BCS-BEC crossover. Here, the onset of superfluidity and pairing occurs at different temperatures, i.e. the density of states is partially gapped and the dispersion relation is BCS-like for a range of temperatures above the critical temperature. The system essentially retains some features of the broken superfluid phase also in the symmetric normal phase without exhibiting superfluidity. This pairing at high temperatures has been studied both experimentally, e.g. in [70, 135], as well as theoretically, e.g. in [136–138].

Moreover, a BCS-BEC crossover can also be found in confined superconducting systems, where the crossover is induced by tuning the chemical potential to a band edge in multi-band superconductors. The size-induced molecule-like pairing has both been studied theoretically [139–142], as well as experimentally [143]. Here, the confinement of superconducting materials (e.g., in the form of monolayer systems) results in shape resonances where an increased temperature, (superconducting) gap, as well as intrapair correlation length are present. In addition, the confinement leads to a step in the density of states which gives rise to a change in the topology of the Fermi surface, a so-called Lifshitz transition, and is another factor in an increased critical transition temperature [144–149]. For a 1d-2d crossover see e.g. [150].

We investigate the dimensional crossover from three to two spatial dimensions for ultracold Fermi gases by means of the functional renormalisation group. For a study of non-relativistic bosonic systems, see [117]. In particular, we are interested in the critical temperature for the superfluid transition over the BCS-BEC-crossover in dependence of the dimensionality.

The dimensional crossover is achieved by compactifying the 'transverse' z-direction by a potential well of length L. The dimensional crossover can then essentially be observed by varying the confinement length L. We discuss (anti-)periodic boundary conditions, as well as a confinement to a box with boundaries fixed to zero. The compactification leads to a discrete momentum spectrum in z-direction. The choice of the boundary conditions is crucial for a well-defined two-dimensional limit. It also influences the mapping between three- and two-dimensional parameters of the Fermi gas. Both aspects are discussed in detail in Section 5.1. The initial conditions and numerical procedure are presented in Sections 5.2 and 5.3. We discuss some aspects of the dependence on the final infrared scale in Sec. 5.4. In Section 5.5 the results for the equation of state and the gap parameter in the dimensional crossover at zero temperature are discussed. The finite temperature phase diagrams with respect to the dimensionality and a comparison to experiment are addressed

in Section 5.6, before concluding in the end.

5.1 Function space and boundary conditions

The choice of the boundary conditions plays a crucial role in arriving at the correct two-dimensional physics. The dimensional crossover is implemented by compactifying the 'transverse' z-direction by a potential well of length L,

$$V_{\text{box}}(z) = \begin{cases} 0 & 0 \leq z \leq L \\ \infty & \text{else} \end{cases} . \tag{5.1}$$

One may choose (anti-)periodic boundary conditions

$$\psi(x, y, z = 0) = \pm\psi(x, y, z = L) ,$$

or restrict oneself to a box

$$\psi(x, y, z = 0) = \psi(x, y, z = L) = 0 .$$

The compactification leads to a discrete momentum spectrum in z-direction. For periodic boundary conditions the respective energies, $E_z = \frac{\hbar q_z^2}{2M}$, are discrete with $q_z \to k_n$

$$k_n = \frac{2\pi n}{L}, \qquad n \in \mathbb{Z} ,$$

which includes a zero mode $k_0 = 0$ with vanishing energy $E_{\text{min}} = 0$. In turn, for anti-periodic boundary conditions one finds $k_n = (2n + 1)\pi/L$ with $n \in \mathbb{Z}$ and with a lowest mode $|k_0| = \pi/L$ with a finite energy $E_{\text{min}} = \hbar\pi^2/(2ML^2)$. Finally, confining the Fermi gas inside a box leads to $k_n = \pi n/L$ with a vanishing energy $E_{\text{min}} = 0$.

The non-vanishing zero point energy for anti-periodic boundary conditions results in a gap in the evaluation of the (discrete) mode sum at zero temperature. Consequently, anti-periodic boundary conditions do not yield the two-dimensional limit for vanishing length $L \to 0$. For a relativistic system, the dispersion relation allows one to identify the length of the potential well L with the inverse temperature $1/T$ in the evaluation of the discrete mode sum at zero temperature. As a result, $T = 0$ and $L = L_0$ gives the same result as $T = 1/L_0$ and $L = 0$, i.e. the zero length limit $L \to 0$ at zero temperature $T = 0$ corresponds to the limit of infinite temperature $T \to \infty$ at zero length $L = 0$. For a non-relativistic system, the situation is less simple since the dispersion relation allows no clear mapping between the temperature and the length of the system. Nevertheless, it is clear that anti-periodic boundary conditions do not admit a two-dimensional limit for $L \to 0$.

Here we choose periodic boundary conditions, which result in a two-dimensional limit for vanishing length $L \to 0$. All modes with $n \neq 0$ have for $L \to 0$ a large gap and can be integrated out. In general, the three-dimensional system with finite L can be viewed

as a two-dimensional system with infinitely many fermions as 'modes', one for each n. Integrating out the modes with $n \neq 0$ reduces the system to a 'single two-dimensional fermion', the one for $n = 0$.

This transition maps the parameters of the three-dimensional theory to the ones of an effective two-dimensional theory. For $L \to 0$ this map may induce large changes for characteristic quantities as the chemical potential μ or the scattering length a. This can lead to shifts in fractions including ε_F and T_F, as well as in the crossover parameter. In experiment, the three-dimensional quantities are generally the ones available, and we will typically use them for our discussion. However, when comparing to results obtained from computations in two-dimensions, the matching between three- and two-dimensional parameters becomes important. In the present discussion we do not deal with this issue, but we should keep it in mind when comparing with two-dimensional results.

Experimentally realistic confinement potentials, used in most ultracold atom experiment, such as [67] and [68], are implemented by using harmonic trapping potentials. Here, the function space consists of Hermite polynomials. Heuristically, our choice for the confinement potential is a limiting case. In particular, observables that are independent of the different boundary conditions studied here should be the same for the harmonic trap.

5.1.1 Dimensional reduction

In order to obtain a system within the dimensional crossover from three to two dimensions, we initialise the renormalisation group (RG) flow at ultraviolet cutoff scale $k = \Lambda$ where the effective action Γ_Λ coincides with the microscopic action of a three-dimensional ultracold Fermi gas. By delimiting the z-direction of the system via a potential well of length L, we introduce an additional scale to the three-dimensional system. By following the RG flow as a function of k for a given length scale L, one observes that the contribution of modes with $k_n^2 \gg k^2$ is suppressed by powers of k^2/k_n^2. These modes decouple and effective dimensional reduction is achieved automatically once $k \ll 2\pi/L$. This is very similar to computations in finite temperature quantum field theories, where an effective dimensional reduction is also realised by solutions of the flow equations, cf. e.g. [151]. Following the RG from $k = \Lambda$ to $k = 0$, the flow always makes a transition from a three-dimensional regime to a two-dimensional one. For this purpose the UV scale is always chosen such that $\Lambda \gg (L^{-1}, \mu^{1/2}, T^{1/2})$. The flow equations become effectively two-dimensional for $k \ll 2\pi/L$, while the physical system is effectively two-dimensional if L^{-1} is much larger than all other many-body scales [117].

To incorporate the effects of the compactification in transversal z-direction given by the potential well in (5.1), the regulators in (4.19) are modified according to

$$\vec{q}^2 = \hat{q}^2 + q_z^2 \to \hat{q}^2 + k_n^2 \,,$$

where k_n is chosen according to the boundary conditions and $\hat{q}^2$ denotes the square of the

x- and y-components of the momentum. Note that while in three dimensions all couplings tend to saturate quickly at sufficiently small k-scales [59], the saturation behaviour is much slower for $d < 3$. As a consequence, we choose a much smaller final k-scale in the infrared (cf. Appendix 5.4), while in three dimensions it is possible to stop the RG-flow earlier.

In order to display the confinement in transversal direction we introduce the dimensionless length parameter $L\sqrt{\mu_{\mathrm{mb}}}$ of the potential well, where $\mu_{\mathrm{mb}} = \mu - \varepsilon_B/2$ denotes the chemical potential for the three-dimensional gas with half the dimer binding energy $\varepsilon_B/2$ being subtracted.

5.2 Initial conditions

As described in Section 4.7.2 for three dimensions the running couplings approach fixed points in the renormalisation group flow of the Fermi gas, resulting in a macrophysics independent of the microphysics.

These fixed points lead to a loss of the specific microphysics with its initial conditions. As a consequence, the initial conditions of the running couplings are, except for the bosonic mass term, irrelevant and we may essentially start at the fixed point values in the ultraviolet.

Since the RG flow for a system in reduced dimensions is initialised at an UV scale where the Fermi gas is described by the three-dimensional classical action, these considerations can also be applied to the study of systems inside the dimensional crossover. We therefore choose the fixed point values of the three-dimensional Fermi gas as our initial conditions.

5.3 Numerical procedure

The general numerical procedure is given in Sec. 4.7.1. Here, we comment on solving the flow equations within the dimensional crossover. The flow equations, underlying the results at zero and at finite temperature discussed in this Chapter, are obtained analytically with periodic boundary conditions for both bosonic and fermionic fields inside the potential well. The flow equations are given explicitly in Chapter 4.

As described in Sec. 4.7.1, we use that, within the fRG, the finite temperature flow for large scales $k^2 \gg T$ can be approximated by the zero temperature system. Likewise, the Fermi gas confined to a trap can be regarded as an unconfined system for large scales $k \gg L^{-1}$. We follow the unconfined flow until $k_{\mathrm{switch},L}$, where the (inverse) confinement length starts to become an important scale. At this scale we switch to the confined flow equations. Here we choose $k_{\mathrm{switch},L} = 50/L$, which significantly decreases the runtime of the computation. The agreement of the results with and without splitting the flow in zero and finite temperature, as well as unconfined and confined flow equations, was checked numerically.

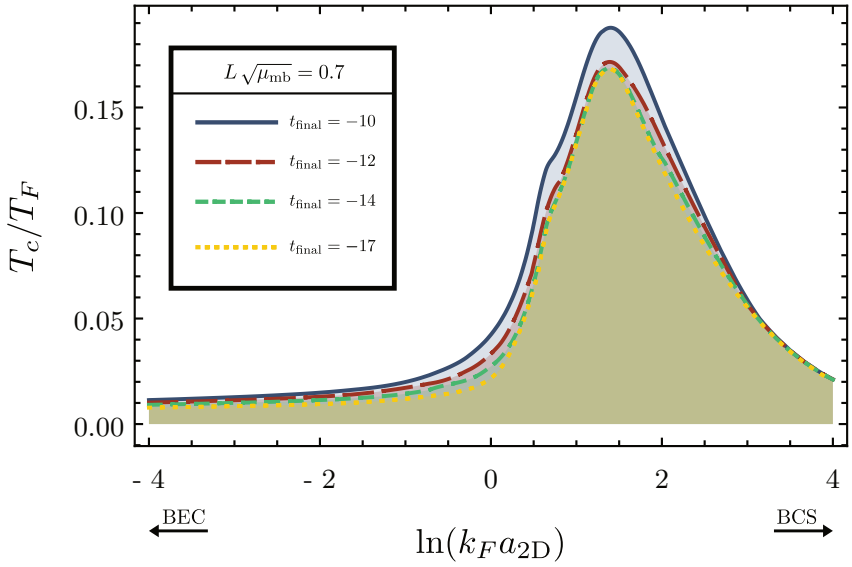

Figure 5.1: Phase diagram in terms of T_c/T_F for a confinement length of $L\sqrt{\mu_{\rm mb}} = 0.7$. Here the dependence on the final IR scale of the RG-flow is shown with (from top to bottom) $t_{\rm final} = -10$ in solid-blue (solid line dark grey), $t_{\rm final} = -12$ in long-dashed-red (long-dashed line in grey), $t_{\rm final} = -14$ in dashed-green (dashed line in lighter grey) and $t_{\rm final} = -17$ in dotted-yellow (dotted line in light grey). It is most pronounced in the strongly-interacting region around $\ln(k_F\, a_{2D}) \sim 1$, while being much less significant in the BEC- and BCS-limits. A smaller IR-scale leads to a reduced critical temperature.

The determination of the critical temperature follows (4.43) and is the largest temperature for which the gap of the fermion spectrum is non-vanishing. Within the dimensional crossover with corresponding confinement length L, we use

$$0 < \Delta_{t_{\rm final}}(T_c, \mu, a, L) < \frac{1}{100}\Delta_{t_{\rm final}}(T = 0, \mu, a, L)\ .$$

As in the three-dimensional system it was checked numerically that a further limitation to $< 1\%$ of the zero temperature gap yields identical results in $2 \lesssim d \lesssim 3$ within the numerical precision and thus represents a very efficient algorithm.

5.4 Dependence on the infrared RG-flow scale

As mentioned in Section 5.1.1 the running of the couplings does not saturate as quickly in $d < 3$ as for a three-dimensional system in our RG-flow. In Fig. 5.1 we show this IR-scale dependence exemplary for a confinement length of $L\sqrt{\mu_{mb}} = 0.7$, with the dimensionless length parameter $L\sqrt{\mu_{\rm mb}}$ introduced in Sec. 5.1.1. We find that it is most pronounced in the strongly interacting region around $\ln(k_F\, a_{2D}) \sim 1$, while being much less significant in the BEC- and BCS-limits. Seeing that the critical temperature is reduced for a smaller

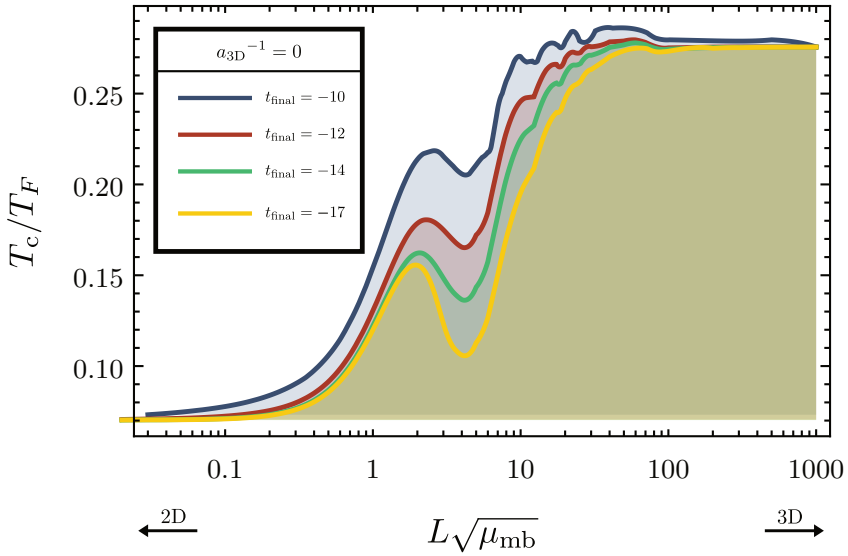

Figure 5.2: Critical temperature T_c/T_F at fixed three-dimensional scattering length $a_{3D}^{-1} = 0$ over the dimensional crossover from two- to three-dimensions. Here we show the dependence on the final IR scale of the RG-flow with (from top to bottom) $t_{\text{final}} = -10$ in blue (dark grey), $t_{\text{final}} = -12$ in red (grey), $t_{\text{final}} = -14$ in green (lighter grey) and $t_{\text{final}} = -17$ in yellow (light grey).

IR-scale requires that we have to choose a sufficiently small final k-scale when solving our flow equations.

The dependence on the final RG-flow scale in the infrared across the dimensional crossover can be seen in Fig. 5.2 for a three-dimensional scattering length of $a_{3D}^{-1} = 0$. As we will explain below, the dips within the crossover from two- to three-dimensions are caused by the chosen boundary conditions and are related to the step-like structure of the density of states for a confined system [123].

As shown in Fig. 5.3 the maximum critical temperature $T_c^{\max}/T_F$ within the (quasi-) two-dimensional BCS-BEC crossover for a confinement length scale $L\sqrt{\mu_{\text{mb}}} = 0.7$ converges for $t_{\text{final}} \leq -16$ (with $t = \ln(k/\Lambda)$). For this reason we choose a final IR-scale of $t_{\text{final}} = -17$ for all our calculations such that sufficiently converged results should be obtained.

5.5 Dimensional crossover at zero temperature

As expected in Section 5.1, imposing anti-periodic boundary conditions for fermionic fields $\psi(x)$ results in a suppression of the fermionic flow for small confinement length scales $L\sqrt{\mu_{\text{mb}}} \sim 2$. Consequently, no phase transition on the BCS-side of the crossover can be found. The BEC-side, however, is not affected by this choice. This finding reaffirms us in the use of periodic boundary conditions, also concerning fermionic fields.

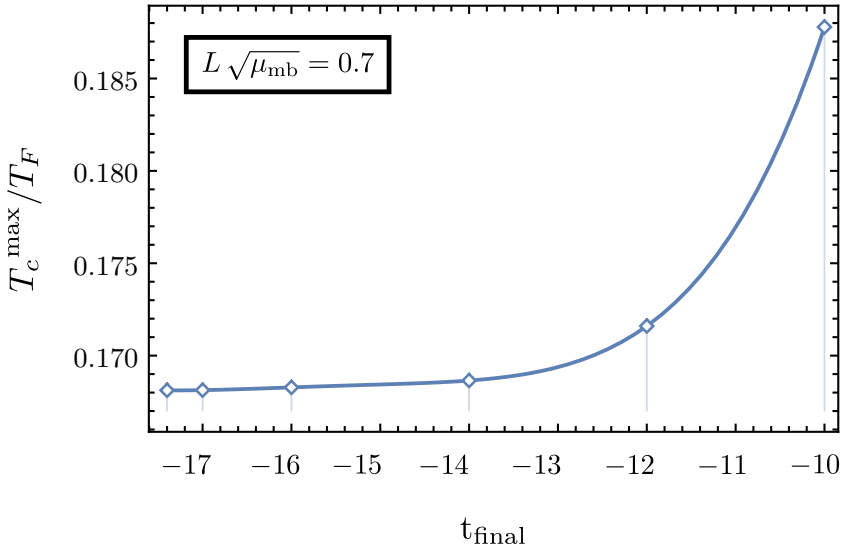

Figure 5.3: Maximum critical temperature $T_c^{\max}/T_F$ within the (quasi-) two-dimensional BCS-BEC crossover for a confinement length scale $L\sqrt{\mu_{\mathrm{mb}}} = 0.7$ and different final k-scales in the infrared. A convergence for $t_{\mathrm{final}} \leq -16$ can be inferred.

In Fig. 5.4 the equation of state is shown as a function of the three-dimensional crossover parameter $(k_F\, a_{3\mathrm{D}})^{-1}$, which can be interpreted as the inverse concentration of the Fermi gas. For large confinement length scales $L\sqrt{\mu_{\mathrm{mb}}}$ the three-dimensional result is recovered, while the equation of state in dependence of the transversal extension starts to saturate only at the order of $L\sqrt{\mu_{\mathrm{mb}}} = 10^{-4}$ for a two-dimensional limit.

For better comparison to experiment the equation of state is also displayed in Fig. 5.5 with respect to the two-dimensional crossover parameter $\ln(k_F\, a_{2\mathrm{D}})$. Here the (quasi-) two-dimensional scattering length $a_{2\mathrm{D}}$ is calculated by [117]

$$a_{2\mathrm{D}}^{(\mathrm{pbc})} = L\, \exp\left\{-\frac{1}{2}\,\frac{L}{a_{3\mathrm{D}}}\right\},$$

for our setup with periodic boundary conditions.

We find that a reduction of the dimensionless confinement length parameter $L\sqrt{\mu_{\mathrm{mb}}}$ leads to an increased density and thereby to an increased Fermi energy $\varepsilon_F = k_F^2$. As a consequence the equation of state $(\mu - \varepsilon_B/2)/\varepsilon_F$, presented in Figs. 5.4 and 5.5, is lowered for more confined systems.

Here the Fermi momentum is calculated using the three-dimensional definition $k_F = (3\,\pi^2\, n)^{1/3}$ as the initial conditions for the RG flows, i.e. also for the density, are given for a three-dimensional system. Therefore, the Fermi momentum k_F of the (quasi-) two-dimensional system is calculated by using the functional form given in the ultraviolet. The reduced dimension then enters via the flow of the density.

Comparing the results in Fig. 5.4 with the experimental data found in [63] for a (quasi-) two-dimensional setup we find a qualitatively good agreement. Especially on the BEC-

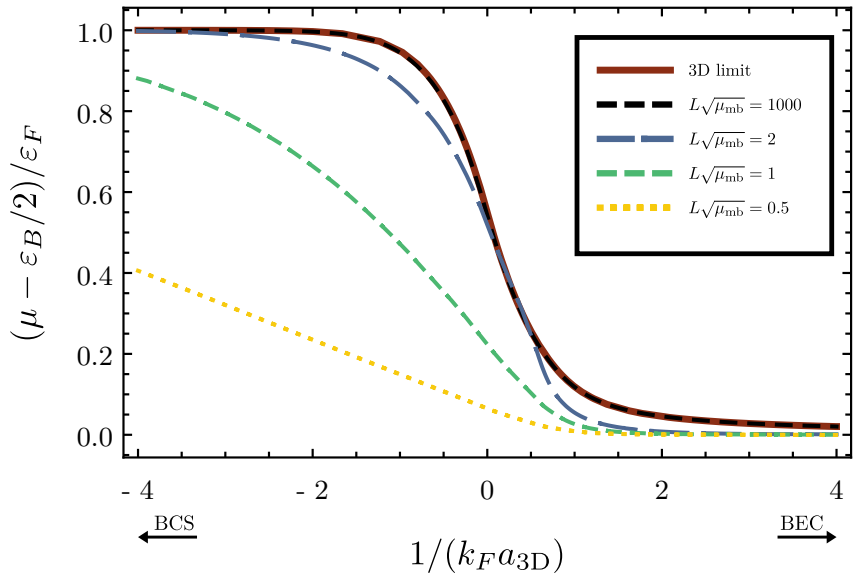

Figure 5.4: Comparison of the equation of state at zero temperature for different confinement length scales and the three dimensional case with respect to the 3D crossover parameter $1/(k_F\, a_{3D})$ for $t_{\text{final}} = -17$. From top to bottom: 3D limit in solid-red (solid-grey), $L\sqrt{\mu_{mb}} = 1000$ in dashed-black, $L\sqrt{\mu_{mb}} = 2$ in long-dashed-blue (long-dashed line in dark grey), $L\sqrt{\mu_{mb}} = 1$ in dashed-green (dashed line in grey), $L\sqrt{\mu_{mb}} = 0.5$ in dotted-yellow (dotted line in light grey). The three-dimensional case is recovered for large $L\sqrt{\mu_{mb}}$.

side, where the measurements were obtained in the superfluid phase, the equation of state for lower values of the confinement length $L\sqrt{\mu_{mb}}$ yields the correct behaviour. However, on the BCS-side the equation of state for confinements $L\sqrt{\mu_{mb}} \lesssim 6$ does not give the quantitative correct result. This behaviour might be on the one hand attributed to an insufficient precision in the determination of the density. For a more elaborate way to obtain the density, see Chapter 7. On the other hand, as mentioned in Section 5.1, the two-dimensional limit for periodic boundary conditions may feature parameters which do not coincide with the ones in three dimensions.

In Fig. 5.6 we compare the gap parameter $\Delta = (h^2\,\rho_0)^{1/2}$ with respect to the Fermi energy ε_F for different confinement length scales. One finds a flattening of the curve for lower dimensionality, while the three-dimensional case is recovered for large length scales $L\sqrt{\mu_{mb}}$. Interestingly, the gap saturates much faster for small length scales, already around $L\sqrt{\mu_{mb}} \simeq 0.5$, representing the two-dimensional limit. Moreover, depending on the (three-dimensional) scattering length a_{3D}, regions of an increased gap Δ/ε_F can be found at intermediate length scales within the dimensional crossover. This dip-like structure is a characteristic property of the modes and is related to the specific boundary conditions and. It is also found at finite temperature.

Note that due to the renormalisation of the fields, the expectation value $\Delta = (h^2\,\rho)^{1/2}$

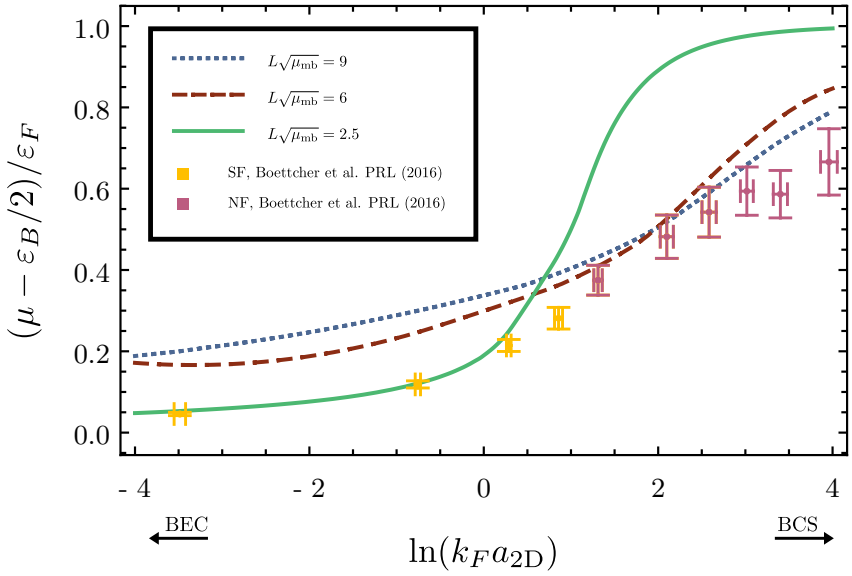

Figure 5.5: Comparison of the equation of state for different confinement length scales to the experimental data from [63] with respect to the 2D crossover parameter $\ln(k_F\, a_{2D})$ for $t_{\rm final} = -17$. Here we show: $L\sqrt{\mu_{\rm mb}} = 9$ in dotted-blue (dotted line in grey), $L\sqrt{\mu_{\rm mb}} = 6$ in dashed-red (dashed line in dark grey), $L\sqrt{\mu_{\rm mb}} = 2.5$ in solid-green (solid line in light grey). The experimental data is obtained for the lowest attainable temperatures of $T/T_F \approx 0.05$ on the BEC-side and $T/T_F \approx 0.1$ on the BCS-side. The orange and purple (light grey and dark grey) squares denote measurements in the superfluid and normal phase.

can be non-zero, even in the two-dimensional limit [117], where the Mermin-Wagner theorem [110, 111] forbids true long-range order. Instead, algebraically decaying correlation functions with a non-vanishing superfluid density can be found [152–155].

5.6 Superfluid transition

5.6.1 Dimensional crossover of the critical temperature

At finite temperature we study in the following the behaviour of the critical temperature T_c/T_F with respect to the spatial extension in transversal z-direction $L\sqrt{\mu_{\rm mb}}$. The Fermi temperature $T_F = {k_F}^2$ is, as in the zero temperature case, calculated using the three-dimensional relation between the Fermi momentum and the density $k_F = (3\,\pi^2\,n)^{1/3}$. The order parameter for the superfluid transition is the (finite-temperature) gap $\Delta = (h^2\,\rho)^{1/2}$ in the fermion spectrum. The critical temperature is calculated as the largest temperature at which the gap Δ is non-vanishing, as described in Section 5.3.

As shown exemplary for $a_{3D}^{-1} = 0$ in Fig. 5.7, one can identify a dimensional crossover from three to two dimensions for all values of the three-dimensional scattering length. The

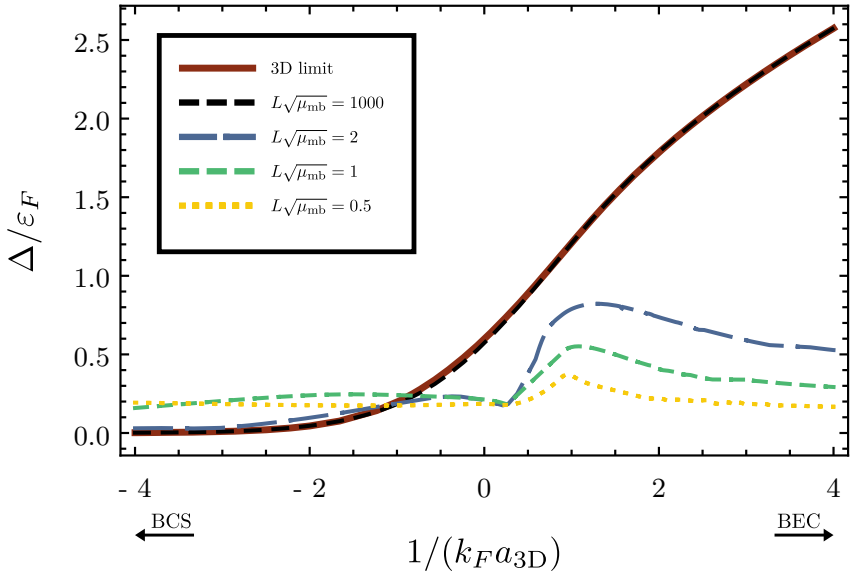

Figure 5.6: Comparison of the gap parameter for different confinement length scales and the three dimensional case with respect to the 3D crossover parameter $1/(k_F\, a_{\rm 3D})$ for $t_{\rm final} = -17$. From top to bottom (on BEC-side): 3D limit in solid-red (solid line in grey), $L\sqrt{\mu_{\rm mb}} = 1000$ in dashed-black, $L\sqrt{\mu_{\rm mb}} = 2$ in long-dashed-blue (long-dashed line in dark grey), $L\sqrt{\mu_{\rm mb}} = 1$ in dashed-green (dashed line in grey), $L\sqrt{\mu_{\rm mb}} = 0.5$ in dotted-yellow (dotted line in light grey). The three-dimensional case is recovered for large $L\sqrt{\mu_{\rm mb}}$.

limiting case of three dimensions is reached for large confinement scales $L\sqrt{\mu_{\rm mb}}$. Moreover, a two-dimensional limit is obtained where the critical temperature in units of the Fermi temperature saturates and is significantly reduced with respect to the three-dimensional case. Note that as in the zero temperature case 5.5 we choose $t_{\rm final} = -17$ for the final RG-flow scale.

Furthermore, one can clearly discern dips in the dimensional crossover of the critical temperature where we find an increased T_c/T_F at intermediate stages between the two- and three-dimensional limit. Interestingly, their appearance and amplitude seem to be related to the scattering length $a_{\rm 3D}$ chosen in the ultraviolet. Moreover, we find a larger amplitude for more confined systems. The occurrence of the dips can be explained by the mode structure of a confined system specified by the chosen boundary conditions. As a consequence of the respective mode structure, the density of states for a confined system has a step-like structure. The dips can be found at the positions of these discontinuities, while the dip structure for the critical temperature T_c/T_F emerges at the same confinement length scales $L\sqrt{\mu_{\rm mb}}$ as for the zero temperature gap parameter Δ. In a mean-field analysis with a confinement in transversal z-direction induced by a harmonic potential on the weakly-interacting BCS-side of the BCS-BEC crossover a similar dip-like structure of the critical temperature was found [123]. The same behaviour is seen in confined superconductors

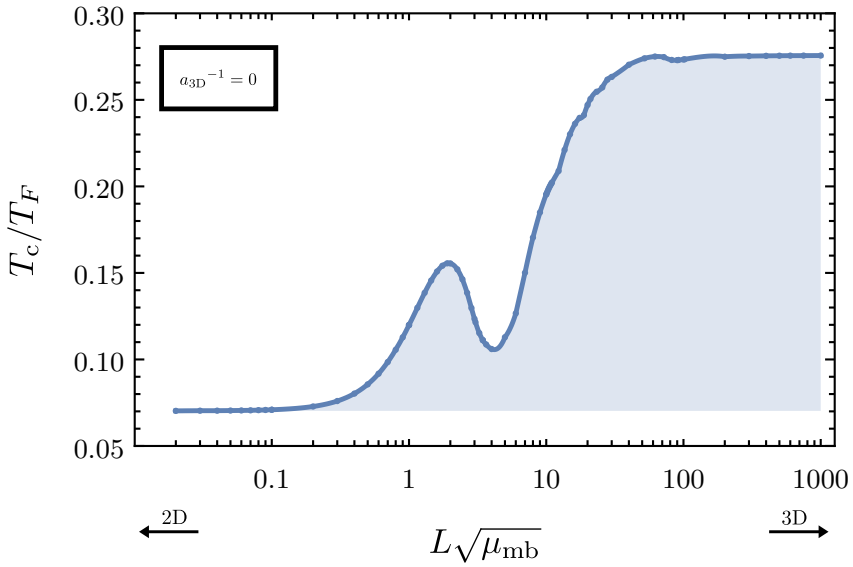

Figure 5.7: Critical temperature T_c/T_F as a function of the confinement length scale $L\sqrt{\mu_{mb}}$ at an exemplary three dimensional fermion scattering length of $a_{3D}^{-1} = 0$ for $t_{final} = -17$. Similar plots can be found for different scattering lengths with the difference being the amplitude and the position of the dips. This non-monotonous behaviour results from the mode structure caused by the chosen boundary conditions and are related to the step-like structure of the density of states for a confined system. Similar dips were also found in a mean-field analysis with a harmonic confinement [123].

or thin superconducting films where the critical temperature, the gap parameter and the intrapair correlation lengths are increased at so-called shape resonances [144–150].

5.6.2 Finite temperature phase diagram

In Figs. 5.8 and 5.9 the critical temperature T_c/T_F is shown as a function of the three dimensional inverse concentration $c^{-1} = (k_F\, a_{3D})^{-1}$ and the two-dimensional crossover parameter $\ln(k_F\, a_{2D})$ for different confinement length scales over the whole BCS-BEC crossover. The phase diagram in Fig. 5.8 approaches the three-dimensional limit for large confinement length scales, while the critical temperature is reduced for lower dimensionality over the BCS-BEC crossover. On the other hand, we find an increased critical temperature on the BCS-side of the crossover around $L\sqrt{\mu_{mb}} = (0.5 \ldots 5)$. On the BEC-side T_c/T_F continues to be reduced for more confined systems.

In Figs. 5.9 and 5.10 we find the expected exponential decrease on the BCS-side of the crossover, where $\ln(k_F\, a_{2D}) \gg 1$, for small confinement scales in a quasi-two-dimensional

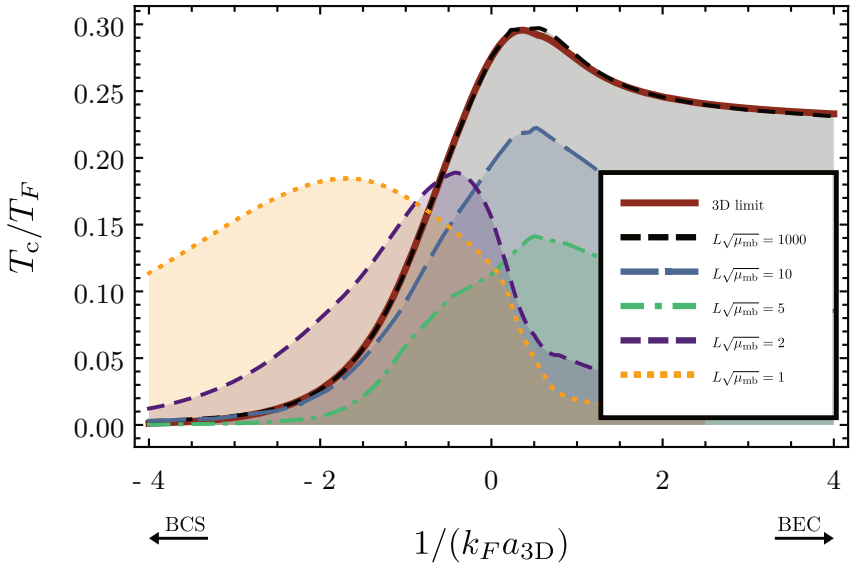

Figure 5.8: Phase diagram in terms of T_c/T_F for different confinement length scales and the three dimensional case with respect to the 3D crossover parameter $1/(k_F\, a_{3D})$ for $t_{final} = -17$. From top to bottom (on BEC-side): 3D limit in solid-red (solid line in grey), $L\,\sqrt{\mu_{mb}} = 1000$ in dashed-black, $L\,\sqrt{\mu_{mb}} = 10$ in long-dashed-blue (long-dashed line in grey), $L\,\sqrt{\mu_{mb}} = 5$ in dashed-dotted-green (dashed-dotted line in lighter grey), $L\,\sqrt{\mu_{mb}} = 2$ in dashed-purple (dashed line in dark grey) and $L\,\sqrt{\mu_{mb}} = 1$ in dotted-orange (dotted line in light grey).

geometry. Here it was found [156] that

$$\frac{T_c}{T_F} = \frac{2\,e^{\gamma}}{\pi\, k_F\, a_{2D}}$$

with the Euler number $\gamma \simeq 0.5772$. The critical temperature is lowered by a factor of e when including the Gorkov–Melik-Barkhudarov contribution [157, 158].

Furthermore, the BKT-transition temperature on the BEC-side, where $\ln(k_F\, a_{2D}) \ll 1$, is approximately reached for these length scales. However, for smaller $L\,\sqrt{\mu_{mb}}$, we obtain a smaller value than the predicted BKT transition temperature [107, 158]

$$\frac{T_c}{T_F} = \frac{1}{2}\left[\log\left(\frac{\mathcal{B}}{4\,\pi}\,\log\left(\frac{4\,\pi}{k_F^2\, a_{2D}^2}\right)\right)\right]^{-1},$$

with $\mathcal{B} \simeq 380$.

As described in Section 5.1 this behaviour might be attributed to our choice of boundary conditions. Although we are arriving at a two-dimensional system using periodic boundary conditions, integrating out the higher modes in the transversal z-direction may lead to a shift in the parameters of the Fermi gas. This shift can also be differently pronounced depending on the scattering length. The observation that T_c/T_F decreases towards zero on the BEC-side for $L \to 0$ may be an indication for a strong L-dependence in the map

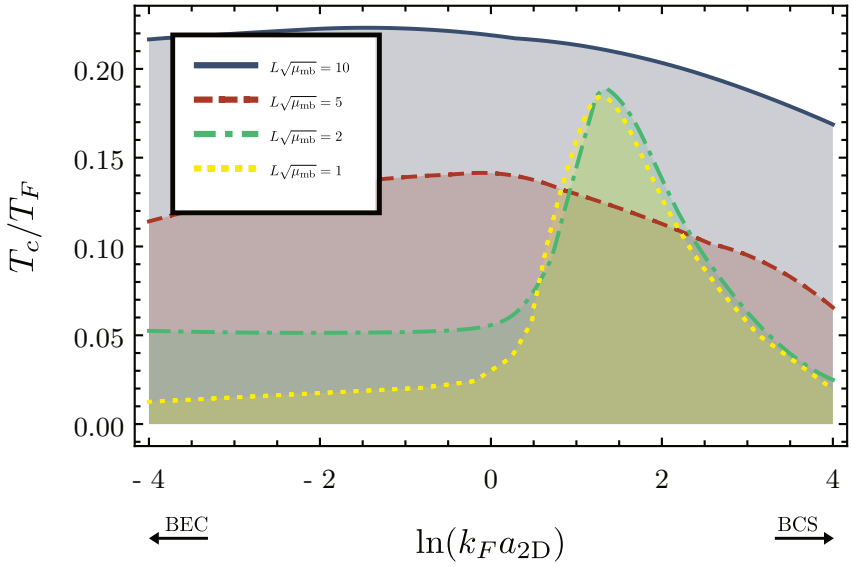

Figure 5.9: Phase diagram in terms of T_c/T_F for different confinement length scales with respect to the 2D crossover parameter $\ln(k_F\, a_{2D})$ for $t_{\rm final} = -17$. From top to bottom (on BEC-side): $L\sqrt{\mu_{\rm mb}} = 10$ in solid-blue (solid line in dark grey), $L\sqrt{\mu_{\rm mb}} = 5$ in dashed-red (dashed line in grey), $L\sqrt{\mu_{\rm mb}} = 2$ in dashed-dotted-green (dashed-dotted line in lighter grey) and $L\sqrt{\mu_{\rm mb}} = 1$ in dotted-yellow (dotted line in light grey). The low critical temperature on the BEC-side is caused by our choice of boundary conditions, see Section 5.1.

from three-dimensional to two-dimensional parameters in this region of the phase diagram and range of L.

In the region of strong correlations, where $\ln(k_F\, a_{2D}) \simeq 1$, we find a substantial increase in the critical temperature T_c/T_F compared to more weakly interacting regions. This increased critical temperature cannot be found in a mean-field analysis by extrapolation of the known BCS- and BEC-limits.

Comparing our results for $L\sqrt{\mu_{\rm mb}} = 3.1$ to the experimental data from [67] in Fig. 5.10, where $L\sqrt{\mu_{\rm mb}}$ is approximately of the order $0.5 \ldots 5$, we find a qualitatively similar phase diagram. Here the increased critical temperature in the strong coupling regime can also be found, yet slightly less pronounced.

In Fig. 5.11 we show our result for a confinement length of $L\sqrt{\mu_{\rm mb}} = 3.1$ and the experimental data on the non-thermal fraction found in [67]. Here the preferred onset of a presuperfluid phase in the strongly correlated region is on par with our result of an increased superfluid temperature. The shift with respect to the two-dimensional crossover parameter can be assigned to the our map of the parameters from a three-dimensional theory to the ones of a effective two-dimensional theory. As described in Sec. 5.1, this possibly induces large changes in parameters like the density or the scattering length and hence the two-dimensional crossover parameter.

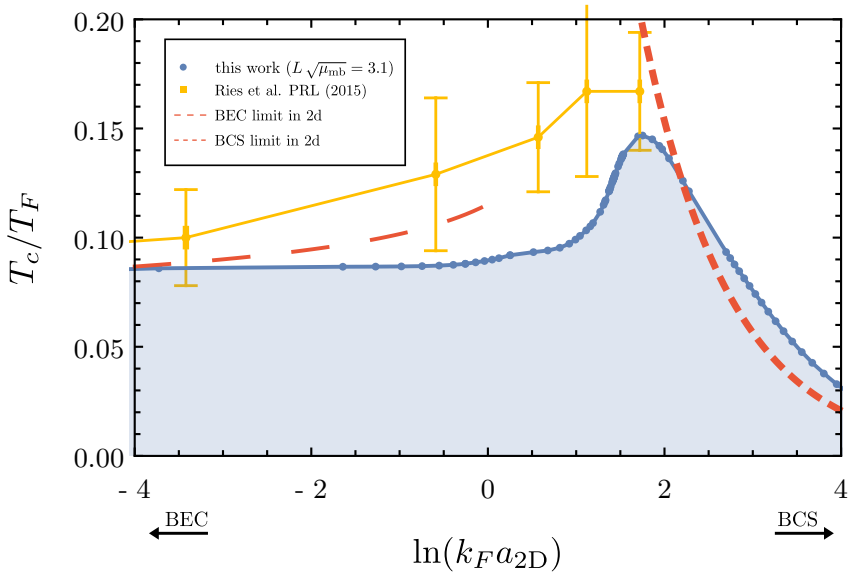

Figure 5.10: Phase diagram in terms of T_c/T_F for a confinement length of $L\sqrt{\mu_{\mathrm{mb}}} = 3.1$ with respect to $\ln(k_F\, a_{2\mathrm{D}})$ for $t_{\mathrm{final}} = -17$. Here we show the experimental data from [67] with the corresponding statistical errors in orange (light grey), as well as both the perturbative BKT- and BCS-transition temperatures as dashed red (dashed grey) lines in the appropriate regimes, i.e. $\ln(k_F\, a_{2\mathrm{D}}) \ll -1$ (BEC) and $\ln(k_F\, a_{2\mathrm{D}}) \gg 1$ (BCS).

We note, that a comparison to the experimental data in [67], as shown in Fig. 5.10 and 5.11, is not straightforward. Due to different parameters used and a varying transverse confinement (w.r.t. the three-dimensional scattering length) in the experimental setup, there is no one-to-one map between the two descriptions of the (quasi-) two-dimensional system. For a better comparison it would be beneficial to specify the confinement length L in terms of the Fermi momentum k_F. This, however, necessitates a quantitatively improved determination of the density in our calculations, as we will show in further detail in Chapter 7. In the end, comparing theoretical and experimental data on equal footing, would allow to gain further insight in the dimensionality effects of ultracold Fermi gases.

5.7 Conclusion and outlook

We have studied the dimensional crossover in an ultracold Fermi gas from three to two dimensions, thus extending the work on non-relativistic bosons carried out in [117], as well as the mean-field analysis in [123] for fermions. Particular emphasis was put on the superfluid phase transition calculated over the whole BCS-BEC crossover in dependence on different confinement length scales. A comparison to recent experiments in [63] and [67] shows a qualitative good agreement. Moreover, we find a non-trivial behaviour of the finite temperature phase diagram when confining the Fermi gas in reduced dimensionality.

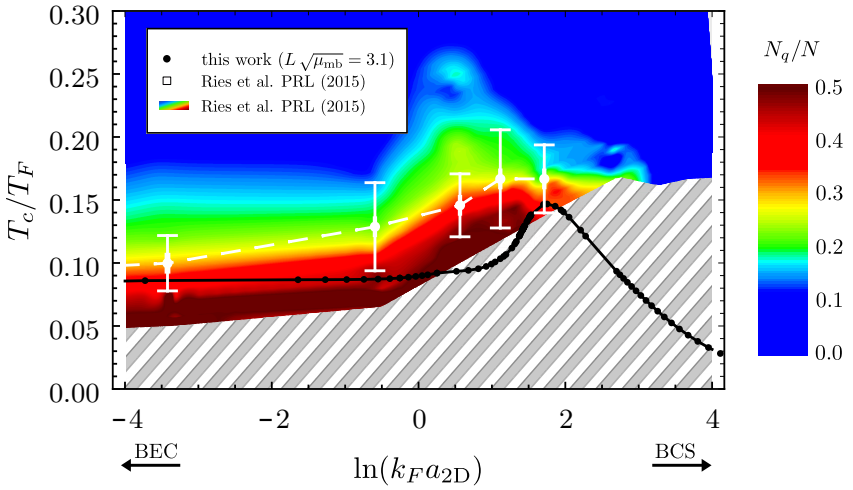

Figure 5.11: Phase diagram in terms of T_c/T_F for a confinement length of $L\sqrt{\mu_{\rm mb}} = 3.1$ (in black) with respect to $\ln(k_F\, a_{2D})$. Here we show the experimental data from [67]. The experimental critical temperature T_c/T_F with the corresponding statistical errors is depicted in white, while the colour scale denotes the non-thermal fraction which signals the onset of a presuperfluid phase.

Here, on the one hand, for small confinement length scales a substantial reduction of the critical temperature T_c/T_F is found on the BEC-side of the crossover, while, on the other hand, the critical temperature on the BCS-side is moderately increased. Notably, in the strongly-coupled regime a substantially higher critical temperature is found which is on par with recent measurements [67].

Within the dimensional crossover from three to two dimensions a dip-like structure with regions of increased and reduced critical temperature T_c/T_F were observed. This dip-like structure is more or less pronounced depending on the scattering length chosen in the ultraviolet a_{3D}. Its exact shape is an artefact of the boundary conditions chosen for the confinement. For a harmonic confinement similar dips were seen in [123] for a mean-field study of the critical temperature on the BCS-side for quasi-two dimensional Fermi gases. Moreover, in confined superconducting systems this behaviour is known as superconducting shape resonances and responsible for an increased critical temperature, gap and intrapair correlation length at the discontinuities of the density of states.

These results suggest that a geometry lying between three and two dimensions might be beneficial in finding systems with increased critical temperature and hence in advancing in the quest for high-T_c superconductors.

Overall, we see that certain effects can be attributed to the dimensionality of the system. These include the dip-like structure of increased and reduced critical temperature within the dimensional crossover and the overall shape of the phase diagram at a certain

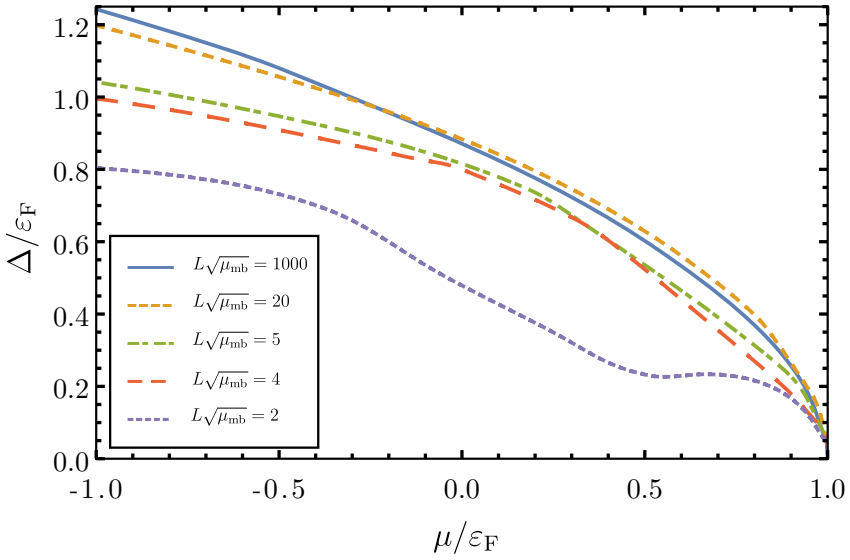

Figure 5.12: Comparison of the zero temperature gap Δ/ε_F with respect to the normalised chemical potential μ/ε_F for different confinement length scales. For large $L\sqrt{\mu_{\mathrm{mb}}} = 1000$ (in blue) we agree well with recent experimental results [160]. For smaller confinement length scales, though being qualitatively of the same shape (except for the strongest confinement $L\sqrt{\mu_{\mathrm{mb}}} = 2$ shown here), we find a decrease in Δ/ε_F.

confinement length $L\sqrt{\mu_{\mathrm{mb}}}$. The effective dimension of the system has thus a constraining impact on the many-body physics.

The above procedure of confinement from three to two dimensions can in general be extended to confinements from three to one and from two to one dimensions, cf. e.g. [159] for studies of a dimensional crossover from two to one dimensions. Moreover, for a more realistic confinement scenario a harmonic trapping potential $V(z) = \frac{1}{2} m\,\omega_z\,z^2$, as it is approximately realised in most ultracold atom experiments, should be implemented instead of the periodic conditions used in this work in order to account for the correct trapping geometry. However, already the periodic boundary conditions yield qualitatively similar features in the L-dependence of the critical temperature as a harmonic trap.

A further quantitative improvement within the dimensional crossover as well as in three dimensions concerns the calculation of the density by which every quantity is normalised, namely by means of the Fermi momentum k_F. As we detail in Chapter 7, the initial conditions for observables g_i with scaling dimension $d_{g_i} \geq 2$ are dependent on the chemical potential μ. As a consequence, the flow of the density, calculated by a μ-derivative of the effective potential, is not UV-finite. In Chapter 7 we define an iterative safe way to calculate the density and present quantitative results for the three-dimensional BCS-BEC crossover. The case of the dimensional crossover will be future work. In addition, the truncation may be extended to include also the renormalisation of the fermion propagator,

as well as higher orders in the derivative expansion.

Another interesting aspect is the study of spin- and mass-imbalanced Fermi gases within the dimensional crossover since here the influence of mismatching Fermi surfaces and stronger fluctuations in lower dimensions might result in competing effects concerning pairing [90–95]. This may shed further physical insights, for example in the search for high temperature superconductors.

In addition, new experimental results measured in [160] indicate that the superfluid gaps Δ/ε_F versus the normalised chemical potential μ/ε_F obtained in a three- and two-dimensional system collapse onto a single curve. This is a very interesting property, as it points to a unified description of the BCS-BEC crossover independent of the dimensionality. A first analysis of our zero temperature data for the gap Δ/ε_F in Fig. 5.12 finds qualitative agreement for weak confinement, i.e. in a more 3D-like system. For stronger confinement, though being of the same qualitative shape (except for $L\sqrt{\mu_{\mathrm{mb}}} = 2$), the gap normalised over the Fermi energy ε_F is lowered. This discrepancy may well be attributed to a shift in parameters, like the density, for our choice of boundary conditions, as well as the insufficient quantitative precision in the density determination here. Further investigation of this behaviour might lead to a deeper understanding of the underlying many-body physics.

Already at the present stage our beyond-mean-field analysis is an advancement in the study of the interplay between many-body physics and dimensionality of ultracold Fermi gases. It reveals that the dependence of fluctuation effects on the effective dimensionality leads to new characteristic features that can be exploited in experiment and serve as a test for theoretical methods.

CHAPTER 6

Spectral functions

This Chapter is in parts based on Ref. [2].

We investigate observables obtained in Euclidean space-time in Chapter 5 and Chapter 7. In principle, the full knowledge of imaginary-time Euclidean correlation functions constitutes the solution of the underlying theory. However, in practice this is complicated in so far that one usually knows only a finite number of correlation functions and in most cases only on a numerical level. As we have seen, one can nevertheless compute Euclidean observables, i.e. static, thermodynamic quantities, such as e.g. the density or the superfluid gap in ultracold atom systems.

Ultimately, however, we are also interested in acquiring dynamical information of the theory. In particular, this includes knowledge of transport coefficients, such as conductivities, viscosities or diffusion coefficients. They characterise fluctuations on long time and length scales in systems close to thermal equilibrium and their real-time relaxation. Transport coefficients consequently describe inherently real-time physics.

A central quantity for determining transport coefficients are real-time spectral functions, where Kubo relations are used to extract the transport coefficients. Moreover, spectral functions are relevant quantities of their own right since they for example encode (quasi-) particle spectra, as well as collective excitations, cf. e.g. [33].

To obtain this information for our system of an ultracold Fermi gas, we consequently need to extend the Euclidean framework to real time.

The difficulty of applying Euclidean approaches in thermal quantum field theory to real time arises from the necessary analytical continuation. In practice, this can prove to be rather difficult, since the correlation functions in Euclidean space-time are usually only known numerically. Several methods have been successfully applied in order to reconstruct real-time correlation functions from their Euclidean analogues, such as maximum entropy [33, 161–165] or Padé approximant methods [166–169].

From an experimental point of view, radio frequency spectroscopy is performed, see e.g.

[170], in either a spatially [171], or a momentum resolved way [172] to determine the full spectral functions, as outlined e.g. in [173].

In this Chapter we compute (real-time) finite temperature spectral functions for ultracold Fermi gases within the fRG approach. The utilised method is based upon analytically continued frequency components of the flow equations for the two-point functions in the original Euclidean plane, as it has been applied in [174, 175]. Here, we show results for the fermionic spectral functions at a variety of temperatures within the three-dimensional BCS-BEC crossover. Experimental measurements can e.g. found in [171, 176, 177] and for theoretical results for the BCS-BEC crossover we refer e.g. to [33, 178].

We start our discussion by recapping the defining relations of spectral representations and the properties of the accompanying spectral functions in Section 6.1. Laying out our procedure to obtain real-time spectral functions from analytically continued flow equations in Section 6.2 allows us to obtain fermion spectral functions in the symmetry broken regime in Section 6.3. While summarising our results in the end, we also give a short outlook on future directions.

6.1 Spectral representations

The method builds on the existence of a spectral representation and we shall summarise its definitions and the most important properties in this Section. We restrict ourselves to the case of the propagator. From a physics point of view the spectral function of the propagator encodes the spectrum of the theory. It contains information e.g. on (quasi-) particle excitations, masses and decay widths making it a central quantity in understanding the intricate physics of strongly correlated Fermi gases. We follow the formulation in [179, 180] where also generalisations to higher n-point functions can be found.

6.1.1 Källén-Lehmann spectral representation

For a Euclidean field theory the Källén-Lehmann spectral representation of the Euclidean imaginary-time propagator is given by [105, 181–183]

$$G(p_0) = \int_{-\infty}^{\infty} \frac{d\lambda}{2\pi} \frac{\rho(\lambda)}{\mathrm{i}p_0 - \lambda} \,. \tag{6.1}$$

The integrand in Eq. (6.1) can essentially be understood as the free propagator with mass λ which is then integrated with the weight $\rho(\lambda)$, representing the spectral function.

6.1.2 Finite temperature spectral representation

The above expression for the spectral representation, Eq. (6.1), is in general only applicable in vacuum, see e.g. [184]. Here, we recap its generalisation to the finite temperature case

for the propagator, relying on the formulation in [179, 180]. We start by considering the two-point function of a general, i.e. fermionic or bosonic, field χ

$$\gamma_{i_1,i_2}(t_1,t_2) = \langle \chi_1(t_1)\,\chi_2(t_2)\rangle \ ,$$

with t_i ordered in the imaginary part of the analytically continued time. This enables us to perform the Fourier transform

$$\gamma_{i_1,i_2}(t_1,t_2) = \left(\prod_{j=1}^{2}\int_{-\infty}^{\infty}\frac{d\omega_j}{2\pi}\,e^{-\mathrm{i}\,\omega_j\,t_j}\right)\,\gamma_{i_1,i_2}(\omega_1,\omega_2)\,. \tag{6.2}$$

In equilibrium, we can reduce the number of arguments by using translational invariance

$$\gamma_{i_1,i_2}(\omega_1,\omega_2) = 2\pi\,\delta(\omega_1+\omega_2)\,\gamma_{i_1,i_2}(\omega_1)\,. \tag{6.3}$$

The thermal correlation functions have to fulfil the so-called Kubo-Martin-Schwinger (KMS) condition, to wit

$$f_{\omega_{i_1}}\,\gamma_{i_1,i_2}(\omega_1,\omega_2) = \gamma_{i_2,i_1}(\omega_2,\omega_1)\,, \tag{6.4}$$

with $f_\omega = e^{-\beta\omega}$. In the end, we are interested in imaginary-time correlation functions

$$\gamma_{i_1,i_2}(\mathrm{i}(p_1)_0,\mathrm{i}(p_2)_0) = \left(\prod_{j=1}^{2}\int_0^\beta d\tau_j\,e^{-(p_j)_0\,\tau_j}\right)\,\langle\mathcal{T}\,\chi_{i_1}(-\mathrm{i}\tau_1)\chi_{i_2}(-\mathrm{i}\tau_2=0)\rangle\ . \tag{6.5}$$

Here, the zero component of the Euclidean momenta p_i is represented by $(p_i)_0$ and $\mathcal{T}$ is the time ordering operator. We can now define finite temperature spectral representations by plugging Eq. (6.2) into Eq. (6.5) using Eq. (6.3).

For the Euclidean propagator we then explicitly find

$$G(p_0) = \int_{-\infty}^{\infty}\frac{d\lambda}{2\pi}\int_0^\beta d\tau\,e^{\mathrm{i}\,p_0\,\tau}\,e^{-\lambda\,\tau}\,\gamma_{12}(\lambda)\,,$$

where the τ-integration can easily be performed, yielding

$$G(p_0) = \int_{-\infty}^{\infty}\frac{d\lambda}{2\pi}\,\frac{1}{\lambda-\mathrm{i}p_0}\left(1-e^{-\beta\lambda+\mathrm{i}\beta p_0}\right)\,\gamma_{12}(\lambda)\,.$$

We now use the KMS condition Eq. (6.4) to remove $f_\lambda = e^{-\beta\lambda}$ and exploit the fact that the zero component of the Euclidean momenta p_0 is restricted to discrete Matsubara modes. The phase factor thus yields $e^{\mathrm{i}\beta p_0} = \zeta$, with $\zeta = 1$ ($\zeta = -1$) for bosons (fermions). We obtain the desired Källén-Lehmann spectral representation (with an overall minus sign) at finite temperature

$$G(p_0) = \int_{-\infty}^{\infty}\frac{d\lambda}{2\pi}\,\frac{\rho(\lambda)}{\mathrm{i}p_0-\lambda}\,. \tag{6.6}$$

Here we defined the spectral function as

$$\rho(\omega) = \Big[\chi_1(\omega), \chi_2(-\omega)\Big]_\zeta \,. \tag{6.7}$$

The graded commutator $[\,\cdot\,,\,\cdot\,]_\zeta$ in Eq. (6.7) relates to the commutator for bosons and to the anti-commutator for fermions, respectively. Starting from the spectral representation in Eq. (6.6) we can now define the retarded and advanced propagators of the Euclidean propagator analytically continued to the whole p_0-plane, to wit

$$\begin{aligned} G_{\mathrm{R}}(\omega) &= \lim_{\epsilon\to 0^+} G\left(-\mathrm{i}(\omega + \mathrm{i}\epsilon)\right) \,, \\ G_{\mathrm{A}}(\omega) &= \lim_{\epsilon\to 0^+} G\left(-\mathrm{i}(\omega - \mathrm{i}\epsilon)\right) \,. \end{aligned} \tag{6.8}$$

From this one easily finds the usual property $[G_{\mathrm{R}}(\omega)]^* = G_{\mathrm{A}}(\omega)$ where $(\,\cdot\,)^*$ denotes the complex conjugation. From Eq. (6.8) also immediately follows the expression for the spectral function $\rho(\omega)$ in terms of the real-time retarded and advanced propagators

$$\rho(\omega) = G_{\mathrm{R}}(\omega) - G_{\mathrm{A}}(\omega) = 2\,\mathrm{Im}\,G_{\mathrm{R}}(\omega) = 2\,\mathrm{Im}\left[\lim_{\epsilon\to 0^+} G\big(-\mathrm{i}(\omega + \mathrm{i}\epsilon)\big)\right] . \tag{6.9}$$

Using the relation between the (scale dependent) propagator and the second functional derivative of the effective average action in Eq. (3.9) we can express the spectral function in Eq. (6.9) in terms of the retarded two-point function $\Gamma^{(2)}_{\mathrm{R}}(\omega)$

$$\rho(\omega) = \frac{2\,\mathrm{Im}\,\Gamma^{(2)}_{\mathrm{R}}(\omega)}{\Big(\mathrm{Re}\,\Gamma^{(2)}_{\mathrm{R}}(\omega)\Big)^2 + \Big(\mathrm{Im}\,\Gamma^{(2)}_{\mathrm{R}}(\omega)\Big)^2} \,, \tag{6.10}$$

with $\Gamma^{(2)}_{\mathrm{R}}$ being the retarded two-point function at the macroscopic scale $k = 0$. Eq. (6.10) will be the equation we use in order to calculate the real-time spectral function. Note, that the propagators and likewise the spectral function in general depend also on spatial momenta which we have suppressed in our notation.

Spectral functions as defined in Eq. (6.6) have a number of essential properties. By using the symmetry properties of the retarded and advanced propagators

$$\begin{aligned} G_{\mathrm{R}}(\omega, \vec{p}) &= G_{\mathrm{R}}(\omega, -\vec{p}) \,, \\ G_{\mathrm{R}}(-\omega, \vec{p}) &= G_{\mathrm{A}}(\omega, \vec{p}) \,, \end{aligned}$$

it is easily found that the spectral functions obey the following symmetry relations

$$\begin{aligned} \rho(\omega, -\vec{p}) &= \rho(\omega, \vec{p}) \\ \rho(-\omega, \vec{p}) &= -\rho(\omega, \vec{p}) \,, \\ \rho(-\omega, -\vec{p}) &= -\rho(\omega, \vec{p}) \,. \end{aligned}$$

Moreover, one can show that for physical states the spectral function follows the sum rule, [105, 183]

$$\int_{-\infty}^{\infty} \frac{d\omega}{2\pi}\, \rho(\omega) = 1\,.$$

Finally, the spectral function also obeys the positivity constraint for physical particles

$$\mathrm{sgn}(\omega)\, \rho(\omega) \geq 0\,.$$

6.1.3 Example of free fermion propagator

A concrete example for the spectral representation is computed for a free field. For free non-relativistic fermions the Euclidean imaginary-time propagator is given by

$$G(\omega) = \frac{1}{\mathrm{i}\omega_n + p^2 - \mu}\,.$$

Applying Eq. (6.9) we immediately obtain for the spectral function

$$\rho(\omega, \vec{p}) = \delta(\omega - \varepsilon_{\vec{p}} + \mu)\,,$$

where we have used

$$\frac{1}{\omega \pm \mathrm{i}0^+} = \mathcal{P}\frac{1}{\omega} \mp \mathrm{i}\,\pi\,\delta(\omega)\,,$$

with $\mathcal{P}$ denoting the Cauchy principal value.

6.2 Analytical continuation of flow equations

Our general viewpoint is that our quantum field theory, specifically its scale dependent effective action $\Gamma_k[\phi]$, is defined within the Matsubara formalism. Here, the fermionic finite temperature correlation functions are anti-periodic in imaginary time with circumference $1/T$, cf. Section 3.3. In the following, we want to compute real-time properties from the fRG by analytical continuation. One option is to solve the flow equations (using the Matsubara formalism) for imaginary frequencies in Euclidean space-time and then to analytically continue the result at the macroscopic scale $k = 0$ to real frequencies, e.g. by using Padé or maximum entropy techniques. This approach generally needs a sufficient amount of numerical information on the (imaginary) frequency dependence of the propagator, and thus is numerically usually more involved. Other reconstruction methods can, e.g. be found in [185] for an approach exploiting analytical properties or in [186] using Deep Neural Networks. Furthermore, for Dyson-Schwinger calculations see [187, 188].

Here, we use the approach laid out in [174, 175] and perform the analytical continuation to real frequencies already on the level of the flow equations. As outlined in [174] this procedure has a number of advantages, to wit

- Provided the flow equations are known analytically the analytical continuation can be performed symbolically without using more involved numerical methods.
- Information about real-time properties can be used on the right hand side of the flow equations in a self-consistent way, thus allowing for an improved truncation and performance.
- It is able to respect space-time and translational symmetries and at the same time, it allows for an analytical computation of Matsubara sums given a convenient choice of the regulator function.
- This approach is easier to compute than closed time contour methods. Furthermore, as it is based on the Euclidean formalism, the knowledge can be carried over.

Note, that only close-to-equilibrium observables that are accessible via linear response theory can be calculated in this way [174] and more complicated non-linear response observables in far-from-equilibrium situations have to be obtained in different ways, e.g. Schwinger-Keldysh or temporal fRG methods, cf. e.g. [189–192].

In general analytical continuation describes the process of extending the domain of definition of an analytical function (typically only defined on a certain number of discrete points) to the whole complex plane. One is specifically interested in its definition on the real axis in order to obtain real-time observables, cf. Fig. 6.1. The analytically continued function $F(z)$ has to coincide with its original form at its former domain of definition $\mathrm{i}\omega_n$,

$$F(z)|_{z=\mathrm{i}\,\omega_n} = f(\mathrm{i}\omega_n)\,.$$

This procedure is in general not unique and there exist infinitely many ways to define an analytical continuation (even when based on infinitely many discrete points). For this reason, in order to restrict the amount of possibilities and to arrive at a physical solution, appropriate boundary conditions have to be applied, cf. Baym-Mermin boundary conditions [193]. This requires the analytically continued function $F(z)$ to be analytical off the real axis and to be bounded as $|z| \to \infty$.

6.2.1 Analytical continuation of two-point functions

In order to analytically continue the flow equations for the two-point functions defined in Section 4.1, specifically in Eq. (4.16), we exploit the fact that the flow equations of both fermionic, as well as bosonic two-point functions are of a one-loop structure, as shown in Fig. 4.2. By using three-dimensional Litim-type regulators, cf. Eq. (4.19), the frequency component of the four-momentum is unaffected. Thus, we are able to analytically calculate the fermionic and bosonic Matsubara sums and express them in terms of occupation numbers.

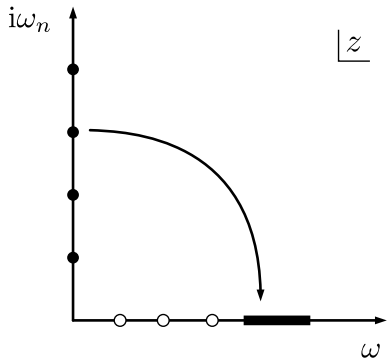

Figure 6.1: Graphical depiction of the analytical continuation of a function defined at discrete points $\mathrm{i}\omega_n$ in the complex plane z to the real axis.

We can utilise the cyclicity of the fermionic and bosonic occupation numbers with respect to the Euclidean frequency $p_0 = 2n\pi T$,

$$n_{F,B}(E + \mathrm{i}p_0) = n_{F,B}(E)\,.$$

The analytical continuation is then performed in the following way

$$\partial_t \Gamma_k^{(2),\mathrm{R}}(\omega, \vec{p}) = -\lim_{\epsilon \to 0} \partial_t \Gamma_k^{(2),\mathrm{E}}(p_0 = -\mathrm{i}(\omega + \mathrm{i}\epsilon), \vec{p})\,, \tag{6.11}$$

with ϵ being a small, real parameter in the numerical implementation.

Our procedure for the calculation of spectral functions is as follows:

1. Calculate the flow of the couplings at vanishing external momentum and frequency $P = 0$ in Euclidean space.

2. Analytically continue the two-point functions $\Gamma_k^{(2),\mathrm{E}}(p_0, \vec{p} = 0)$ to real frequencies according to Eq. (6.11).

3. Solve the flow of the real-time two-point functions with the solution of the couplings from step 1.

4. Calculate the spectral function according to Eq. (6.10).

In summary, we evaluate the Matsubara sums analytically, thereby taking care of the mixed diagrams, as in Fig. 4.2, by shifting the Matsubara frequencies appropriately. For further details on our case, we refer to Appendix C.

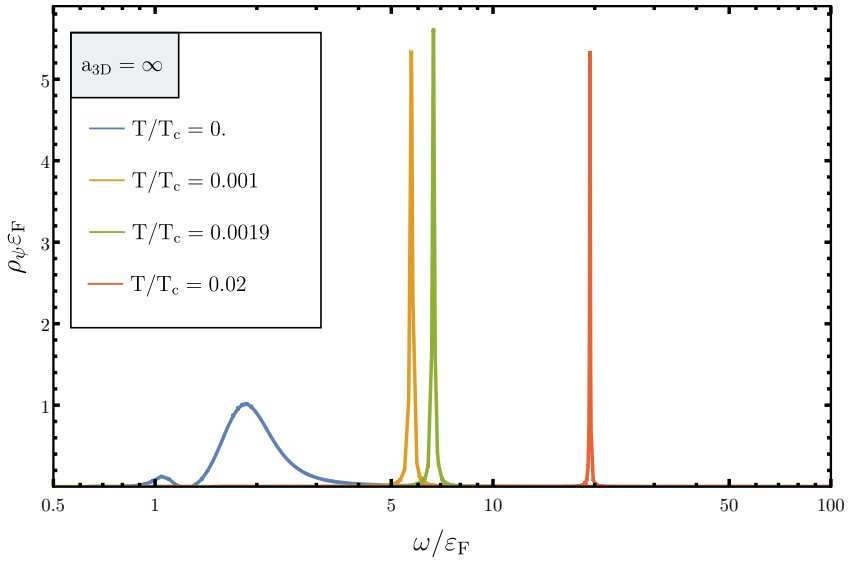

Figure 6.2: The normalised fermion spectral function $\rho_\psi\, \varepsilon_F$ in terms of the frequency ω/ε_F at unitarity, i.e. $a_{3D} = \infty$, for a variety of temperatures. In blue we show the zero-temperature case $T = 0$, while the yellow curve depicts the case for $T/T_c = 0.001$ and the green curve $T/T_c = 0.0019$. In red we show the case for $T/T_c = 0.02$.

6.3 Fermion spectral functions in the symmetry broken regime

With this at hand, we are in a position for a study of spectral functions at finite temperature within the BCS-BEC crossover. We concentrate on the fermionic spectral functions in three spatial dimensions at vanishing spatial momenta $\vec{p} = 0$ for a range of scattering lengths in the symmetry broken regime. The flow equations of the couplings and the two-point function are solved numerically, as specified in Section 4.7, and the spectral function is obtained via Eq. (6.10) from the corresponding flow of the analytically continued fermionic two-point function. The normalised spectral functions are illustrated in Fig. 6.2 at unitarity, in Fig. 6.3 for $a_{3D} = 5$ on the BEC-side of the crossover, and for $a_{3D} = -5$ on the BCS-side of the crossover in Fig. 6.4.

Across all scattering lengths in the strongly interacting regime we find a rather large broadening of the quasiparticle peaks, especially at the very low temperatures depicted here. This finding is in line with results in [33]. It can be proven in the perturbative BCS- and BEC limits that the existence of well-defined quasi-particles at $T = 0$ is prohibited, cf. [33, 194]. One expects, that the broadened spectral functions transforms into a delta peak with infinite lifetime for zero temperature at the minimum of the dispersion relation.

Furthermore, the position of the peaks are found at larger frequencies ω/ε_F for higher

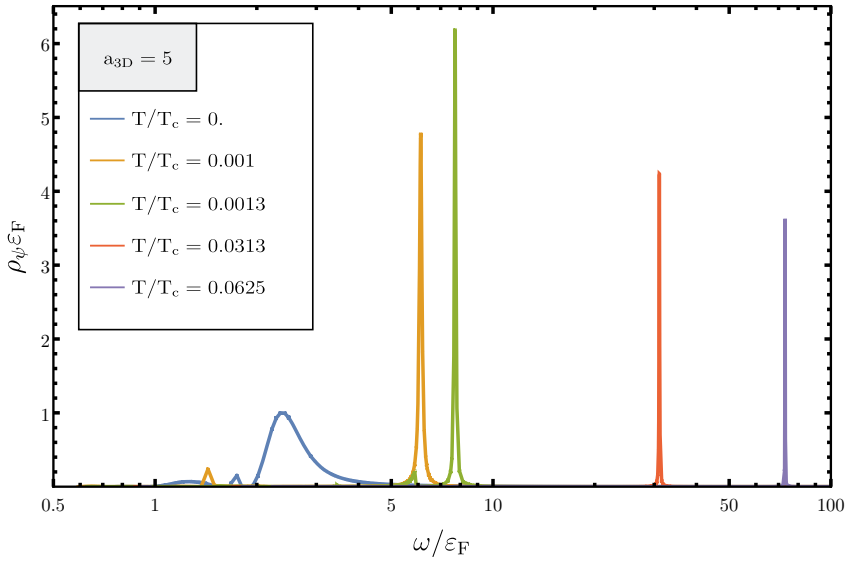

Figure 6.3: The normalised fermion spectral function $\rho_\psi\, \varepsilon_F$ in terms of the frequency ω/ε_F at a scattering length of $a_{3\mathrm{D}} = 5$ for a variety of temperatures. In blue we show the zero-temperature case $T = 0$, while the yellow curve depicts the case for $T/T_c = 0.001$ and the green curve $T/T_c = 0.0013$. The red curve is at $T/T_c = 0.0313$ and the purple curve shows the case for $T/T_c = 0.0625$.

temperatures, while the peak width (with exception of the peak at zero temperature) stays approximately constant, as can be seen in Fig. 6.4. In addition, for small temperatures at unitarity and on the BEC-side of the crossover, the spectral functions show an additional peak at smaller frequencies apart from the dominant peak. These peaks have much smaller spectral weight and vanish for increasing temperatures.

6.4 Conclusion and outlook

The results presented above provide initial findings in the study of the real-time spectral functions for a gas of ultracold fermions at zero and at finite temperature in three dimensions. They cover the strongly interacting regime of the BCS-BEC crossover from a fermionic system $a_{3\mathrm{D}} = -5$, over the unitary regime $a_{3\mathrm{D}} = \infty$ to the case of bosonic dimers $a_{3\mathrm{D}}$ and can in general be further extended to the BCS and BEC limits. We observe a finite width of the spectral functions, even at zero temperature. This is in accordance with the results found in [33, 194]. The expectation of a vanishing width at the dispersion minimum for zero temperature can be checked by computing spectral functions at non-vanishing external momenta. In principle, this can be implemented easily within the

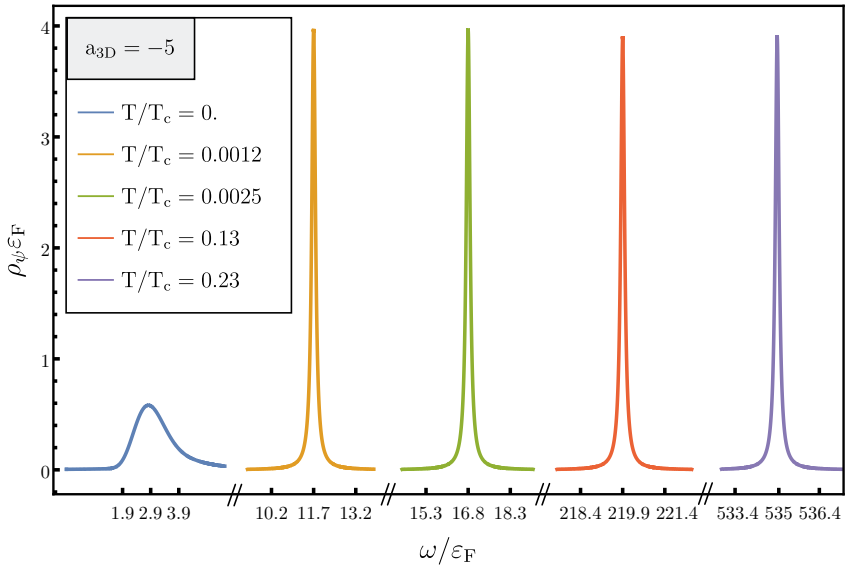

Figure 6.4: The normalised fermion spectral function $\rho_\psi\, \varepsilon_F$ in terms of the frequency ω/ε_F at a scattering length of $a_{3D} = -5$ for a variety of temperatures. In blue we show the zero-temperature case $T = 0$, while the yellow curve depicts the case for $T/T_c = 0.0012$ and the green curve $T/T_c = 0.0025$. The red curve shows the case for $T/T_c = 0.13$ and the purple is at a temperature of $T/T_c = 0.23$. For easier comparison of the individual peaks we break the abscissa.

current approach. The only difference is the slightly more complicated momentum integration. With the knowledge of the momentum dependent spectral function the whole quasiparticle structure can then be mapped out.

Further effort has to be put in understanding the different behaviour concerning the single and double peak structure going from an essentially fermionic to a largely bosonic system. The residual peak for low temperatures at unitarity and for $a_{3D} = 5$ contains a much smaller spectral weight and vanishes for larger temperatures. Here, we need to understand why this feature does not persist when going to higher temperatures.

These observations warrant further examination beyond the temperature range shown here. Going to temperatures above the critical temperatures allows also to gain knowledge on the normal and the pseudogap phase.

Overall with these first steps at vanishing external momentum within the framework of the functional renormalisation group we have shown its applicability in the determination of real-time spectral functions for the BCS-BEC crossover. In the end, the aim is to calculate real-time transport properties from the spectral functions via the corresponding Kubo relations.

CHAPTER 7

Towards quantitative precision

This Chapter is in parts based on Ref. [3].

The quantitative access to the phase structure of ultracold Fermi gases, and in particular the resolution of the equation of state and the change of observables such as the gap through the BEC-BCS crossover has been studied intensively in the past decades. Ultracold Fermi gases show interesting macroscopic quantum phenomena such as superfluidity and, thanks to their amazing tunebility, are also tailor made as model systems for many non-relativistic and relativistic systems such as large density QCD in and out-of-equilibrium and neutron star physics, see e.g. [24].

The system has been investigated with the functional renormalisation group (fRG) approach in the past two decades, and many of its interesting phenomena have been explained within this approach, for respective reviews see e.g. [43, 60]. Given this success, the very good grip on the physics phenomena at work, and quite elaborate approximation schemes used, the failure to access some of the observables such as the equation of state (EoS) as well as the superfluid gap is all the more surprising.

Especially in the unitary limit the determination of the Bertsch parameter, $\xi = \mu/\varepsilon_F|_{a\to\infty}$, has been a long standing problem in cold atomic systems, both for theory as well as in experiment. Its importance has far reaching connections beyond the context of ultracold quantum gases and condensed matter physics, e.g. it was proposed by G.F. Bertsch that the physics of neutron stars can be inferred from it [24]. At unitarity all density derivatives of the energy of the system become universal and are solely determined by their corresponding free Fermi gas quantity and a universal constant, the Bertsch parameter [25, 26]. For example this includes the pressure, the speed of sound or the compressibility. The proportionality factor is the universal Bertsch parameter ξ, to wit

$$E = \xi\, \varepsilon_{FG} = \xi\, \frac{3}{5}\, \frac{\hbar^2}{2\,m}\, k_F^2\,.$$

In this Chapter we show in the context of the fRG approach that the failure to accu-

rately determine the EoS and the superfluid gap does not affect the overall quantitative precision of the fRG approach to ultracold gases. On the contrary the dynamics of these systems is captured very well. The failure is rather related to an insufficient resolution of specific density observables. To that end we put forward a computational approach for the determination of observables at finite density on the basis of their density fluctuations and hyper-fluctuations obtained via derivatives of the density with respect to the chemical potential μ. These μ-derivatives lower the ultraviolet sensitivity of the computed quantities and allow for systematic and quantitative computations of observables via successive integrations with respect to the chemical potential. This scheme has been set-up in the context of low energy QCD in [195], and its universal applicability is shown here.

In the explicit computation we shall utilise the approximation to the full two-component Fermi gas as described in Section 4.1, which however already suffices to access the BEC-side and the unitary limit quantitatively. This also highlights the above statement, that the fRG approach is well-suited for the access to ultracold atomic systems as it captures the respective physics in a uniform manner in the whole crossover regime.

We start by laying out the problem of a dependence of initial conditions on the chemical potential and present a generally valid, iterative safe way to determine related observables such as the density in Section 7.1. The application of this general computational approach to our case of ultracold Fermi gases is discussed in the following Sections. Here, our regulator around the Fermi surface generates the problem of defining ultraviolet finite flows. We show this and a way to overcome this deficiency in Section 7.2. Implementing these additions results in a quantitative determination of the EoS and gap at zero temperature which we present in Section 7.4 before concluding in the end.

7.1 Dependence on the chemical potential μ

In this Section we explain how the method works in general. This entails the discussion of potential μ-dependences of initial conditions, as well as an iterative safe way of how to extract related observables, such as the density and higher μ-derivatives, of the free energy. We refer to [195] for a description of the procedure in the QCD context.

It is well-known that thermal fluctuations decay exponentially with the infrared cutoff scale,

$$f(k/T, R)\, e^{-c(R)k/T}\,, \tag{7.1}$$

where $f(k/T, R)$ rises not more than polynomially or even decays, depending on the (canonical) dimension of the observable under consideration, see [196]. The form of the prefactor as well as the coefficient $c(R)$ depend on the shape of the regulator R. In particular, for non-analytic cutoffs (in frequency) such as the sharp cutoff and the optimal cutoff, cf. e.g. Eq. (4.19), we have $c(R) = 0$ and the thermal behaviour at large cutoff scales relates to the

dimension of the observable. Note that Eq. (7.1) can be shown to hold to any order of a given approximation scheme and hence is a formal, exact property of thermal fluctuations. It is intimately linked to the fact that thermal sums can be represented as contour integrals and the infrared cutoff scale k serves as a mass parameter which shifts poles to momenta $p^2 \propto ik^2$. This also hints at the fact that it is not present for non-analytic regulators, where the Matsubara sum cannot be represented as a contour integral, and a naive dimensional analysis prevails.

In contradistinction, the chemical potential μ as well as other external tuning parameters only lead to a polynomial decay or rise in the dimensionless ratio

$$\hat{k}_{\text{rel.}} = \frac{k}{\mu}\,, \qquad \hat{k}_{\text{non-rel.}} = \frac{k}{\sqrt{\mu}}\,,$$

for the relativistic case and non-relativistic case respectively. In most cases this behaviour is related to the (canonical) dimension of the observable at hand. For example, the free energy or effective action has a vanishing canonical dimension. However, it relates to (negative) pressure p times the space-time volume $\mathcal{V}$ and hence has a scaling dimension $d_p = d$ with the cutoff scales in the relativistic case and scaling dimension $d_p = d + 1$ in the non-relativistic one.

The above arguments entail that the flow of the thermal pressure,

$$\partial_t p(T,\mu) := -\left(\frac{\partial_t \Gamma_k[\phi_{\text{EoS}}, k; T, \mu]}{\mathcal{V}_T} - \frac{\partial_t \Gamma_k[\phi_{\text{EoS}}, k; 0, \mu]}{\mathcal{V}_0}\right),$$

in general decays exponentially for large cutoff scales,

$$\partial_t p(T,\mu) \propto e^{-c(R)k/T}\,,$$

while the free energy density, f, normalised in the vacuum,

$$\partial_t f(T,\mu) := \left(\frac{\partial_t \Gamma_k[\phi_{\text{EoS}}, k; T, \mu]}{\mathcal{V}_T} - \frac{\partial_t \Gamma_k[\phi_{\text{EoS}}, k; 0, 0]}{\mathcal{V}_0}\right),$$

has polynomial growth with k,

$$\partial_t f(T,\mu) \to c_{d_f-2}\, k^{d_f}\, \hat{k}^{-2} + c_{d_f-4}\, k^{d_f}\, \hat{k}^{-4} + k^{d_f}\, O(\hat{k}^{-6})\,, \tag{7.2}$$

given the scaling dimension d_f. Here, vanishing exponents (in the relativistic case) include logarithms.

7.1.1 Initial conditions

From Eq. (7.2) we see that the initial conditions for observables or couplings g_i with scaling dimension $d_{g_i} \geq 2$ are μ-dependent. In turn, for sufficiently large cutoff scales $\hat{k} \gg 1$ the initial conditions for couplings with scaling dimension $d_{g_i} < 2$ do not change when changing the chemical potential.

First we concentrate on the effective action, the flow of which is the master equation in our approach,

$$\partial_t \Gamma_k[\psi, \phi] = \frac{1}{2} \operatorname{Tr} G_{k,\phi}\, \partial_t R_{k,\phi} - \operatorname{Tr} G_{k,\psi}\, \partial_t R_{k,\psi}\,, \tag{7.3}$$

where the field ϕ stands for bosonic fields while ψ stands for fermionic ones. Every observable and coupling can be derived directly from Eq. (7.3) and its solution. Indeed, if different definitions of approximations of observables such as the density exist, the one *d*irectly using the flow Eq. (7.3) should have the smallest systematic uncertainty.

For our investigation we write the effective action as

$$\Gamma_k = \Gamma_k[\psi, \phi; \vec{g}], \quad \vec{g} = (m_\psi, m_\phi, S_\psi, S_\phi\,, h, \lambda_\psi, \lambda_\phi, ...)\,,$$

where $\vec{g}$ encodes all couplings (expansion coefficients) of the effective action, ordered in decaying mass dimension. We conclude that in three spatial dimensions the only couplings that potentially require μ-dependent initial conditions are the mass parameters (including μ itself). However, the flow of the dimer mass reads asymptotically

$$\partial_t m_\phi^2 \propto k \frac{h^2}{k} (1 + \mu/k^2)^{3/2}$$

and hence its μ-derivative tends towards zero, and the only coupling to be taken care of is the fermionic mass (and chemical potential).

7.1.2 Density

As already mentioned above, the equation for the density with the smallest systematic error is its flow. According to Eq. (7.2) for the non-relativistic case it reads

$$\partial_t n = \frac{1}{\mathrm{Vol}} \frac{d \partial_t \Gamma_k}{d\mu} \to c_{n,3} k^3 + c_{n,1} \mu\, k + O(\hat{k}^{-1})\,,$$

and a similar equation holds for the relativistic case. In the present case this leaves us with a cubic fine-tuning problem in the cutoff, and more importantly, a subleading linear fine-tuning problem for each value of μ. Fine-tuning problems of this type are difficult to resolve directly, and we do this by considering the flows of susceptibilities. The flow of the second order susceptibility reads

$$\partial_t \partial_\mu n = \frac{1}{\mathrm{Vol}} \frac{d^2 \partial_t \Gamma_k}{d\mu^2} \to c_{n,1} k + O(\hat{k}^{-1})\,,$$

while the flow of the second μ-derivative of the density tends towards zero for large cutoff scales,

$$\partial_t \partial_\mu^2 n = \frac{\partial_\mu^3 \partial_t \Gamma_k}{\mathrm{Vol}} \to O(\hat{k}^{-1})\,,$$

We conclude that the density, and the second order susceptibility at vanishing cutoff, $k = 0$, can be obtained from integrating the third order susceptibility, which has a trivial initial condition for large cutoff scales. We are led to,

$$n(\mu) = \int_0^\mu d\mu' \partial_{\mu'} n(\mu') \,, \quad \text{with} \quad n(0) = 0 \,,$$

for the density, and

$$\partial_\mu n(\mu) = \int_0^\mu d\mu' \, \partial_{\mu'}^2 n(\mu') \,, \quad \text{with} \quad \partial_\mu n(0) = 0 \,,$$

for the second order susceptibility. It is left to determine $\partial_\mu^2 n_k(\mu)$. To that end we rewrite the flow of the density as

$$\partial_t n_k = \frac{d\partial_t \Gamma_k}{d\mu} = \partial_\mu|_{\vec{g}} \, \partial_t \Gamma_k + \frac{dg_i}{d\mu} \partial_{g_i} \partial_t \Gamma_k \,.$$

Both terms follow analytically from the master equation, Eq. (7.3), and each partial μ-derivatives and $dg_i/d\mu \, \partial_{g_i}$-derivative lowers the effective k-dimension by two. The coefficients $g_i^{(1)} = dg_i/d\mu$ with

$$g_i^{(n)} = \frac{d^n g_i}{d\mu^n}$$

follow from their flow

$$\partial_t g_i^{(1)} = \frac{d}{d\mu} \partial_t g_i = \partial_\mu \partial_t g_i + g_j^{(1)} \partial_{g_j} \partial_t g_i \,. \tag{7.4}$$

Eq. (7.4) is a coupled differential equation for $\vec{g}^{(1)}$,

$$\partial_t \vec{g}^{(1)} = \vec{A}_1 + B_1 \cdot \vec{g}^{(1)} \tag{7.5}$$

with coefficients

$$A_{1,i} = \partial_\mu \partial_t g_i \,, \quad B_{1,ij} = \partial_{g_j} \partial_t g_i \,.$$

The coefficients $A_{1,i}$ and $B_{1,ij}$ can be read-off from the flow Eq. (7.3), and hence Eq. (7.5) is a so-called derived flow: it does not feed back into the flow of the effective action. Naturally, this can be iteratively extended to the higher derivatives w.r.t. μ. For $g_i^{(2)}$ it reads

$$\begin{aligned} \partial_t g_i^{(2)} &= \frac{d}{d\mu} \left(A_{1,i} + B_{1,ij} \, g_j^{(1)} \right) \\ &= \partial_\mu A_{1,i} + g_j^{(1)} \partial_{g_j} A_{1,i} + g_j^{(1)} \left(\partial_\mu + g_m^{(1)} \partial_{g_m} \right) B_{1,ij} + B_{1,ij} \, g_j^{(2)} \,. \end{aligned}$$

Again this can be conveniently rewritten in terms of a system of linear differential equations

$$\partial_t \vec{g}^{(2)} = \vec{A}_2 + B_2 \cdot \vec{g}^{(2)} \,,$$

with

$$A_{2,i} = \left(\partial_\mu + g_m^{(1)}\partial_{g_m}\right) A_{1,i} + g_j^{(1)} \left(\partial_\mu + g_m^{(1)}\partial_{g_m}\right) B_{1,ij}\,,$$

$$B_{2,ij} = B_{1,ij}\,.$$

More explicitly we have

$$A_{2,i} = \partial_\mu^2 \partial_t g_i + 2 g_j^{(1)} \partial_{g_j}\partial_\mu \partial_t g_i + g_j^{(1)} g_m^{(1)} \partial_{g_m}\partial_{g_j}\partial_t g_i\,,$$

$$B_{2,ij} = \partial_{g_j}\partial_t g_i\,.$$

This already allows us to put down the general structure. At a given order $g_i^{(n)}$ the matrix B_n is simply B_1. The vector A_n depends on $\vec{g}, \vec{g}^{(1)}, ..., \vec{g}^{(n-1)}$. Hence it can be determined iteratively with

$$A_{n,i} = \left(\partial_\mu + \sum_{m=1}^{n-1} g_j^{(m)} \partial_{g_j^{(m-1)}}\right) A_{n-1,i} + g_j^{(n-1)} \left(\partial_\mu + g_m^{(1)}\partial_{g_m}\right) B_{ij}$$

with $g_i^{(0)} = g_i$ and

$$\left(\partial_\mu + g_m^{(1)}\partial_{g_m}\right) B_{ij} = \partial_\mu \partial_{g_j}\partial_t g_i + g_m^{(1)}\partial_{g_m}\partial_{g_j}\partial_t g_i\,.$$

For $n = 3$ this explicitly yields

$$\begin{aligned} A_{3,i} = \Big[&\partial_\mu^3 + 3\, g_j^{(1)}\, \partial_{g_j}\, \partial_\mu^2 + 3\, g_j^{(1)}\, g_m^{(1)}\, \partial_{g_m}\, \partial_{g_j}\, \partial_\mu \\ &+ g_k^{(1)}\, g_j^{(1)}\, g_m^{(1)}\, \partial_{g_m}\, \partial_{g_j}\, \partial_{g_k} + 3\, g_m^{(2)}\, \partial_{g_m}\, \partial_\mu + 3\, g_j^{(2)}\, g_m^{(1)}\, \partial_{g_m}\, \partial_{g_j} \Big]\, \partial_t\, g_i\,. \end{aligned}$$

Note that there are multiple possible definitions for the coefficients A_n and B_n. The above forms have the advantage that all derivatives w.r.t. μ and $g_i^{(n)}$ can be performed analytically. Finally we write down the flow for higher μ-derivatives of Γ_k

$$\partial_\mu^{(n-1)} \dot{n}(\mu) = \frac{d^n \partial_t \Gamma}{d\mu^n} = \left(\partial_\mu + \sum_{m=1}^{n} g_j^{(m)} \partial_{g_j^{(m-1)}}\right) C_{n-1}\,,$$

with

$$C_0 = \partial_t\, \Gamma_k\,, \qquad C_1 = \partial_\mu\, \partial_t\, \Gamma_k\,.$$

For $n = 2$ this explicitly yields

$$\partial_\mu\, \partial_t\, n_k = \frac{d^2\, \partial_t\, \Gamma_k}{d\mu^2} = \Big[\partial_\mu^2\big|_{\vec{g}} + \, 2\, g_i^{(1)}\, \partial_{g_i}\, \partial_\mu \, + g_j^{(1)}\, g_i^{(1)}\, \partial_{g_i}\, \partial_{g_j} + g_i^{(2)}\, \partial_{g_i}\Big]\, \partial_t\, \Gamma_k\,,$$

while the second μ-derivative of the flow for the density is found to be

$$\begin{aligned} \partial_\mu^2\, \partial_t\, n_k =& \frac{d^3\, \partial_t\, \Gamma_k}{d\mu^3} \\ =& \Big[\partial_\mu^3|_{\vec{g}} + 3\, g_i^{(1)}\, \partial_{g_i}\, \partial_\mu^2 + 3\, g_j^{(1)}\, g_i^{(1)}\, \partial_{g_i}\, \partial_{g_j}\, \partial_\mu \\ &+ g_m^{(1)}\, g_j^{(1)}\, g_i^{(1)}\, \partial_{g_i}\, \partial_{g_j}\, \partial_{g_m} + 3\, g_i^{(2)}\, \partial_{g_i}\, \partial_\mu + 3\, g_i^{(2)}\, g_j^{(1)}\, \partial_{g_j}\, \partial_{g_i} + g_i^{(3)}\, \partial_{g_i} \Big]\, \partial_t\, \Gamma_k\,. \end{aligned} \tag{7.6}$$

Hence, overall the density at vanishing cutoff $k = 0$ is obtained by integrating twice over the chemical potential

$$n(\mu) = \int_0^\mu d\mu' \left[\int_0^{\mu'} d\mu'' \, \partial_{\mu''}^2 \, n(\mu'') + \partial_{\mu'} \, n(0) \right] + \, n(0) \, , \tag{7.7}$$

where $n(0)$ and $\partial_\mu \, n(0)$ are vanishing.

Moreover, we have

$$\partial_\mu^2 \, n_{k=0}(\mu) = \int_\Lambda^0 \frac{dk}{k} \, \partial_\mu^2 \, \dot{n}_k(\mu) \, ,$$

for a UV vanishing flow $\partial_\mu^2 \, \dot{n}_{k\to\infty} \to 0$. To sum up, this procedure leaves us with a closed set of equations and we obtain the density from integrating the third order susceptibility $n^{(2)}$ from $\mu = 0$ with the initial conditions $n(0) = 0$ and $n^{(1)}(0) = 0$ to μ, leading to our results in Sec. 7.4.

7.2 Definition of ultraviolet finite flows

7.2.1 Ultraviolet divergence while regularising around Fermi surface

In this Section, we show that our choice of the regulator for the fermions introduces an additional ultraviolet divergence, and we discuss in detail how to remove this contribution. This solves a major technical challenge of the present approach with our choice of regulators. Using an optimised Litim-type regulator for the fermions of the form Eq. (4.19) which regularises around the Fermi surface, there is a divergence in the UV due to the appearance of an additional sgn-term in the flow equations.

This can be seen as follows: The fermionic part of the flow of the bosonic wavefunction renormalisation $S_\phi = Z_\phi / A_\phi$ is given, as in (4.37), by

$$\dot{S}_\phi^{(F)} = -\frac{16 \, v_d}{d} \, h_k^2 \, k^{d-4} \left(\ell_F^{(0,2)} - 2 \, w_3 \, \ell_F^{(0,3)} \right) .$$

Here we used the definitions in Eqs. (4.39), (4.40) and (E.5). At zero temperature, in three spatial dimensions and in the symmetric regime this becomes

$$\dot{S}_\phi^{(F)} = \alpha_{S_\phi} \, k^{-1} \, h_k^2 \left[\theta(\tilde{\mu} + 1) \, (\tilde{\mu} + 1)^{3/2} - 2 \, \theta(\tilde{\mu}) \, \tilde{\mu}^{3/2} \right] , \qquad \text{for } T = 0, \text{ SYM} \tag{7.8}$$

with a (k-independent) constant α_{S_ϕ} and where the term $2 \, \theta(\tilde{\mu}) \, \tilde{\mu}^{3/2}$ appears due to the additional sgn-term in the regulator around the Fermi surface. We dropped the term $\theta(\tilde{\mu} - 1) \, \theta(\tilde{\mu} - 1)$, as it vanishes due to $k^2 > \mu$ in the symmetric regime (with $\tilde{\mu} = \mu / k^2$). The Yukawa or Feshbach coupling h_k is attracted to a (partial) fixed point and has the scaling behaviour $h_k \sim \sqrt{6 \, \pi^2 \, k}$ in the ultraviolet, so that

$$\dot{S}_\phi^{(F)} = \alpha_{S_\phi} \left[\theta(\tilde{\mu} + 1) \, (\tilde{\mu} + 1)^{3/2} - 2 \, \theta(\tilde{\mu}) \, \tilde{\mu}^{3/2} \right] , \qquad \text{for } T = 0, \text{ SYM}$$

subsuming the factor of $6\,\pi^2$ under the coefficient α_{S_ϕ}. Taking three (partial) μ-derivatives yields

$$\partial_\mu^3 \dot{S}_\phi^{(F)} = \tilde{\alpha}_{S_\phi} \left[\frac{\theta(\tilde{\mu}+1)}{(\tilde{\mu}+1)^{3/2}} - 2\,\frac{\theta(\tilde{\mu})}{\tilde{\mu}^{3/2}} \right], \qquad \text{for } T=0, \text{ SYM}$$

As the term proportional to $\tilde{\mu}^{-3/2} = \mu^{3/2}/k^3$ is only present for a regulator around the Fermi surface, we find in the ultraviolet

$$\partial_\mu^3 S_\phi^{(F)} \propto \begin{cases} k^{-3} & \text{regulator around Fermi surface} \\ k^{-6} & \text{otherwise} \end{cases} . \tag{7.9}$$

Regarding the flow of the effective action we have in the ultraviolet at $T=0$ and in the symmetric regime

$$\dot{V}(\rho) = \beta_{V^{(F)}}\, k^5\, (\tilde{\mu}+1)^{3/2}\, \theta(\tilde{\mu}+1) + \beta_{V^{(B)}}\, \frac{k^5}{S_\phi} \left(1 - \frac{\eta_\phi}{5}\right), \tag{7.10}$$

Here we again split the k-independent coefficients into $\beta_{V^{(F/B)}}$ for the fermionic and bosonic contributions, respectively.
Considering the second μ-derivative of flow of the density in Eq. (7.6) we find from (7.10) in the last term $g_i^{(3)}\,\partial_{g_i}\,\partial_t\,\Gamma_k$ for the couplings $g_i = \{S_\phi, \eta_\phi\}$

$$\begin{aligned} \partial_{S_\phi}\,\dot{\Gamma}_k &= \gamma\,\frac{k^5}{S_\phi^2}\left(1-\frac{\eta_\phi}{5}\right), \\ \partial_{\eta_\phi}\,\dot{\Gamma}_k &= \tilde{\gamma}\,\frac{k^5}{S_\phi^2}, \end{aligned} \tag{7.11}$$

where $\eta_\phi \sim k^0$ in the ultraviolet and γ, $\tilde{\gamma}$ being k-independent.
From (7.9) and (7.11) we infer that the last term in Eq. (7.6) is therefore proportional to

$$g_i^{(3)}\,\partial_{g_i}\,\partial_t\,\Gamma_k \propto \begin{cases} k^2 & \text{regulator around Fermi surface} \\ k^{-1} & \text{otherwise} \end{cases} .$$

Hence, with a regulator around the Fermi surface, we encounter a divergence in the ultraviolet, which is not present otherwise. Note that we used that $S_\phi \sim k^0$ in the UV.

The above argument can be easily generalised to finite temperature, as the only difference is that the constant α_{S_ϕ} in Eq. (7.8) contains a term proportional to the Fermi-Dirac distribution $\tilde{N}_F$, Eq. (E.2), arising from the Matsubara summation Eq. (E.1). In the ultraviolet, where $k \to \infty$, the Fermi-Dirac distribution with the renormalised temperature $\tilde{T} = T/k^2$ vanishes, $\tilde{N}_F \to 0$, and exactly the same structure as above is retained.

7.2.2 Splitting into ultraviolet and infrared flow

However, as the Fermi surface is only relevant in the infrared, we do not need to regularise around the Fermi surface in the ultraviolet. We may rather employ an overall regulator combined out of an infrared part which regularises around the Fermi surface and an ultraviolet part which does not

$$R_\psi = R^{\mathrm{UV}}\,\theta^{\mathrm{UV}} + R^{\mathrm{IR}}\,\theta^{\mathrm{IR}}\,, \tag{7.12}$$

where we choose $\theta^{\mathrm{UV}} = \theta(k-k_0)$ and $\theta^{\mathrm{IR}} = (1-\theta^{\mathrm{UV}})$ with $\theta(x)$ being the Heaviside step function. The scale k_0 at which the switch between ultraviolet and infrared regulator takes place will be chosen appropriately such that the correct physical behaviour is obtained. The advantage of employing a sharp switch between the infrared and ultraviolet regulator is the possibility to analytically perform all integrations and Matsubara sums. For a smooth switching behaviour one would have to deal with both the influence of the switching function itself, as well as the contributions of the infrared and ultraviolet part in a certain switching region.
The derivative of the fermion regulator R_ψ w.r.t. the RG-time t is thus given by

$$\dot{R}_\psi = k\,\partial_k\,R_\psi = \dot{R}^{\mathrm{UV}}\,\theta^{\mathrm{UV}} + \dot{R}^{\mathrm{IR}}\,\theta^{\mathrm{IR}} + k\,\delta_{k,k_0}\,\left(R^{\mathrm{UV}} - R^{\mathrm{IR}}\right)\,, \tag{7.13}$$

where we use the shorthand notation $\delta_{k,k_0} = \delta(k-k_0)$.
With the definition of $z := (q^2-\mu)/k^2$ we choose

$$R_\psi^{\mathrm{UV}}(q^2) = k^2\;(1-z)\;\theta\,(1-z)$$

for the UV regulator and accordingly

$$R_\psi^{\mathrm{IR}}(q^2) = k^2\;(\mathrm{sgn}\,(z)-z)\;\theta\,(1-|z|)$$

for the IR regulator which still appropriately regularises around the Fermi surface in the infrared, cf. Eq. (4.19).
Hence, with the inverse fermion propagator given, as in Eq. (4.12), by

$$G_\psi^{-1}(Q) = \begin{pmatrix} -h\,\phi\,\varepsilon & -P_\psi^{-Q}\,\mathbb{1} \\ P_\psi^{Q}\,\mathbb{1} & h\,\phi\,\varepsilon \end{pmatrix}$$

and the regulator, as in Eq. (4.13), being

$$R_\psi^Q = \begin{pmatrix} 0 & -R_{\mathrm{UV}}^{-Q}\,\mathbb{1} \\ R_{\mathrm{UV}}^{Q}\,\mathbb{1} & 0 \end{pmatrix}\theta^{\mathrm{UV}} + \begin{pmatrix} 0 & -R_{\mathrm{IR}}^{-Q}\,\mathbb{1} \\ R_{\mathrm{IR}}^{Q}\,\mathbb{1} & 0 \end{pmatrix}\theta^{\mathrm{IR}}$$

we find

$$G_\psi^{-1}(Q) + R_\psi^Q = \begin{pmatrix} -a & -b^{-Q} \\ b^{Q} & a \end{pmatrix}\theta^{\mathrm{UV}} + \begin{pmatrix} -a & -c^{-Q} \\ c^{Q} & a \end{pmatrix}\theta^{\mathrm{IR}} \tag{7.14}$$

where we defined $a := h\,\phi\,\varepsilon$, $b^Q := \left(P_\psi^Q + R_{\mathrm{UV}}^Q\right)\mathbb{1}$ and $c^Q := \left(P_\psi^Q + R_{\mathrm{IR}}^Q\right)\mathbb{1}$.
Inverting Eq. (7.14) the propagator is thus found to be

$$\begin{aligned} G_\psi^Q &= \frac{1}{\det_{\mathrm{F}}^Q}\begin{pmatrix} a\left(\theta^{\mathrm{UV}}+\theta^{\mathrm{IR}}\right) & b^{-Q}\,\theta^{\mathrm{UV}} + c^{-Q}\,\theta^{\mathrm{IR}} \\ -b^Q\,\theta^{\mathrm{UV}} - c^Q\,\theta^{\mathrm{IR}} & -a\left(\theta^{\mathrm{UV}}+\theta^{\mathrm{IR}}\right)\end{pmatrix} \\ &=: G^{\mathrm{UV}}\,\theta^{\mathrm{UV}} + G^{\mathrm{IR}}\,\theta^{\mathrm{IR}} \end{aligned} \tag{7.15}$$

where we defined

$$G^{\mathrm{UV}}(Q) = \frac{1}{\det_{\mathrm{F}}^Q}\begin{pmatrix} a & b^{-Q} \\ -b^Q & -a\end{pmatrix}, \qquad G^{\mathrm{IR}}(Q) = \frac{1}{\det_{\mathrm{F}}^Q}\begin{pmatrix} a & c^{-Q} \\ -c^Q & -a\end{pmatrix}.$$

The determinant is then given by

$$\begin{aligned} \det_{\mathrm{F}}^Q &= = -a^2\,\left(\theta^{\mathrm{UV}}+\theta^{IR}\right) + b^Q\,b^{-Q}\,\theta^{\mathrm{UV}} + c^Q\,c^{-Q}\,\theta^{\mathrm{IR}} \\ &= -a^2\, + b^Q\,b^{-Q}\,\theta^{\mathrm{UV}} + c^Q\,c^{-Q}\,(1-\theta^{\mathrm{UV}})\,. \end{aligned}$$

Thus, the flow equations for the effective potential, cf. Eq. (4.20), and for the couplings, obtained via appropriate projection descriptions, see Sec. 4.4, split up into a purely UV- and purely IR-part, as well as a term which is proportional to $(R^{\mathrm{UV}} - R^{\mathrm{IR}})\,\delta_{k,k0}$. Here, the derivative w.r.t. the RG-time t acts on θ^{UV} and θ^{IR}, respectively.
Due to the overall Heaviside step functions θ^{UV} (θ^{IR}) in Eq. (7.15) for the UV- (IR-) contribution the determinant $\det_{\mathrm{F}}^Q$ simplifies in both regimes

$$\det_{\mathrm{F}}^Q = \begin{cases} -a^2\, + b^Q\,b^{-Q} =: \det_{\mathrm{F}}^{\mathrm{UV}}(Q) & \text{in the UV} \\ -a^2\, + c^Q\,c^{-Q} =: \det_{\mathrm{F}}^{\mathrm{IR}}(Q) & \text{in the IR} \end{cases}. \tag{7.16}$$

Together with the overall $\dot{R}^{\mathrm{UV/IR}}$ in the fermionic flow equations, Eq. (7.16) results in

$$\det_F^{\mathrm{UV}} = \det_F^{\mathrm{IR}} = \det_F^{\mathrm{eff}} = S_\psi^2\,q_0^2 + k^4 + h^2\,\rho\,.$$

Hence, at scales smaller than the switching scale $k \leq k_0$ (i.e. in the infrared) we find exactly the same flow equations as before for the regulator around the Fermi surface, cf. Sec. 4.5. In the ultraviolet, however, the flow equations are modified and for the momentum integration one obtains

$$\begin{aligned} \int_{\vec{q}} \dot{R}_\psi^{\mathrm{UV}}\,\left(L_\psi^S\right)^n &= \frac{8\,v_d}{d}\,k^{d+2+2n}\,\ell^{\mathrm{UV}}(\tilde{\mu})\,, \\ \int_{\vec{q}} \dot{R}_\psi^{\mathrm{UV}}\,\left(L_\psi^S\right)^{2n+1} &= \frac{8\,v_d}{d}\,k^{d+4+4n}\,\ell^{\mathrm{UV}}(\tilde{\mu}) \end{aligned} \tag{7.17}$$

and

$$\int_{\vec{q}} \dot{R}_\psi^{\mathrm{UV}}\,q^2\,x^2\,R_\psi^{(2)}\,\left(L_\psi^S\right)^n = \frac{2\,v_d}{d}\,k^{d+2+2n}\,\ell^{\mathrm{UV}}(\tilde{\mu})\,. \tag{7.18}$$

According to Eq. (E.5), we defined $\ell^{\mathrm{UV}}(\tilde{\mu}) = (1+\tilde{\mu})^{d/2}\ \theta\,(1+\tilde{\mu})$ in an analogous manner. The evaluation of the Matsubara sum yields the same result as in the infrared case of the regulator around the Fermi surface, see Eq. (E.1).
Thus, defining an overall threshold function with Eq. (7.17) and Eq. (7.18) we obtain

$$\int_Q \dot{R}_\psi^{\mathrm{UV}}\ \frac{\left(L_\psi^S\right)^n}{\det_F^m} = \frac{8\,v_d\,k^{d+2n+4-4m}}{d}\,\ell_{F,\mathrm{UV}}^{(m)}$$

$$\int_Q \dot{R}_\psi^{\mathrm{UV}}\ q^2\,x^2\,R_\psi^{(2)}\ \frac{\left(L_\psi^S\right)^n}{\det_F^m} = \frac{2\,v_d\,k^{d+2n+4-4m}}{d}\,\ell_{F,\mathrm{UV}}^{(m)}\,.$$

The threshold function for fermionic diagrams is given by

$$\ell_{F,\mathrm{UV}}^{(m)}\left(\tilde{\mu},\tilde{T},w_3\right) = \ell^{\mathrm{UV}}(\tilde{\mu})\,\mathcal{F}_m\big(\sqrt{1+w_3}\big)\ ,$$

where we set $S_\psi = A_\psi = 1$ and defined $w_3 = h^2\,\rho/k^4$ as before, cf. Section 4.5.2.

Contributions proportional to the delta function

The last term in Eq. (7.13) is generated by the RG-time derivative t acting on the Heaviside step function $\theta^{\mathrm{UV/IR}}$ itself and hence contains the delta function δ_{k,k_0}. For a more straight forward evaluation, one can rewrite the regulator Eq. (7.12) using the identity that the nth power of the Heaviside function is the Heaviside function itself, $\theta^n(x) \equiv \theta(x)$.

$$R_\psi = R^{\mathrm{UV}}\ \left(\theta^{\mathrm{UV}}\right)^2 + R^{\mathrm{IR}}\ \left(\theta^{\mathrm{IR}}\right)^2\ .$$

The advantage is that the t-derivative of the regulator clearly splits into an ultraviolet and infrared part also for the third term containing the delta function

$$\dot{R}_\psi = k\,\partial_k\,R_\psi = \dot{R}^{\mathrm{UV}}\,\theta^{\mathrm{UV}} + \dot{R}^{\mathrm{IR}}\,\theta^{\mathrm{IR}} + 2\,\left(R^{\mathrm{UV}}\,\theta^{\mathrm{UV}} - R^{\mathrm{IR}}\,\theta^{\mathrm{IR}}\right)\,\dot{\theta}^{\mathrm{UV}}\,. \tag{7.19}$$

With this definition in Eq. (7.19) the δ-contribution of the effective potential, due to the last term in Eq. (7.19), can be calculated as follows

$$V^{(\mathrm{F}),\delta} = -\,\mathrm{tr}\int_Q \left(\overline{G}_\psi^{Q,\mathrm{UV}}\,\theta^{\mathrm{UV}} + \overline{G}_\psi^{Q,\mathrm{IR}}\,\theta^{\mathrm{IR}}\right)\,\dot{\theta}^{\mathrm{UV}}\,\left(\overline{R}_\psi^{Q,\mathrm{UV}}\,\theta^{\mathrm{UV}} - \overline{R}_\psi^{Q,\mathrm{IR}}\,\theta^{\mathrm{IR}}\right)\ .$$

This simplifies to a purely ultraviolet, as well as purely infrared part and can, with the definition of the symmetrised components of the propagator in Eq. (4.14), be written as

$$V^{(\mathrm{F}),\delta} = -2\int_Q \frac{L_\psi^{Q,S,\mathrm{UV}}}{\det_F^{Q,\mathrm{UV}}}\,\theta^{\mathrm{UV}}\,R_\psi^{Q,\mathrm{UV}}\,\dot{\theta}^{\mathrm{UV}} + 2\int_Q \frac{L_\psi^{Q,S,\mathrm{IR}}}{\det_F^{Q,\mathrm{IR}}}\,\theta^{\mathrm{IR}}\,R_\psi^{Q,\mathrm{IR}}\,\dot{\theta}^{\mathrm{IR}}\,. \tag{7.20}$$

Overall, with these definitions we then find the contributions proportional to the delta function at zero temperature. Note, that in order to perform the integration over the RG-time integration t we recall that for integrands of the form $\delta(k-k_0)\,\theta(k-k_0)$ the

integration procedure is only well-defined in terms of distribution theory. This results in an overall factor of $\delta(k-k_0)/2$ so that in the end we have

$$\begin{aligned} V^{(\delta)} &= -\frac{16\, v_d\, k^{d+2}}{d(d+2)} \left[\theta_-\, \tilde{\mu}_-^{d/2+1} - 2\,\theta(\tilde{\mu})\tilde{\mu}^{d/2+1}\right] \mathcal{F}_1^{T=0}(\sqrt{1+w_3})\, \delta_{k,k_0}\,, \\ S_\phi^{(\delta)} &= \frac{32\, v_d\, h_k^2\, k^{d-4}}{d(d+2)} \left[\theta_-\, \tilde{\mu}_-^{d/2+1} - (d+2)\,\theta(\tilde{\mu})\tilde{\mu}^{d/2}\right] \\ &\qquad \times \left(\mathcal{F}_2^{T=0}(\sqrt{1+w_3}) - 2\, w_3\, \mathcal{F}_3^{T=0}(\sqrt{1+w_3})\right)\, \delta_{k,k_0}\,, \\ \eta_\phi^{(\delta)} &= 0\,. \end{aligned} \tag{7.21}$$

In addition to using the definition of $\mathcal{F}_i$ in Eq. (E.1) we also defined $\theta_\pm = \theta(\tilde{\mu}_\pm)$ with $\tilde{\mu}_\pm = \mu/k^2 \pm 1$ for a more compact notation and offer a more detailed derivation of Eq. (7.21) in Appendix B.

7.2.3 Independence on switching scale

In order to apply the splitting of the flow into an ultraviolet and an infrared part, laid out in Sec. 7.2.1, the density resulting from the integrated 1-loop fermion flow has to be independent of the scale k_0 at which the flow is switched.
According to (7.6) and (7.7) we have to solve the flow of the third (total) μ-derivative of the effective action and integrate twice over the chemical potential. As we only consider the 1-loop fermion flow in the symmetric regime, contributions proportional to $g_i^{(1)}$ and $g_i^{(2)}$ vanish since they are determined by their flow. For the flow of the second μ-derivative of the density we the have

$$\partial_\mu^2\, \partial_t\, n_k = \frac{d^3\, \partial_t\, \Gamma_k}{d\, \mu^3} = \partial_\mu^3|_{\vec{g}}\, \partial_t\, \Gamma_k\,, \tag{7.22}$$

with $g_i^{(n)} \equiv 0$ vanishing, as $g_i^{(n)}$ are determined by its flow.
It is sufficient to show that already $\partial_\mu^2\, n_{k\to 0}$ is independent of the switching scale k_0

$$\partial_\mu^2\, n_{k\to 0} = \int_\Lambda^0 \frac{dk}{k}\, \partial_\mu^2\, \partial_t\, n_k + \partial_\mu^2\, n_{k=\Lambda}\,.$$

Here, the second term $\partial_\mu^2\, n_{k=\Lambda}$ vanishes for a sufficiently large UV cutoff $\Lambda \to \infty$.
According to Eq. (3.14) we have for the flow equation for the 1-loop approximation

$$\partial_t\, \Gamma_k^{(\mathrm{F}),\text{1-loop}} = -\frac{1}{2}\, \mathrm{Tr}\, \frac{1}{S_k^{(2)}[\phi] + R_k}\, \partial_t R_k\,, \tag{7.23}$$

with $S_k[\phi]$ being the classical action.
From Eq. (7.23) we find for the 1-loop fermion flow equation of the effective potential

$$\dot{V}^{(\mathrm{F}),1-\text{loop}} = \dot{V}^{(\mathrm{F}),1-\text{loop,UV}}\, \theta^{\mathrm{UV}} + \dot{V}^{(\mathrm{F}),1-\text{loop,IR}}\, \theta^{\mathrm{IR}} + V^{(\mathrm{F}),1-\text{loop},\delta}\,. \tag{7.24}$$

Here we split the equation in the ultraviolet and infrared part, as well as in a contribution arising from the RG-time derivative acting on the Heaviside function $\theta^{\mathrm{UV}} = 1 - \theta^{\mathrm{IR}}$, cf. the last term in Eq. (7.13).
For the ultraviolet and infrared contributions in Eq. (7.24) we find

$$\dot{V}^{(\mathrm{F}),1-\mathrm{loop},\mathrm{UV}}\,\theta^{\mathrm{UV}} + \dot{V}^{(\mathrm{F}),1-\mathrm{loop},\mathrm{IR}}\,\theta^{\mathrm{IR}} = \alpha_k \left[\left(\theta_+\,\tilde{\mu}_+^{3/2} - \theta_-\,\tilde{\mu}_-^{3/2}\right)\,\theta^{\mathrm{IR}} + \left(\theta_+\,\tilde{\mu}_+^{3/2}\right)\,\theta^{\mathrm{UV}}\right] ,$$

with $\alpha_k = -32\,v_d/d\,k^{d+2}\,\left(\frac{1}{2} - \tilde{N}_F\left(\sqrt{1+w_3}\right)\right)$ a μ-independent coefficient. We introduced the short-hand notations $\tilde{\mu}_+ = \tilde{\mu} + 1$ and $\tilde{\mu}_- = \tilde{\mu} - 1$ and used again $\theta^{\mathrm{UV}} = \theta(k - k_0)$, $\theta^{\mathrm{IR}} = 1 - \theta^{\mathrm{UV}}$ and the Fermi-Dirac distribution $\tilde{N}_F$ given in Eq. (E.2).

Zero temperature case

At zero temperature, ultraviolet and infrared contributions in Eq. (7.24) simplify to

$$\begin{aligned}\dot{V}_{T=0}^{(\mathrm{F}),1-\mathrm{loop},\mathrm{UV}}\,\theta^{\mathrm{UV}} + \dot{V}_{T=0}^{(\mathrm{F}),1-\mathrm{loop},\mathrm{IR}}\,\theta^{\mathrm{IR}} \\ = \alpha_{k,T=0} \left[\left(\theta_+\,\tilde{\mu}_+^{3/2} - \theta_-\,\tilde{\mu}_-^{3/2}\right)\,\theta^{\mathrm{IR}} + \left(\theta_+\,\tilde{\mu}_+^{3/2}\right)\,\theta^{\mathrm{UV}}\right] ,\end{aligned}$$

with $\alpha_{k,T=0} = -16\,v_d/d\,k^{d+2}$ a μ-independent coefficient and the other definitions as above. For the third (total) derivative of the effective potential w.r.t. the chemical potential, which in the 1-loop case turns into a partial μ-derivative according to Eq. (7.22), we the find

$$\frac{d^3\,\dot{V}_{T=0}^{(\mathrm{F}),1-\mathrm{loop}}}{d\mu^3} = \frac{1}{8\,\pi^2\,k}\left[\frac{\theta_+}{\tilde{\mu}_+^{3/2}}\,\theta^{\mathrm{UV}} + \left(\frac{\theta_+}{\tilde{\mu}_+^{3/2}} - \frac{\theta_-}{\tilde{\mu}_-^{3/2}}\right)\,\theta^{\mathrm{IR}}\right] + \delta_\pm^{(n)}\text{-terms}\,. \tag{7.25}$$

The $\delta_\pm^{(n)}$-terms result form the derivatives w.r.t. μ acting on the Heaviside step functions $\theta\,(\tilde{\mu} \pm 1)$, i.e. $\partial_\mu^n\,\theta_\pm = \delta_\pm^{(n)}$. We then always have combinations of $(\mu \pm 1)^{m/2}\,\delta_\pm^{(n)}$ with $m \in \{-1, 1, 3\}$ and $n \in \{1, 2, 3\}$. Since, in the end, we integrate twice over μ (as well as over the RG-time t), these $\delta_\pm^{(n)}$-terms vanish under the integrals.
For the integration over the RG-time t of Eq. (7.25) we then find

$$\begin{aligned}\int_\Lambda^0 \frac{dk}{k}\,\partial_\mu^3\,\dot{V}_{T=0}^{(\mathrm{F}),1\text{-loop}} &= \int_\Lambda^{k_0} \frac{dk}{k}\,\partial_\mu^3\,V_{T=0}^{(\mathrm{F}),1\text{-loop},\mathrm{UV}} + \int_{k_0}^0 \frac{dk}{k}\,\partial_\mu^3\,V_{T=0}^{(\mathrm{F}),1\text{-loop},\mathrm{IR}} \\ &= \frac{1}{8\,\pi^2}\left[\int_\Lambda^{k_0} \frac{dk}{k}\,\frac{\theta_+}{\tilde{\mu}_+^{3/2}} + \int_{k_0}^0 \frac{dk}{k}\left(\frac{\theta_+}{\tilde{\mu}_+^{3/2}} - \frac{\theta_-}{\tilde{\mu}_-^{3/2}}\right)\right] \\ &= \frac{1}{8\,\pi^2}\left(\frac{1}{\sqrt{\Lambda^2+\mu}} + \theta(\mu - k_0^2)\,\theta(\mu)\,\frac{1}{\sqrt{k_0^2-\mu}} - \frac{2}{\sqrt{\mu}}\,\theta(\mu)\right) .\end{aligned} \tag{7.26}$$

Combining Eq. (7.26) and the first equation in Eq. (7.21) we find that the dependence on the switching scale between ultraviolet and infrared flow in Eq. (7.26) drops out at zero

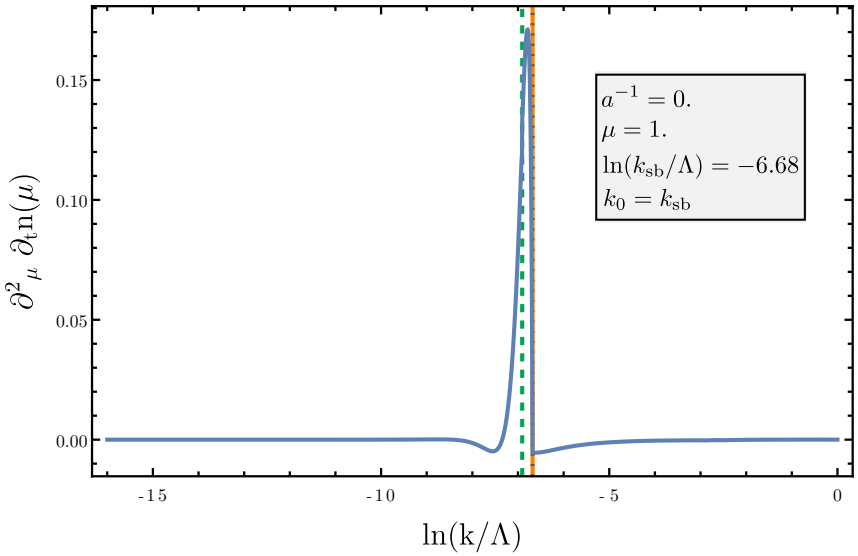

Figure 7.1: The flow of the second μ-derivative of the density, here exemplary shown for a diverging scattering length of $a^{-1} = 0$ and $\mu = 1$, is peaked around the switching scale $k_0 = k_{\rm sb}$. The solid orange line depicts the symmetry breaking scale $\ln(k_{sb}/\Lambda)$, while the green dashed line shows the chemical potential $\ln(\mu_{\rm mb}/\Lambda)$ and the grey dotted one the switching scale $\ln(k_0/\Lambda)$ which coincides with the symmetry breaking scale here.

temperature.

At finite temperature we have an additional factor of the Fermi-Dirac distribution in the flow equation of the effective potential. This complicates the integration over the RG-time t, cf. Eq. (7.26) for the zero temperature case, which can then be evaluated numerically. On the other hand, for the delta contribution Eq. (7.20) at finite temperature, the evaluation of the RG-time integration is also not trivial, since factors of $\theta(k - k_0)$ now occur in the Fermi-Dirac distribution as well and independence of k_0 is again checked numerically.

7.3 Resolution of divergences at $\mu = k^2$

As we described in Section 7.2.2 we use a Litim-type regulator for the fermions which regularises around the Fermi surface in the infrared, i.e. with $z := (q^2 - \mu)/k^2$ it is of the form

$$R_\psi^{(\rm IR)}(z) = k^2\ (1 - z)\ \theta\,(1 - z)\ ,$$

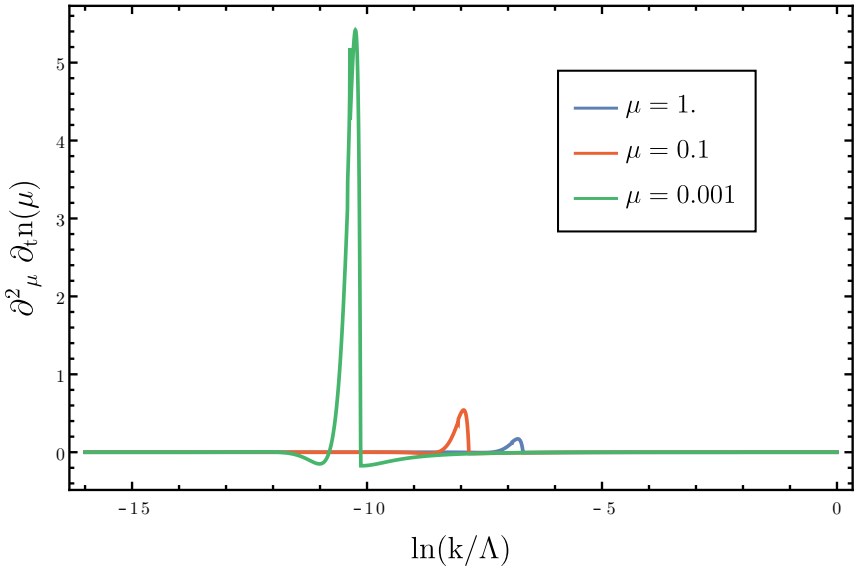

Figure 7.2: The flow of the second μ-derivative of the density, here exemplary shown for a scattering length of $a^{-1} = 0$ and different values of $\mu = \{0.001, 0.1, 1.\}$ (shown in green, red and blue from left to right). The lower the chemical potential the higher is the peak around the switching scale k_0.

Performing the momentum integration, as given in Appendix E, results in couplings g_i of the form

$$\dot{g}_i \propto \theta\left(\tilde{\mu} \pm 1\right) \left(\tilde{\mu} \pm 1\right)^{3/2} f(g_i, k)\,,$$

where $f(g_i, k)$ is a function of a combination of the k-dependent couplings and the flow parameter k. Taking μ-derivatives results in discontinuities starting at the second order due to the $(\tilde{\mu} - 1)$ term. Especially, the third μ-derivative results in a $3/2$ singularity and needs to be regulated. To this end, we employ the following regularisation

$$\frac{1}{\left(\tilde{\mu} - 1\right)^{3/2}} \theta\left(\tilde{\mu} - 1\right) \left[f(g_i, k^2) - f(g_i, \mu)\right]\,,$$

where $f(g_i, k)$ is the part of the flow equation finite in $\tilde{\mu} = \mu/k^2$.

7.4 Quantitative BCS-BEC crossover at zero temperature

We are now in the position to calculate the density over the whole BCS-BEC crossover. Here, we limit ourselves to the three-dimensional case at zero temperature, such that, in the following, the scattering length a always denotes the three-dimensional one $a \equiv a_{3\mathrm{D}}$. The generalisation to finite temperature and dimensions below three, e.g. the dimensional crossover from three to two dimensions, is in principle straightforward, albeit numerically

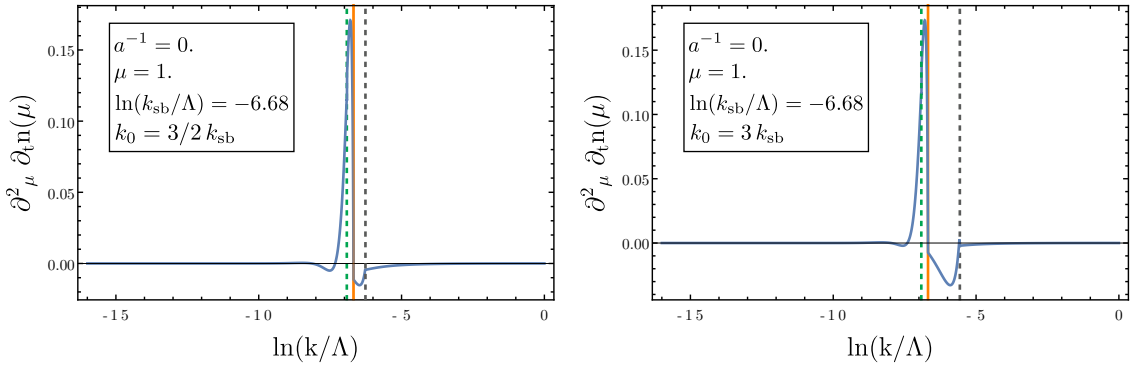

(a) The flow of the second μ-derivative of the density, here exemplary shown for a scattering length of $a^{-1} = 0$, $\mu = 1$ and $k_0 = 1.5 k_{sb}$.

(b) The flow of the second μ-derivative of the density, here exemplary shown for a scattering length of $a^{-1} = 0$, $\mu = 1$ and $k_0 = 3\, k_{sb}$.

Figure 7.3: The flow of the second μ-derivative of the density for a scattering length of $a^{-1} = 0$ and $\mu = 1$ at switching scales $k_0 > k_{sb}$. For larger switching scales k_0 we find an increased influence of the ultraviolet divergence when regularising around the Fermi surface.

more demanding.

We employ the same truncation, given in Eq. (4.18) and depicted in Fig. 4.1, as before, with a running boson propagator. We do not allow for a running fermion propagator at this stage whose inclusion, especially a running fermion mass m_ψ, might in the end the yield more accurate results.

Considering the flow of the second μ-derivative of the density, as shown exemplary for a diverging scattering length $a^{-1} = 0$ in Fig. 7.1, it is peaked around the switching scale k_0. The amplitude of the peak generally increases for lower values of the chemical potential μ, cf. Fig. 7.2.

The same behaviour can be found beyond unitarity, where we take care of the smaller symmetry breaking scale k_{sb} on the BCS-side of the crossover by running the flow until $t_{\rm final} = -20$ (for $a < 0$) and until $t_{\rm final} = -16$ (for $a \geq 0$) with a ultraviolet cutoff scale of $\Lambda/\sqrt{\mu_{\rm mb}} = 1000$. For additional details and plots cf. Appendix A. We have seen in Sec. 7.2.3 that the integrated flow is independent within 1-loop of the scale k_0 where we switch from an ultraviolet flow not regularising around the Fermi surface to an infrared flow which regularises around the Fermi surface. In practice however, the switching scale k_0 influences the result in the way that we see residual influences of the ultraviolet divergence for a regulator around the Fermi surface when choosing k_0 too large, cf. Figs. 7.3. We therefore set $k_0 = k_{sb}$ to the symmetry breaking scale for negative and zero scattering length $a \leq 0$. For positive scattering lengths the symmetry breaking occurs much earlier in the flow such that we choose $k_0 = 2/3\, k_{sb}$ in order to minimise the influence of the ultraviolet divergence.

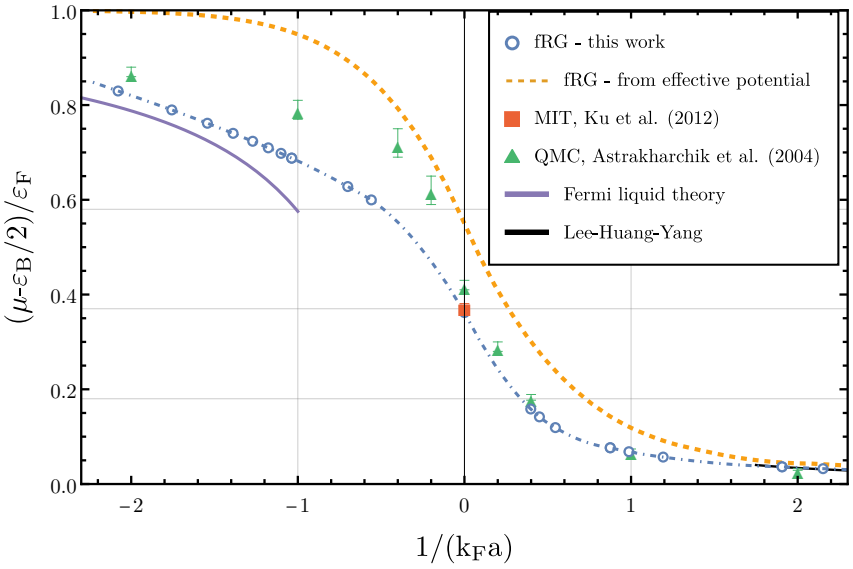

Figure 7.4: Comparison of the equation of state for the density iteratively calculated (blue open circles and dash-dotted blue line) with the one obtained from Fermi-liquid theory (FLT) in the BCS-regime (purple solid line), with the Lee-Huang-Yang results on the BEC-side (black diamond) and the one obtained from the effective potential calculation (dashed orange line). In addition, we show experimental data (red square) by the Zwierlein group at MIT (Ku et al.) [27] and by quantum Monte Carlo calculations (green triangles) by Astrakharchik et al. [28].

Moreover, we neglect all delta distributions in Eq. (7.21) except for the dominant contribution to the effective potential because of numerical stability. Including further delta distributions led to numerical instabilities and should have minute impacts on the results.

Note, that neglect data points where we see a residual influence of the diverging behaviour from the regulator around the Fermi surface. Furthermore, we set the initial condition at $k = \Lambda$ for our couplings $g_i^{(n)}$ with $n \in \{1, 2, 3\}$ to zero, while the initial conditions for the couplings $g_i^{(0)}$ are chosen as outlined in Sec. 4.7.2.

7.4.1 Equation of state

The result for the equation of state at zero temperature over the three-dimensional BCS-BEC crossover is shown in Fig. 7.4. We obtain for the Bertsch parameter $\xi = \mu/\epsilon_F|_{a\to\infty}$ at unitarity,

$$\boxed{\xi_{\mathrm{fRG}} \simeq 0.362 \qquad \text{for } k_0 = k_{\mathrm{sb}}},$$

in good quantitative agreement with the experimental value of $\xi_{\mathrm{exp}} = 0.376(5)$ from [27]. Here, we compare the equation of state from this iterative procedure to the fRG result

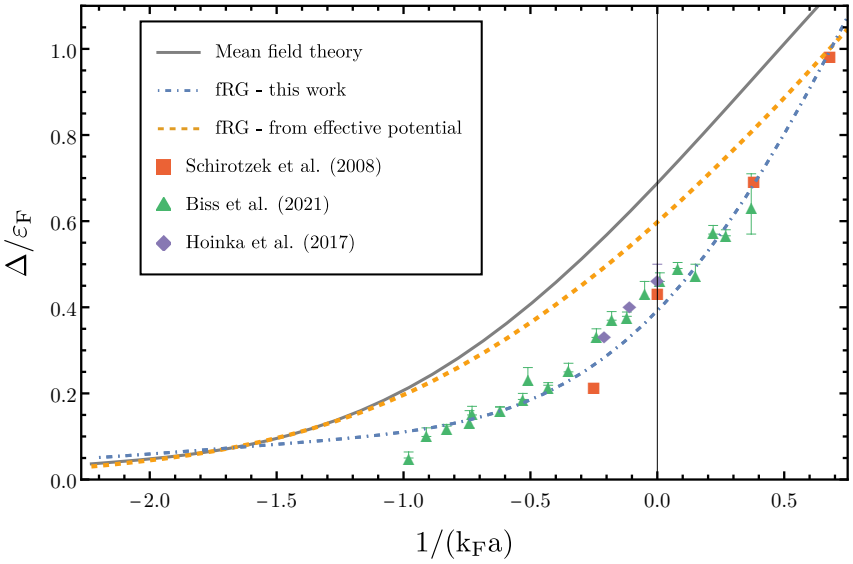

Figure 7.5: Comparison of the gap iteratively calculated (dash-dotted line) with the one obtained from mean-field calculations (solid grey line), effective potential calculations (dashed orange line). In addition, experimental data from the Ketterle group at MIT (Schirotzek et al.) [197], measured in a spin-imbalanced Fermi gas, is shown in red squares, from the Moritz group in Hamburg (Biss et al.) [177] in green triangles and by Hoinka et al. [198] in purple diamonds.

obtained from the effective potential calculation, to the experimental data by the Zwierlein group at MIT [27] and quantum Monte Carlo calculations by [28]. We find promising and very good quantitative agreement at unitarity and on the BEC-side with theory calculations and experimental results. On the BCS-side of the crossover, our iterative result seems to yield smaller results for the equation of state than comparable calculations, although it agrees better with the Fermi liquid theory result. Here, an improved truncation including a running fermion mass m_ψ might lead to increased precision. Furthermore, there is good agreement with various other calculations from quantum Monte Carlo simulations [29, 32], as well as T-matrix [30] and Nozières, Schmitt-Rink [31] studies and measurements [34].

7.4.2 Superfluid gap

The gap is obtained by integrating the susceptibility $n^{(2)}$ from $\mu = 0$ to $\mu = 1$ and at the same time solving for the flow of the gap at $\mu = 1$, i.e. $\Delta(\mu = 1)$. The μ-dependence drops out and the result for the gap at zero temperature over the three-dimensional BCS-BEC crossover is shown in Fig. 7.5, where our curve corresponds to a fit of all data points. For the gap $\Delta/\epsilon_F|_{a\to\infty}$ at unitarity, we obtain

$$\boxed{(\Delta/\epsilon_F)_{\mathrm{fRG}} \simeq 0.39 \qquad \text{for } k_0 = k_{\mathrm{sb}}},$$

Comparison of Bertsch parameter and gap at unitarity		
	μ/ϵ_F	Δ/ϵ_F
fRG - this work	0.362	0.392
fRG - effective potential	0.55	0.60
Literature results		
Astrakharchik et al. [28]	0.42(1)	
Hausmann et al. [206]	0.36	0.46
Bartosch et al. [207]	0.32	0.61
Experimental data		
Ku et al. [27]	0.376(5)	
Schirotzek et al. [197]		0.44
Hoinka et al. [198]		0.47(3)
Biss et al. [177]		0.47(1)

Table 7.1: Comparison of the Bertsch parameter $\xi = \mu/\epsilon_F|_{a\to\infty}$ and the gap $\Delta/\epsilon_F|_{a\to\infty}$ at unitarity for the case of vanishing temperature.

in good agreement with the experimental value of $(\Delta/\epsilon_F)_{\text{exp}} = 0.44$ from [197]. We compare the gap calculated via this iterative procedure to the fRG result obtained from the effective potential calculation and show the gap in mean field theory, experimental data by the Ketterle group at MIT (Schirotzek et al.) [197] (obtained in a spin-imbalanced Fermi gas), by the Moritz group in Hamburg (Biss et al.) [177] and by Hoinka et al. [198] in comparison to the fRG results. We find good quantitative agreement at unitarity and on the BEC-side, especially with data from [197]. In addition, good agreement is found with beyond mean field calculations in [199], other functional integral approaches [33, 200–203], quantum Monte Carlo simulations [204] and measurements in [205]. This constitutes an important result of the present work. It demonstrates that the employed method is very promising in providing quantitatively satisfactory results already with a comparatively small truncation. The results for the equation of state and the gap at zero temperature are summarised in Tab. 7.1.

7.5 Conclusion and outlook

In this Chapter we have put forward an iterative computational approach for the computations of the density, and higher moments of it. The reasoning behind it being that the density requires a cubic fine-tuning procedure in the cutoff. Considering higher moments of the density n, specifically the susceptibility $n^{(2)}$ removes this fine-tuning problem. We obtain improved results for the equation of state and the gap at zero temperature and

thus progress further in our quest to obtain quantitative access to the phase structure of ultracold Fermi gases. Our results are in good quantitative agreement with recent experimental, as well as theoretical data, thus showing that quantitative precision within the promising fRG approach presented here is possible.

Despite of the good quantitative agreement there are a couple of aspects where the current approach can be improved in. As has been shown before, extending the truncation yields enhanced results [59]. Especially, the inclusion of a running fermion propagator, with a renormalised fermion mass m_ψ, is believed to improve the quantitative access to the BCS-side of the BCS-BEC crossover. Furthermore, an extension from the zero to the finite temperature case is needed in order to gain quantitative precision for the superfluid transition temperature T_c/T_F. For this step, the numerical stability in solving the flow equations of the higher moments has to be improved in order to obtain reliable results.

A further upgrade concerns the regulation scheme used in the setup of the flow equations. Here, a cutoff which includes a frequency regulation can further better the outcome, since then the idea of integrating from the ultraviolet to the infrared momentum shell by momentum shell is fully realised.

In the end, it would be beneficial to apply the iterative computational approach shown here also to the case of a system within a dimensional crossover as in Chapter 5. A quantitative precision in this domain would allow for a improved comparison to experiment, as the parameter $L\,k_F$ could directly be mapped to the experimental setup.

Furthermore, it might also be worthwhile to consider the density defined as the integral over the full fermion propagator at $k \to 0$

$$n(\mu, T) = 2 \int_{\vec{p}} \left(\frac{1}{2} - \int_{p_0} G_{\psi^*\psi}(P) \right) .$$

This ansatz might lead, after overcoming some problems concerning the high momentum structure, to comparable results, while requiring less effort on a numerical level.

Overall, our results, especially the quantitative determination of the Bertsch parameter and the superfluid gap at unitarity, constitute significant advancement in the quest for quantitative precision in ultracold Fermi gases, as well as within the fRG approach.

CHAPTER 8

Summary and conclusion

In this thesis we have studied aspects of ultracold Fermi gases from multiple angles. Our focus was on resolving the many-body physics of the strongly correlated regime within the BCS-BEC crossover. This regime is of particular interest since in three dimensions it accommodates the unitary limit, resulting in universal scale invariant behaviour. In a (quasi-) two-dimensional system experimental data suggested a region of increased critical temperature for strong correlations. However, due to these strong interactions perturbative methods are not applicable in this region of the crossover leading us to employ functional methods, specifically the functional renormalisation group (fRG). The fRG, as introduced in Chapter 3, is perfectly suited for this task since it naturally accounts for the relevant degrees of freedom. New developments within this well-established method allow us to gain novel insights into the intricate phase structure and to obtain unprecedented quantitative precision.

One direction we investigated in Chapter 5 was the examination of a confined system of ultracold fermions between three and two dimensions. Here, the confinement was induced by periodic boundary conditions leading to a compactification of the transversal momentum to a torus of circumference L, similar to the Matsubara formalism at finite temperature. We discussed the function space and argued that anti-periodic boundary conditions do not yield a well-defined two-dimensional limit. The dimensional reduction is then realised within the fRG approach by following the RG flow. Following the RG flow essentially suppresses higher momentum modes in the confined direction which decouple and one is left with a system at a specific confinement length. We calculated the zero temperature equation of state and gap over a wide range of confinement lengths for the whole BCS-BEC crossover. At finite temperature the phase diagram within the dimensional crossover was obtained. As in the zero temperature case, for large confinement lengths we found excellent agreement with the three-dimensional system, while for stronger confinements the critical temperature T_c/T_F is lowered leading to a two-dimensional limit.

We observed a non-monotonic behaviour within the dimensional crossover resulting in

regions of increased critical temperature due to a step-like density of states for the confined system, similar to shape resonances in condensed matter systems. Our finite temperature phase diagram at a fixed low confinement exhibits a region of increased critical temperature in the strongly interacting regime which is in good qualitative agreement with experimental data. Our results present new perspectives in understanding confined systems of ultracold quantum gases, as it allows for calculating many-body observables for arbitrary strong confinement. Our results computed from first principles constitute a significant contribution on the study of fluctuation effects on the effective dimensionality. The knowledge of characteristic new features might be utilised in experimental setups and checks for other theoretical methods.

There are, however, two main challenges to overcome to allow for a quantitative comparison to experimental data. First, a confinement induced by a harmonic potential is usually employed in experiments necessitating a function space consisting of Hermite polynomials in theory. Secondly, it is important to match the parameters from experiment to theory. The difficulty here lies in the correct determination of the Fermi momentum k_F in a quantitative manner such that the dimensionless quantity $L\,k_F$ can be matched to the experimentally given ones and a comparison for the given compactification in terms of the Fermi momentum can be made. Obtaining quantitative precision within the dimensional crossover would allow for predicting the specific confinement at which the critical temperature is greatest, thus further advancing towards high-T_c superconductors.

In Chapter 6 we set up a basis for gaining real-time information of ultracold Fermi gases in three spatial dimensions, with the final goal of obtaining transport properties. We analytically continued the flow equations of the two-point functions from imaginary time in Euclidean space to real-time before numerically solving it. The focus was on determining the fermion spectral function over the three-dimensional BCS-BEC crossover at vanishing spatial momenta. Across a specific temperature range in the symmetry broken regime, and from a fermionic to a bosonic system in the strongly interacting regime of the BCS-BEC crossover we found a rather large broadening of the quasiparticle peaks, especially at zero temperature. At low temperatures at unitarity and on the BEC-side of the crossover we obtained a second residual peak with a much smaller spectral weight. Overall, we showed the applicability of the fRG approach to gain real-time properties in in our context of ultracold Fermi gases. Our insights gained here constitute a fertile ground for future advancements, e.g. in calculating the spectral functions at non-vanishing spatial momenta and for the derivation of transport coefficients in ultracold Fermi gases.

Finally, a further promising direction concerns the access to a quantitative description of the physics of ultracold quantum gases within the fRG. We argued in Chapter 7 that this boils down to an insufficiency in the determination of density observables linked to an ultraviolet sensitive behaviour. We overcome this shortcoming by considering the flow of higher moments of the density, i.e. higher derivatives w.r.t. the chemical potential μ. We

found that the second moment of the density, the susceptibility, has an ultraviolet finite behaviour. By starting from the susceptibility we obtain the density by integrating twice over the chemical potential after solving the flow equations of the higher μ-derivatives. Here, we have to take care of the higher μ-derivatives of the couplings as well. We showed the universal applicability of the computational approach and were able to access the zero temperature physics of the three-dimensional BCS-BEC crossover, namely the equation of state and the superfluid gap.

Our results agree well with recent experimental and theoretical data. Especially our quantitative result for the previously hard to determine universal Bertsch parameter of $\xi_{\mathrm{fRG}} = 0.362$ and the gap at unitarity are in excellent agreement with observations. This so far unprecedented quantitative precision within the fRG constitutes a significant advancement in going beyond the qualitative determination of observables. Applying this computational approach to the case of the finite temperature phase diagram in a quantitative manner is one of the next steps.

To conclude, we employed the functional renormalisation group to gain further knowledge in the physics of ultracold Fermi gases in three distinct, but ultimately connected directions. We gained novel physical insights into the interplay of many-body physics and dimensionality, which yielded characteristic new features for confined systems. Secondly, analytical continuation of the flow equations resulted in real-time spectral functions. Finally, the computational procedure laid out in the third part resulted in significant improvement on zero temperature observables in a quantitative manner. With the progress accomplished in this thesis we showed the valuable contribution of the fRG framework in the context of cold quantum gases.

APPENDIX A

Details on the determination of the density in Chapter 7

In this Appendix we comment on further details regarding the density determination via the iterative procedure in Chapter 7.

Comparable to the case of a diverging scattering length $a^{-1} = 0$ in Fig. 7.1 the flow of the second μ-derivative of the density is peaked around the switching scale k_0 for a scattering length of $a = -1$ on the BCS-side of the BCS-BEC crossover. Here, the amplitude of the peak also increases for lower values of the chemical potential μ, as shown in Fig. A.1. In Fig. A.2 a similar behaviour can be observed for a positive scattering length $a = 1$ on the BEC-side of the crossover.

As already mentioned in Section 7.4 the symmetry breaking scale k_{sb} on the BCS-side of the crossover is substantially lower than at unitarity and on the BEC-side. Therefore, we allow for a running of the RG-flow until a final RG-time scale of $t_{\text{final}} = -20$ (for $a < 0$) compared to $t_{\text{final}} = -16$ (for $a \geq 0$). For the ultraviolet cutoff we choose $\Lambda/\sqrt{\mu_{\text{mb}}} = 1000$ consistently.

The integrated second μ-derivative and first μ-derivative of the density, also shown exemplary for $a^{-1} = 0$, are illustrated in Figs. A.3. As described in Section 7.1.2 they are obtained via

$$\partial_\mu^2 \, n_{k=0}(\mu) = \int_\Lambda^0 \frac{dk}{k} \, \partial_\mu^2 \, \dot{n}_k(\mu) + \partial_\mu^2 \, \dot{n}_{k=\Lambda} \, ,$$

for a UV vanishing flow $\partial_\mu^2 \, \dot{n}_{k\to\infty} \to 0$. The first μ-derivative of the density is then given by

$$\partial_\mu \, n_{k=0}(\mu) = \int_0^\mu d\mu' \, \partial_{\mu'}^2 \, n(\mu') + \partial_{\mu'} \, n(0) \, ,$$

with $\partial_\mu \, n(0) = 0$. To both curves the delta contributions of Eq. (7.21) have to be added. Since, we neglect the contributions for S_ϕ and η_ϕ the dominant contribution of the effective potential can be added after solving for the couplings $g_i^{(n)}$. In particular, this results in an integrated second μ-derivative of the density finite at the origin $\mu = 0$.

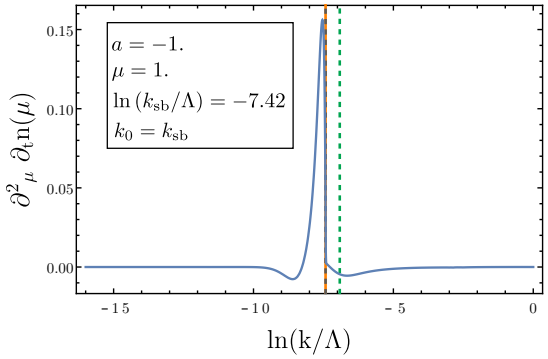

(a) The flow of the second μ-derivative of the density, here exemplary shown for a scattering length of $a = -1$ and $\mu = 1$, is peaked around the switching scale $k_0 = k_{sb}$.

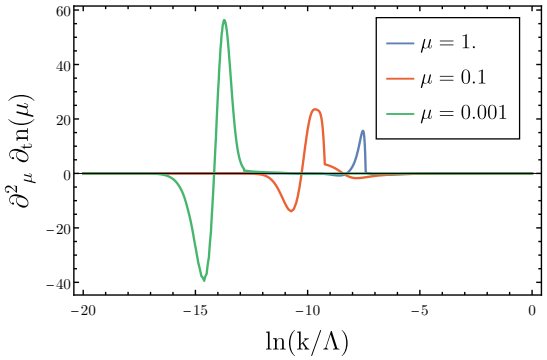

(b) Scaled flow of the second μ-derivative of the density, here exemplary shown for a scattering length of $a = -1$ and different values of $\mu = \{0.001, 0.1, 1.\}$ (shown in green, red and blue from left to right). For better readability we multiplied the curves for $\mu = 1.$ and $\mu = 0.1$ with a factor of 100.

Figure A.1: The flow of the second μ-derivative of the density for a scattering length of $a = -1$.

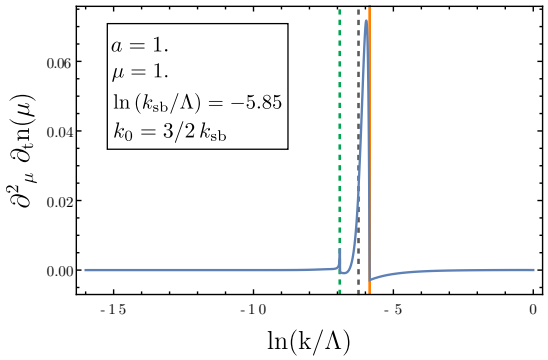

(a) The flow of the second μ-derivative of the density, here exemplary shown for a scattering length of $a = 1$ and $\mu = 1$, is peaked around the switching scale $k_0 = 2/3\, k_{sb}$.

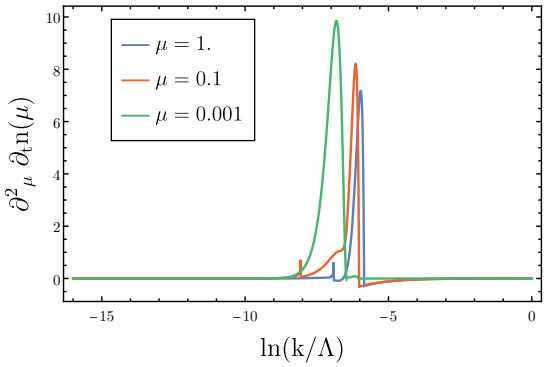

(b) Scaled flow of the second μ-derivative of the density, here exemplary shown for a scattering length of $a = 1$ and different values of $\mu = \{0.001, 0.1, 1.\}$ (shown in green, red and blue from left to right). For better readability we multiplied the curves for $\mu = 1.$ and $\mu = 0.1$ with a factor of 100.

Figure A.2: The flow of the second μ-derivative of the density for a scattering length of $a = 1$.

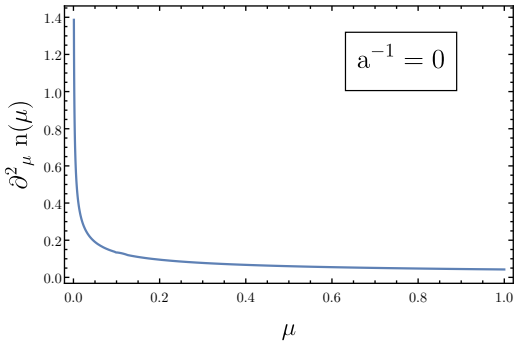

(a) The integrated second μ-derivative of the density, here exemplary shown for a scattering length of $a^{-1} = 0$ and a switching scale $k_0 = k_{\mathrm{sb}}$, before adding the delta contributions.

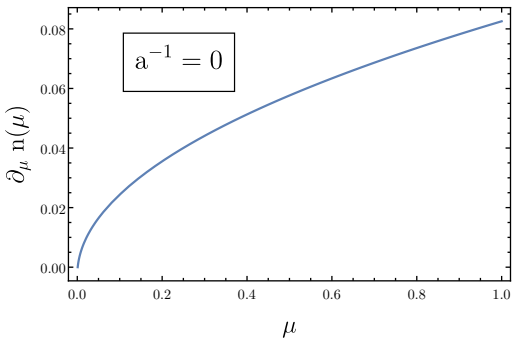

(b) The first μ-derivative of the density, here exemplary shown for a scattering length of $a^{-1} = 0$ and a switching scale $k_0 = k_{\mathrm{sb}}$, before adding the delta contributions.

Figure A.3: Integrated second μ-derivative and first μ-derivative of the density for a scattering length of $a^{-1} = 0$. Both curves do not include corrections due to the delta contributions.

APPENDIX B

Evaluation of delta contributions

In this Appendix we elucidate on the evaluation of the the delta contributions in Section 7.2.2. As outlined there the need for considering contributions proportional to $\sim \delta(k-k_0)$ arises from the splitting of the flow into an ultraviolet and an infrared part

$$R_\psi = R^{\mathrm{UV}}\,\theta^{\mathrm{UV}} + R^{\mathrm{IR}}\,\theta^{\mathrm{IR}}\,, \tag{B.1}$$

and the choice of a hard cutoff $\theta^{\mathrm{UV}} = \theta(k-k_0) = (1-\theta^{\mathrm{IR}})$. The RG-time derivative acting on the Heaviside step functions $\theta^{\mathrm{UV/IR}}$ then leads to the delta functions $\sim \delta(k-k_0)$. The delta contributions can evaluated in a straightforward manner by making use of the 'idempotence' of the Heaviside step function, i.e. $\theta^n(x) \equiv \theta(x)$, thereby rewriting Eq. (B.1) as

$$R_\psi = R^{\mathrm{UV}}\,\left(\theta^{\mathrm{UV}}\right)^2 + R^{\mathrm{IR}}\,\left(\theta^{\mathrm{IR}}\right)^2\,.$$

Repeating the argument outlined in Section 7.2.2 the advantage is that with a splitting of the t-derivative of the regulator leads to a decomposition of the flow equation of the effective potential, and likewise for its derived couplings, as well as $S_\phi = Z_\phi/A_\phi$ and $\eta_\phi = -\dot{A}_\phi/A_\phi$, to wit

$$V^{(\mathrm{F}),\delta} = -2\int_Q \frac{L_\psi^{Q,S,\mathrm{UV}}}{\det{}_F^{Q,\mathrm{UV}}}\,\theta^{\mathrm{UV}}\,R_\psi^{Q,\mathrm{UV}}\,\dot{\theta}^{\mathrm{UV}} + 2\int_Q \frac{L_\psi^{Q,S,\mathrm{IR}}}{\det{}_F^{Q,\mathrm{IR}}}\,\theta^{\mathrm{IR}}\,R_\psi^{Q,\mathrm{IR}}\,\dot{\theta}^{\mathrm{IR}}\,. \tag{B.2}$$

According to Sec. 4.5 Eq. (B.2) and the corresponding equations for $S^{(\mathrm{F}),\delta}$ and $\eta^{(\mathrm{F}),\delta}$ are of the form

$$\begin{aligned}
&\int_{\vec{q}} R_\psi^{Q,\mathrm{UV}}\,\left(L_\psi^{S,\mathrm{UV}}\right)^{2n}\,, && \int_{\vec{q}} R_\psi^{Q,\mathrm{IR}}\,\left(L_\psi^{S,\mathrm{IR}}\right)^{2n}\,,\\
&\int_{\vec{q}} R_\psi^{Q,\mathrm{IR}}\,\left(L_\psi^{S,\mathrm{IR}}\right)^{2n+1}\,, && \frac{1}{d}\int_{\vec{q}} q^2\,R_\psi^{Q,\mathrm{IR}}\,R_\psi^{Q,\mathrm{IR},(2)}\,\left(L_\psi^{S,\mathrm{IR}}\right)^{2n}\,.
\end{aligned} \tag{B.3}$$

The definitions of the symmetrised components $L_\psi^{(S)}$ and of the momentum derivatives of the regulator $R_\psi^{(2)} = \partial^2 R_\psi/\partial(q^2)^2$ follow the definitions in Sec. 4.5 and $n \in \mathbb{N}_0$. The

general form of the contributions in Eq. (B.3) are then be evaluated in a similar fashion as in Appendix E. This yields

$$\begin{aligned}
&\int_{\vec{q}} R_\psi^{Q,\mathrm{UV}} \left(L_\psi^{S,\mathrm{UV}}\right)^{2n} = \frac{16\, v_d}{d\,(d+2)}\, k^{d+2+4n}\, \theta_+\, \tilde{\mu}_+^{d/2+1}\,, \\
&\int_{\vec{q}} R_\psi^{Q,\mathrm{IR}} \left(L_\psi^{S,\mathrm{IR}}\right)^{2n} = \frac{16\, v_d}{d\,(d+2)}\, k^{d+2+4n} \left[\theta_+\, \tilde{\mu}_+^{d/2+1} - \theta_-\, \tilde{\mu}_-^{d/2+1} - (d+2)\, \tilde{\mu}^{d/2}\right], \\
&\int_{\vec{q}} R_\psi^{Q,\mathrm{IR}} \left(L_\psi^{S,\mathrm{IR}}\right)^{2n+1} = \frac{16\, v_d}{d\,(d+2)}\, k^{d+2+2(2n+1)} \left[\theta_+\, \tilde{\mu}_+^{d/2+1} - \theta_-\, \tilde{\mu}_-^{d/2+1} - 2\, \tilde{\mu}^{d/2+1}\right], \\
&\int_{\vec{q}} q^2\, R_\psi^{Q,\mathrm{IR}}\, R_\psi^{Q,\mathrm{IR},(2)} \left(L_\psi^{S,\mathrm{IR}}\right)^{2n} = 0\,.
\end{aligned} \tag{B.4}$$

For better readability we defined $\theta_\pm = \theta(\tilde{\mu}_\pm)$ with $\tilde{\mu}_\pm = \mu/k^2 \pm 1$ in Eq. (B.4).

Note, that in order to perform the integration over the RG-time integration t we recall that for integrands of the form $\delta(k-k_0)\,\theta(k-k_0)$ the integration procedure is only well-defined in terms of distribution theory. As a general rule, one can, for a smeared out Heaviside step function $\theta_\varepsilon(x)$ with $\delta_\varepsilon(x) = \theta'(x)$ and a continuous function f, apply the formula

$$\delta_\varepsilon(x)\, f(x, \theta_\varepsilon(x)) \xrightarrow{\varepsilon\to 0} \delta(x) \int_0^1 \mathrm{d}u\, f(0,u)\,.$$

This results in an overall factor of $\delta(k-k_0)/2$ for the present case of $f(x,u) = u$ and we find for the delta contributions at zero temperature

$$\begin{aligned}
V^{(\delta)} &= -\frac{16\, v_d\, k^{d+2}}{d(d+2)} \left[\theta_-\, \tilde{\mu}_-^{d/2+1} - 2\,\theta(\tilde{\mu})\tilde{\mu}^{d/2+1}\right] \mathcal{F}_1^{T=0}(\sqrt{1+w_3})\, \delta_{k,k_0}\,, \\
S_\phi^{(\delta)} &= \frac{32\, v_d\, h_k^2\, k^{d-4}}{d(d+2)} \left[\theta_-\, \tilde{\mu}_-^{d/2+1} - (d+2)\,\theta(\tilde{\mu})\tilde{\mu}^{d/2}\right] \\
&\qquad \times \left(\mathcal{F}_2^{T=0}(\sqrt{1+w_3}) - 2\, w_3\, \mathcal{F}_3^{T=0}(\sqrt{1+w_3})\right) \delta_{k,k_0}\,, \\
\eta_\phi^{(\delta)} &= 0\,.
\end{aligned} \tag{B.5}$$

Here, we used that the Matsubara sums decouple at zero temperature from the spatial momentum integration.

Alternatively, starting from the RG-time derivative of the regulator split into ultraviolet and infrared part in Eq. (7.12), i.e.

$$\dot{R}_\psi = k\,\partial_k\, R_\psi = \dot{R}^{\mathrm{UV}}\,\theta^{\mathrm{UV}} + \dot{R}^{\mathrm{IR}}\,\theta^{\mathrm{IR}} + k\,\delta_{k,k_0}\left(R^{\mathrm{UV}} - R^{\mathrm{IR}}\right), \tag{B.6}$$

one has to correctly account for the regulator difference $\Delta R := \left(R^{\mathrm{UV}} - R^{\mathrm{IR}}\right)$ in the last term of Eq. (B.6) when performing the integration. In the end, this yields the same result as in Eq. (B.5).

APPENDIX C

Analytically continued flow equations for the fermionic two-point function

In this Appendix we elaborate on further details concerning the calculation of the analytically continued two-point functions for the BCS-BEC crossover. Here, we concentrate on the (inverse) fermion propagator as given in Fig. 4.2. Our aim is to perform the Matsubara summation at finite temperature, cf. Sec. 3.3 for an outline of the Matsubara formalism, as well as the spatial momentum integral analytically and in the end continue the flow equations to real times. This is in general possible, as we use the optimised regulator given in Eq. (4.19) which only regularises the spatial momenta. However, a difficulty arises, since the flow equation for the fermionic two-point function contains mixed diagrams on the right hand side, i.e. with both fermion and boson internal lines. Consequently, there are both fermionic, as well as bosonic Matsubara frequencies present.

Given an external frequency p_0 and according to Eq. (4.23) we have the following type of Matsubara sum for the flow equation of the fermionic two-point function

$$T \sum_{n=-\infty}^{\infty} \frac{f_1(\mathrm{i}\varepsilon_n)}{(\mathrm{i}\varepsilon_n + \mathrm{i}p_0)^2 - y_1^2} \frac{f_2(\mathrm{i}\omega_n)}{(\mathrm{i}\omega_n)^2 - y_2^2}\,, \tag{C.1}$$

with fermionic $\varepsilon_n = (2n+1)\pi T$ and bosonic $\omega_n = 2n\pi T$ Matsubara frequencies. For completeness, in this specific case we have $f_1(\mathrm{i}\varepsilon_n) = \mathrm{i}\varepsilon_n + \mathrm{i}p_0 + k^2 \mathrm{sgn}(q^2 - \mu)$, $f_2(\mathrm{i}\omega_n) = (\mathrm{i}\omega_n + k^2)^2 + k^4\, w_2^2$, $y_1^2 = k^4(1+w_3)$, $y^2 = k^4(1-w_2)$, $w_2 = \rho V''/k^2$ and $w_3 = h^2\rho/k^4$ as before. For non-vanishing $S_\phi = Z_\phi/A_\phi$ or $S_\psi = Z_\psi/A_\psi$, the corresponding Matsubara frequencies can be rescaled accordingly.

Making use of the fact that the fermionic Matsubara frequencies are just shifted versions of the bosonic ones, and vice versa, i.e. with the identifications

$$\begin{aligned} \omega_n &= \varepsilon_n - \pi\, T\,, \\ \varepsilon_n &= \omega_n + \pi\, T\,, \end{aligned} \tag{C.2}$$

the Matsubara sums in Eq. (C.1) can be evaluated in the usual manner. This boils down to applying the residue theorem to Eq. (C.1) and by means of Jordan's lemma expressing

the resulting contour integral as sum over the residues. When taking into account the sum over the fermionic Matsubara frequencies ε_n the bosonic Matsubara frequencies appear shifted according to Eq. (C.2) and vice versa, summing in the end over all contributions.

The spatial momentum integration factors out, as in Appendix E, except for the fermionic contributions proportional to $f_1(\pm y_1 - \mathrm{i}p_0)$ and $f_1(\pm y_2 + \mathrm{i}\pi T)$ which result in additional $\mathrm{sgn}(q^2 - \mu)$-terms. We account for these contributions separately, while using the results of Appendix E for the rest.

In the end, we obtain a symbolic expression for the flow equation of the fermionic two-point function with the loop integration already carried out. It is thus easy to perform the analytical continuation according to Section 6.2 with

$$\partial_t \Gamma_k^{(2),\mathrm{R}}(\omega, \vec{p}) = -\lim_{\epsilon \to 0} \partial_t \Gamma_k^{(2),\mathrm{E}}(p_0 = -\mathrm{i}(\omega + \mathrm{i}\epsilon), \vec{p}) \,,$$

which constitutes the flow equation for real frequencies. As described in Chapter 6 we are then able to solve them numerically in Minkowski space-time.

APPENDIX D

Three- and four-point vertices

For displaying the three- and four-point vertices, we choose supermatrices with BB, BF, FB and FF as indices for further derivatives where a vertical bar, $|$, separates fermionic derivatives acting from the left and right. For an introduction cf. e.g. [115].
The boson vertices in the $\{\overline{\phi_1}, \overline{\phi_2}\}$-basis for a constant bosonic background field $\phi = \sqrt{\rho}$ are given by

$$\bar{\gamma}^{(3)}_{\bar{\phi}_1 BB} = A_\phi^{3/2} \begin{pmatrix} v^{(3)}_{111} & 0 \\ 0 & v^{(3)}_{122} \end{pmatrix}, \qquad \bar{\gamma}^{(3)}_{\bar{\phi}_2 BB} = A_\phi^{3/2} \begin{pmatrix} 0 & v^{(3)}_{122}, \\ v^{(3)}_{122} & 0 \end{pmatrix},$$

$$\bar{\gamma}^{(4)}_{\bar{\phi}_1\bar{\phi}_1 BB} = A_\phi^{2} \begin{pmatrix} v^{(4)}_{1111} & 0 \\ 0 & v^{(4)}_{1122} \end{pmatrix}, \qquad \bar{\gamma}^{(4)}_{\bar{\phi}_1\bar{\phi}_2 BB} = A_\phi^{3/2} \begin{pmatrix} 0 & v^{(4)}_{1122} \\ v^{(4)}_{1122} & 0 \end{pmatrix} = \bar{\gamma}^{(4)}_{\bar{\phi}_2\bar{\phi}_1 BB},$$

$$\bar{\gamma}^{(4)}_{\bar{\phi}_2\bar{\phi}_2 BB} = A_\phi^{2} \begin{pmatrix} v^{(4)}_{1122} & 0 \\ 0 & v^{(4)}_{2222} \end{pmatrix}, \qquad \bar{\gamma}^{(3)}_{\bar{\phi}_1 F|F} = A_\psi\, A_\phi^{1/2}\, \frac{h}{\sqrt{2}} \begin{pmatrix} -\varepsilon & 0 \\ 0 & \varepsilon \end{pmatrix},$$

$$\bar{\gamma}^{(3)}_{\bar{\phi}_2 F|F} = A_\psi\, A_\phi^{1/2}\, \frac{\mathrm{i}\, h}{\sqrt{2}} \begin{pmatrix} \varepsilon & 0 \\ 0 & \varepsilon \end{pmatrix}, \qquad \bar{\gamma}^{(3)}_{\bar{\phi} F|F} = A_\psi\, A_\phi^{1/2}\, h \begin{pmatrix} 0 & 0 \\ 0 & \varepsilon \end{pmatrix},$$

$$\bar{\gamma}^{(3)}_{\bar{\phi}_2^* F|F} = A_\psi\, A_\phi^{1/2}\, h \begin{pmatrix} -\varepsilon & 0 \\ 0 & 0 \end{pmatrix}.$$

For better readabiltiy we introduced the short-hand notations

$$v^{(3)}_{111} = \sqrt{2\,\rho}\, \left(3\, V'' + 2\,\rho\, V^{(3)}\right), \qquad v^{(3)}_{122} = \sqrt{2\,\rho}\, V'',$$

$$v^{(4)}_{1111} = 3\, V'' + 4\,\rho\, \left(3\, V^{(3)} + \rho\, V^{(4)}\right), \qquad v^{(4)}_{1122} = V'' + 2\,\rho\, V^{(3)}, \qquad v^{(4)}_{2222} = 3\, V''.$$

For the mixed vertices we obtain

$$\bar{\gamma}^{(3)}_{\bar{\psi}_1^* B|F} = A_\psi\, A_\phi^{1/2}\, \frac{h}{\sqrt{2}} \begin{pmatrix} 0 & 0 & 0 & 1 \\ 0 & 0 & 0 & \mathrm{i} \end{pmatrix} \overset{\text{conj.}}{\underset{\text{basis}}{=}} A_\psi\, A_\phi^{1/2}\, h \begin{pmatrix} 0 & 0 & 0 & 1 \\ 0 & 0 & 0 & 0 \end{pmatrix},$$

$$\bar{\gamma}^{(3)}_{\bar{\psi}_1 B|F} = A_\psi\, A_\phi^{1/2}\, \frac{h}{\sqrt{2}} \begin{pmatrix} 0 & -1 & 0 & 0 \\ 0 & \mathrm{i} & 0 & 0 \end{pmatrix} \overset{\text{conj.}}{\underset{\text{basis}}{=}} A_\psi\, A_\phi^{1/2}\, h \begin{pmatrix} 0 & 0 & 0 & 0 \\ 0 & -1 & 0 & 0 \end{pmatrix},$$

$$\bar{\gamma}^{(3)}_{BF|\bar{\psi}_1} = A_\psi\, A_\phi^{1/2}\, \frac{h}{\sqrt{2}} \begin{pmatrix} 0 & 1 & 0 & 0 \\ 0 & -\mathrm{i} & 0 & 0 \end{pmatrix} \overset{\text{conj.}}{\underset{\text{basis}}{=}} A_\psi\, A_\phi^{1/2}\, h \begin{pmatrix} 0 & 0 & 0 & 0 \\ 0 & 1 & 0 & 0 \end{pmatrix},$$

$$\bar{\gamma}^{(3)}_{BF|\bar{\psi}_2} = A_\psi\, A_\phi^{1/2}\, \frac{h}{\sqrt{2}} \begin{pmatrix} -1 & 0 & 0 & 0 \\ \mathrm{i} & 0 & 0 & 0 \end{pmatrix} \overset{\text{conj.}}{\underset{\text{basis}}{=}} A_\psi\, A_\phi^{1/2}\, h \begin{pmatrix} 0 & 0 & 0 & 0 \\ -1 & 0 & 0 & 0 \end{pmatrix}$$

and

$$\bar{\gamma}^{(3)}_{F|B\bar{\psi}_1} = A_\psi\, A_\phi^{1/2}\, \frac{h}{\sqrt{2}} \begin{pmatrix} 0 & 0 \\ 1 & -\mathrm{i} \\ 0 & 0 \\ 0 & 0 \end{pmatrix} \overset{\text{conj.}}{\underset{\text{basis}}{=}} A_\psi\, A_\phi^{1/2}\, h \begin{pmatrix} 0 & 0 \\ 0 & 1 \\ 0 & 0 \\ 0 & 0 \end{pmatrix},$$

$$\bar{\gamma}^{(3)}_{F|B\bar{\psi}_2} = A_\psi\, A_\phi^{1/2}\, \frac{h}{\sqrt{2}} \begin{pmatrix} -1 & \mathrm{i} \\ 0 & 0 \\ 0 & 0 \\ 0 & 0 \end{pmatrix} \overset{\text{conj.}}{\underset{\text{basis}}{=}} A_\psi\, A_\phi^{1/2}\, h \begin{pmatrix} 0 & -1 \\ 0 & 0 \\ 0 & 0 \\ 0 & 0 \end{pmatrix},$$

$$\bar{\gamma}^{(3)}_{\bar{\psi}_1^* | FB} = A_\psi\, A_\phi^{1/2}\, \frac{h}{\sqrt{2}} \begin{pmatrix} 0 & 0 \\ 0 & 0 \\ 0 & 0 \\ 1 & \mathrm{i} \end{pmatrix} \overset{\text{conj.}}{\underset{\text{basis}}{=}} A_\psi\, A_\phi^{1/2}\, h \begin{pmatrix} 0 & 0 \\ 0 & 0 \\ 0 & 0 \\ 1 & 0 \end{pmatrix},$$

$$\bar{\gamma}^{(3)}_{\bar{\psi}_1 | FB} = A_\psi\, A_\phi^{1/2}\, \frac{h}{\sqrt{2}} \begin{pmatrix} 0 & 0 \\ -1 & \mathrm{i} \\ 0 & 0 \\ 0 & 0 \end{pmatrix} \overset{\text{conj.}}{\underset{\text{basis}}{=}} A_\psi\, A_\phi^{1/2}\, h \begin{pmatrix} 0 & 0 \\ 0 & -1 \\ 0 & 0 \\ 0 & 0 \end{pmatrix},$$

in the $\{\phi_1, \phi_2\}$ and conjugate field basis $\{\phi, \phi^*\}$, respectively.
The purely bosonic vertices may moreover be written in the conjugate field basis according to

$$\hat{\bar{\gamma}}^{(3)}_{\bar{\phi}_i BB} = U\, \bar{\gamma}^{(3)}_{\bar{\phi}_i BB}\, U^t\,, \quad \hat{\bar{\gamma}}^{(4)}_{\bar{\phi}_i \bar{\phi}_j BB} = U\, \bar{\gamma}^{(3)}_{\bar{\phi}_i \bar{\phi}_j BB}\, U^t\,,$$

and we eventually arrive at

$$\widehat{\bar{\gamma}}^{(3)}_{\bar{\phi}_1 BB} = A_\phi^{3/2} \begin{pmatrix} v^{(3)}_{1\phi\phi} & v^{(3)}_{1\phi\phi^*} \\ v^{(3)}_{1\phi\phi^*} & v^{(3)}_{1\phi\phi} \end{pmatrix}, \qquad \widehat{\bar{\gamma}}^{(3)}_{\bar{\phi}_2 BB} = A_\phi^{3/2} \begin{pmatrix} v^{(3)}_{2\phi\phi} & 0 \\ 0 & -v^{(3)}_{2\phi\phi} \end{pmatrix},$$

$$\widehat{\bar{\gamma}}^{(4)}_{\bar{\phi}_1\bar{\phi}_1 BB} = A_\phi^{2} \begin{pmatrix} v^{(4)}_{11\phi\phi} & v^{(4)}_{11\phi\phi^*} \\ v^{(4)}_{11\phi\phi^*} & v^{(4)}_{11\phi\phi} \end{pmatrix}, \qquad \widehat{\bar{\gamma}}^{(4)}_{\bar{\phi}_1\bar{\phi}_2 BB} = A_\phi^{2} \begin{pmatrix} v^{(4)}_{12\phi\phi} & 0 \\ 0 & -v^{(4)}_{12\phi\phi} \end{pmatrix},$$

$$\widehat{\bar{\gamma}}^{(4)}_{\bar{\phi}_2\bar{\phi}_2 BB} = A_\phi^{2} \begin{pmatrix} v^{(4)}_{22\phi\phi} & v^{(4)}_{22\phi\phi^*} \\ v^{(4)}_{22\phi\phi^*} & v^{(4)}_{22\phi\phi} \end{pmatrix}.$$

The matrix components are defined as

$$v^{(3)}_{1\phi\phi} = \sqrt{2\,\rho}\,\left(V'' + \rho\,V^{(3)}\right), \qquad v^{(3)}_{1\phi\phi^*} = \sqrt{2\,\rho}\,\left(2\,V'' + \rho\,V^{(3)}\right),$$

$$v^{(3)}_{2\phi\phi} = -\mathrm{i}\,\sqrt{2\,\rho}\,V'', \qquad v^{(4)}_{11\phi\phi} = \left(V'' + \rho\,\left(5\,V^{(3)} + 2\,\rho\,V^{(4)}\right)\right),$$

$$v^{(4)}_{11\phi\phi^*} = \left(2\,V'' + \rho\,\left(7\,V^{(3)} + 2\,\rho\,V^{(4)}\right)\right), \qquad v^{(4)}_{12\phi\phi} = -\mathrm{i}\,\left(V'' + 2\,\rho\,V^{(3)}\right),$$

$$v^{(4)}_{22\phi\phi} = -\left(V'' - \rho\,V^{(3)}\right), \qquad v^{(4)}_{22\phi\phi^*} = \left(2\,V'' + \rho\,V^{(3)}\right).$$

APPENDIX E

Loop integration in the derivation of the flow equations

In this Appendix we perform the loop integrations still present for (4.33) and (4.35) in the derivation of the flow equations in Section 4.5. For this we use the Matsubara formalism outlined in Section 3.3 for the summation over the discrete Matsubara frequencies at finite temperature, different for fermions and bosons. The spatial momentum integration follows where the fermionic regularisation around the Fermi surface has to be taken special care of.

E.1 Fermionic Matsubara sums

For fermionic Matsubara sums we find

$$\begin{aligned}
\mathcal{F}_1(z) &= T\sum_{\varepsilon_n}\frac{1}{\varepsilon_n^2+z^2} = \frac{1}{z}\left(\frac{1}{2}-\tilde{N}_F(z)\right),\\
\mathcal{F}_2(z) &= T\sum_{\varepsilon_n}\frac{1}{(\varepsilon_n^2+z^2)^2} = -\frac{\partial}{\partial z^2}\mathcal{F}_1(z) = -\frac{1}{2\,z}\frac{\partial}{\partial\, z}\mathcal{F}_1(z)\\
&= \frac{1}{2\,z^3}\left(\frac{1}{2}-\tilde{N}_F(z)+z\,\tilde{N}_F'(z)\right),\\
\mathcal{F}_3(z) &= T\sum_{\varepsilon_n}\frac{1}{(\varepsilon_n^2+z^2)^3} = -\frac{1}{2}\frac{\partial}{\partial z^2}\mathcal{F}_2(z) = -\frac{1}{4\,z}\frac{\partial}{\partial\, z}\mathcal{F}_2(z)\\
&= \frac{3}{8\,z^5}\left(\frac{1}{2}-\tilde{N}_F(z)+z\,\tilde{N}_F'(z)-\frac{z^2}{3}\,\tilde{N}_F''(z)\right).
\end{aligned} \tag{E.1}$$

where the Fermi-Dirac distribution with the renormalised temperature $\tilde{T}=T/k^2$ is defined as

$$\tilde{N}_F(z) = \begin{cases} 0 & \tilde{T}=0 \\ \left(e^{z/\tilde{T}}+1\right)^{-1} & \tilde{T}>0 \end{cases}. \tag{E.2}$$

To simplify the non-thermal beta-function we set $\tilde{N}_F = 0$, while the limit $T \to 0$ with $N_F(z) \to \theta(-z)$ yields the same result.

E.2 Bosonic Matsubara sums

Without the quadratic frequency term the bosonic Matsubara sums yield

$$\begin{aligned}
\mathcal{B}_1(z) &= T \sum_{\omega_n} \frac{1}{\omega_n^2 + z^2} = \frac{1}{z} \left(\frac{1}{2} + \tilde{N}_B(z) \right) , \\
\mathcal{B}_2(z) &= T \sum_{\omega_n} \frac{1}{(\omega_n^2 + z^2)^2} = -\frac{\partial}{\partial z^2} \mathcal{B}_1(z) = -\frac{1}{2\,z} \frac{\partial}{\partial\, z} \mathcal{B}_1(z) \\
&= \frac{1}{2\,z^3} \left(\frac{1}{2} + \tilde{N}_B(z) - z\, \tilde{N}_F'(z) \right) , \\
\mathcal{B}_3(z) &= T \sum_{\omega_n} \frac{1}{(\omega_n^2 + z^2)^3} = -\frac{1}{2} \frac{\partial}{\partial z^2} \mathcal{B}_2(z) = -\frac{1}{4\,z} \frac{\partial}{\partial\, z} \mathcal{B}_2(z) \\
&= \frac{3}{8\,z^5} \left(\frac{1}{2} + \tilde{N}_B(z) - z\, \tilde{N}_B'(z) + \frac{z^2}{3}\, \tilde{N}_B''(z) \right) .
\end{aligned} \tag{E.3}$$

with the Bose-Einstein distribution

$$\tilde{N}_B(z) = \begin{cases} 0 & \tilde{T} = 0 \\ \left(e^{z/\tilde{T}} - 1 \right)^{-1} & \tilde{T} > 0 \end{cases} .$$

Including a quadratic dependence on q_0 in the boson propagator, i.e. for a non-vanishing $W_\phi \neq 0$ in Eq. (4.4), modifies the bosonic Matsubara sums slightly, but is otherwise straightforward to take into account.

E.3 Fermionic momentum integration

In order to perform the momentum integration for both fermions, as well as bosons, we exploit the specific structure of the optimised regulator such that it becomes particularly simple due to the overall Heaviside-Theta-function.
The optimised fermionic regulator is given by

$$\begin{aligned}
\overline{R}_\psi(q^2) &= A_\psi\, k^2\, r_\psi(z) , \\
\frac{\dot{\overline{R}}_\psi(q^2)}{A_\psi} &= -\eta_\psi\, R_\psi + \dot{R}_\psi , \quad \dot{R}_\psi(q^2) = 2\, k^2\, \mathrm{sgn}(z)\, \theta\left(1 - |z|\right) ,
\end{aligned}$$

where $z = (q^2 - \mu)/k^2$ and

$$\begin{aligned} r_\psi(z) &= (\mathrm{sgn}(z) - z)\ \theta\left(1 - |z|\right)\,, \\ r'_\psi(z) &= -\theta\left(1 - |z|\right)\,, \\ r''_\psi(z) &= \mathrm{sgn}(z)\,\delta\left(1 - |z|\right). \end{aligned}$$

We furthermore have $R^{(2)}_\psi(q^2) = r''_\psi(z)/k^2$. Due to the overall $\overline{R}_\psi$ in the integral we effectively have

$$L^S_\psi(Q) = q^2 - \mu + R_\psi(q^2) \overset{\text{eff.}}{=} k^2\,\mathrm{sgn}(z).$$

Then for $n \in \mathbf{N}_0$ we find the evaluated momentum integrals

$$\begin{aligned} \int_{\vec{q}} \frac{\dot{\overline{R}}_\psi}{A_\psi}\ \left(L^S_\psi\right)^{2n} &= \frac{8\,v_d}{d}\,k^{d+4n+2}\left[\ell_2(\tilde{\mu}) - \eta_\psi\,\left(\ell_2(\tilde{\mu}) - \frac{1}{d+2}\,\tilde{\ell}_1(\tilde{\mu})\right)\right]\,, \\ \int_{\vec{q}} \frac{\dot{\overline{R}}_\psi}{A_\psi}\ \left(L^S_\psi\right)^{2n+1} &= \frac{8\,v_d}{d}\,k^{d+4n+4}\left[\ell_1(\tilde{\mu}) - \eta_\psi\,\left(\ell_1(\tilde{\mu}) - \frac{1}{d+2}\,\tilde{\ell}_2(\tilde{\mu})\right)\right]\,, \\ \int_{\vec{q}} \frac{\dot{\overline{R}}_\psi}{A_\psi}\,q^2\,x^2\,r''_\psi(z)\ \left(L^S_\psi\right)^{2n} &= \frac{2\,v_d}{2}\,k^{4+4n+d}\,\ell_3(\tilde{\mu})\,, \\ \int_{\vec{q}} \frac{\dot{\overline{R}}_\psi}{A_\psi}\,q^2\,x^2\,r''_\psi(z)\ \left(L^S_\psi\right)^{2n+1} &= \frac{2\,v_d}{2}\,k^{6+4n+d}\,\ell_1(\tilde{\mu})\,. \end{aligned} \tag{E.4}$$

Here we defined the threshold functions

$$\begin{aligned} \ell_1(x) &= \theta(x+1)\,(x+1)^{d/2} - \theta(x-1)\,(x-1)^{d/2}\,, \\ \ell_2(x) &= \theta(x+1)\,(x+1)^{d/2} + \theta(x-1)\,(x-1)^{d/2} - 2\,\theta(x)\,x^{d/2}\,, \\ \ell_3(x) &= \theta(x+1)\,(x+1)^{d/2} + \theta(x-1)\,(x-1)^{d/2}\,, \\ \tilde{\ell}_1(x) &= \theta(x+1)\,(x+1)^{d/2}\,(d-2\,x) - \theta(x-1)\,(x-1)^{d/2}\ (d+2\,x)\,, \\ \tilde{\ell}_2(x) &= \theta(x+1)\,(x+1)^{d/2}\,(d-2\,x) + \theta(x-1)\,(x-1)^{d/2}\ (d+2\,x) - 4\,\theta(x)\,x^{d/2+1} \end{aligned} \tag{E.5}$$

and the d-dimensional volume integrals

$$v_d = \frac{1}{2^{d+1}\,\pi^{d/2}\,\Gamma(d/2)}\,, \quad v_1 = \frac{1}{4\,\pi}\,, \quad v_2 = \frac{1}{8\,\pi}\,, \quad v_3 = \frac{1}{8\,\pi^2}\,.$$

Note that the terms proportional to $\sim \eta_\psi$ in Eq. (E.4) vanish for our truncation, cf. Eq. (4.18), but are given for a straightforward extension in future works.

E.4 Bosonic momentum integration

In accordance with the discussion of the fermionic momentum integration the optimised bosonic regulator is given by

$$\begin{aligned}
\overline{R}_\phi(q^2) &= A_\phi\, k^2\, r_\phi(y)\,, \\
\frac{\dot{\overline{R}}_\phi(q^2)}{A_\phi} &= -\eta_\phi\, R_\phi + \dot{R}_\phi\,, \quad \dot{R}_\phi(q^2) = 2\,k^2\;\theta\,(1-y)\;,
\end{aligned}$$

where $y = q^2/2k^2$ and

$$\begin{aligned}
r_\phi(y) &= (1-y)\;\theta\,(1-y)\;, \\
r'_\phi(y) &= -\,\theta\,(1-y)\;, \\
r''_\phi(y) &= \;\delta\,(1-y)\;.
\end{aligned}$$

We furthermore have $R^{(2)}_\psi(q^2) = r''_\phi(y)/4k^2$. Due to the overall $\overline{R}_\phi$ in the integral we effectively find

$$L^S_\phi(Q) = \frac{q^2}{2} + V' + \rho\, V'' + R_\phi(q^2) \overset{\text{eff.}}{=} k^2 + V' + \rho\, V''. \tag{E.6}$$

Hence, we obtain the simple result

$$\begin{aligned}
\int_{\vec{q}} \frac{\dot{\overline{R}}_\phi}{A_\phi} &= 8\,\frac{2^{d/2}\,v_d}{d}\,k^{d+2}\,\left(1 - \frac{\eta_\phi}{d+2}\right)\,, \\
\int_{\vec{q}} \frac{\dot{\overline{R}}_\phi}{A_\phi}\,q^2\,x^2\,R^{(2)}_\phi(q^2) &= \frac{2^{d/2}\,v_d}{d}\,k^{d+2}.
\end{aligned}$$

Due to (E.6) every insertion of $\left(L_\phi)^S\right)^n$ under the integral yields another factor of $k^2 + V' + \rho\, V'' = k^2\;(1 + w_1 + w_2)$ for the linear frequency dependence in our case.

APPENDIX F

Finite volume summation

In this Appendix we calculate the explicit form of the 'spatial Matsubara sums' for the flow equations restricted to finite volume in Section 4.6. As we have argued in Section 4.6 the confinement w.r.t. periodic boundary conditions results in a quantisation of the momentum in the confined 'transversal' directions. We then modify the optimised regulators accordingly

$$R_{\phi,k}(q^2) = \left(k^2 - \frac{q^2 + k_n^2}{2}\right) \theta\left(k^2 - \frac{q^2 + k_n^2}{2}\right) ,$$
$$R_{\psi,k}(q^2) = k^2 \left[\operatorname{sgn}\left(z + \tilde{k}_n^2\right) - \left(z + \tilde{k}_n^2\right)\right] \theta\left(1 - |z + \tilde{k}_n^2|\right) ,$$

where we again used $z = (q^2 - \mu)/k^2$ and $\tilde{k}_n = k_n/k$. Hence the d-dimensional spatial integration splits up into a sum over the discrete momenta k_n and a momentum integral in $d-1$ dimensions

$$\int \frac{d^d q}{(2\pi)^d} = \frac{1}{L} \sum_{k_n} \int \frac{d^{d-1} q}{(2\pi)^{d-1}} .$$

Due to the inclusion of the discrete momenta in the regulator the evaluation of the spatial boils down to counting the modes within the potential well. For periodic boundary conditions we hereby encounter the following type of sums

$$\sum_{n=-N}^{N} \alpha = \alpha\,(1 + 2\,N) \qquad (\alpha \in \mathbb{R}) ,$$

$$\sum_{n=1}^{N} n^2 = \frac{1}{6}\,N\,(1+N)\,(1+2\,N) ,$$

and

$$\sum_{n=1}^{N} n^4 = \frac{1}{30}\,N\,(1+N)\,(1+2\,N)\,(-1+3\,N+3\,N^2) .$$

As a result of the periodic boundary conditions the regulator function restricts the Matsubara-type summation in the transversal direction to $|k_n| = |2\pi n/L| < \sqrt{2}\,k$ or equivalently $|n| < \tilde{L}/\sqrt{2}\pi$.

For bosonic contributions we define

$$N^{(B)} = \left\lfloor \frac{\tilde{L}}{\sqrt{2}\,\pi} \right\rfloor$$

with $\lfloor x \rfloor$ being the largest integer smaller than x. In three dimensions we find

$$\begin{aligned} C_L =& \frac{1}{L} \sum_{k_n} \left(1 - \frac{k_n^2}{2\,k^2}\right)^{d/2} \left(1 - \frac{\eta_\phi}{d+2}\left(1 - \frac{k_n^2}{2\,k^2}\right)\right) \theta\left(k^2 - \frac{k_n^2}{2}\right) \\ =& \frac{k}{\tilde{L}} \left(1 + 2\,N^{(B)}\right) \left[1 - \frac{\eta_\phi}{4} - \frac{1}{6}\left(1 - \frac{\eta\phi}{2}\right)\left(\frac{2\,\pi}{\tilde{L}}\right)^2 N^{(B)}\left(1 + N^{(B)}\right)\right. \\ & \left. - \frac{\eta_\phi}{60}\left(\frac{2\,\pi}{\tilde{L}}\right)^4 N^{(B)}\left(1 + N^{(B)}\right)\left(-1 + 3\,N^{(B)} + 3\left(N^{(B)}\right)^2\right)\right]. \end{aligned}$$

The fermionic momentum integrals can be generalised by the transformation $z \to \widehat{z} = (q^2 + k_n^2 - \mu)/k^2$. All results can then be transferred by the transformation $\mu \to \widehat{\mu} = \tilde{\mu} - k_n^2$. For periodic boundary conditions it can be easily shown in three spatial dimensions

$$\frac{1}{L}\sum_{k_n} \theta\left(\hat{\mu}+1\right)\left(\hat{\mu}+1\right)^{(d-1)/2} = \frac{1}{L}\left[\tilde{\mu}_+\left(1 + 2N_1^{(F)}\right) - \frac{1}{3}\left(\frac{2\pi}{\tilde{L}}\right)^2 N_1^{(F)}\left(1 + N_1^{(F)}\right)\left(1 + 2N_1^{(F)}\right)\right]\theta_+\,,$$

$$\frac{1}{L}\sum_{k_n} \theta\left(\hat{\mu}-1\right)\left(\hat{\mu}-1\right)^{(d-1)/2} = \frac{1}{L}\left[\tilde{\mu}_-\left(1 + 2N_2^{(F)}\right) - \frac{1}{3}\left(\frac{2\pi}{\tilde{L}}\right)^2 N_2^{(F)}\left(1 + N_2^{(F)}\right)\left(1 + 2N_2^{(F)}\right)\right]\theta_-\,,$$

$$\frac{1}{L}\sum_{k_n} \theta\left(\hat{\mu}\right)\left(\hat{\mu}\right)^{(d-1)/2} = \frac{1}{L}\left[\tilde{\mu}\left(1 + 2N_3^{(F)}\right) - \frac{1}{3}\left(\frac{2\pi}{\tilde{L}}\right)^2 N_3^{(F)}\left(1 + N_3^{(F)}\right)\left(1 + 2N_3^{(F)}\right)\right]\theta\left(\tilde{\mu}\right)\,.$$

For a more compact notation we defined $\theta_\pm = \theta(\tilde{\mu}_\pm)$ with $\tilde{\mu}_\pm = \mu/k^2 \pm 1$ and used

$$N_1^{(F)} = \left\lfloor \frac{\tilde{L}\,(\tilde{\mu}+1)^{1/2}}{2\,\pi} \right\rfloor, \qquad N_2^{(F)} = \left\lfloor \frac{\tilde{L}\,(\tilde{\mu}-1)^{1/2}}{2\,\pi} \right\rfloor, \qquad N_3^{(F)} = \left\lfloor \frac{\tilde{L}\,\tilde{\mu}^{1/2}}{2\,\pi} \right\rfloor.$$

Hence for the spatial threshold function with explicit Matsubara summation we obtain for periodic boundary conditions in $d = 3$

$$\begin{aligned} \frac{1}{L}\sum_{k_n} \ell_a(\hat{\mu}) =& \frac{k}{\tilde{L}} \left\{ \left[(\tilde{\mu}+1)\left(1 + 2\,N_1^{(F)}\right) - \frac{1}{3}\left(\frac{2\,\pi}{\tilde{L}}\right)^2 N_1^{(F)}\left(1 + N_1^{(F)}\right)\left(1 + 2\,N_1^{(F)}\right)\right]\right. \\ & (-1)^a \left[(\tilde{\mu}+1) \to (\tilde{\mu}-1)\,\&\left(N_1^{(F)} \to N_2^{(F)}\right)\right] \\ & \left. - \left(1 + (-1)^a\right)\left[\tilde{\mu}\left(1 + 2\,N_3^{(F)}\right) - \frac{1}{3}\left(\frac{2\,\pi}{\tilde{L}}\right)^2 N_3^{(F)}\left(1 + N_3^{(F)}\right)\left(1 + 2\,N_3^{(F)}\right)\right]\right\}, \end{aligned}$$

for $a = 1, 2$. Furthermore, we find

$$\frac{1}{L}\sum_{k_n} \ell_3(\hat{\mu}) = \frac{k}{\tilde{L}} \left\{ \left[(\tilde{\mu}+1) \left(1 + 2\, N_1^{(F)}\right) - \frac{1}{3} \left(\frac{2\,\pi}{\tilde{L}}\right)^2 N_1^{(F)} \left(1 + N_1^{(F)}\right) \left(1 + 2\, N_1^{(F)}\right) \right] \right.$$
$$\left. + \left[(\tilde{\mu}+1) \to (\tilde{\mu}-1) \,\&\, \left(N_1^{(F)} \to N_2^{(F)}\right) \right] \right\} .$$

With these generalisations of the flow equations from Section 4.5.2 to finite volume represents the base for our investigation of the dimensional crossover from three to two dimensions in Chapter 5. We will solve the flow equations, after an appropriate vacuum renormalisation, numerically as described in Section 4.7.

Acknowledgements

During my work on this thesis there were many people who supported me in multiple ways and I am grateful to all of them. Naturally, this list cannot be exhaustive.

First of all, I want to thank my supervisor Jan M. Pawlowski. This work would not have been possible without your constant support and guidance. Your astonishing physical insight helped me in various challenging situations which came up during this time and shaped my approach to physical problems. Furthermore, I appreciated the welcoming atmosphere within your group.

I am grateful to Prof. Dr. Tilman Enss for being my second referee and the insightful discussions in our meetings.

Moreover, I thank Felipe Attanasio, Marc Bauer, Gioele Casagranda, Keisuke Fujii for our discussions on different theory perspectives on ultracold quantum gases which we had together with Tilman Enss and Jan M. Pawlowski.

I would like to express my gratitude to Christof Wetterich for being my second supervisor and the stimulating and versatile discussions we had.

I thank Selim Jochim and his group at the Physikalisches Institut Heidelberg, in particular Luca Bayha, for various discussions on possible comparisons between experiment and theory and to the good collaboration we had. Moreover, I thank their group for providing experimental data to us.

I am grateful to Igor Boettcher for stimulating and lively discussions and that he shared his physical insight into the physics of cold atoms with me. In addition, I thank Stefan Flörchinger, Masatoshi Yamada and Sören Lammers for helpful comments and their ideas on solving problems within quantum systems.

Furthermore, I thank Eleonora Lippi, Robert Ott and Tina Kuka for their great team spirit in organising the Young Researchers' Convent, especially the workshop on Quantum Computing, and the pleasant time spent together.

I thank Markus Heller, Jan Horak, Julian Urban, Nicolas Wink and Felix Ziegler for the joint effort in the organisation of the Cold Quantum Coffee seminar at the institute.

I thank all people in the group of Jan M. Pawlowski, for the diverse discussions during lunch time, coffee breaks and the various barbecues in the evening. Special thanks goes to the whole Dachzimmer during my stay for the enjoyable time spent together.

I am indebted to Anton Cyrol, Markus Heller, Lukas Kades and Robert Ott for critically reading parts my thesis and their support during this time.

Lastly, for their unconditional support, their open ears and the joyful moments spent together I thank my family, all my friends and my girlfriend.

Bibliography

[1] B. M. Faigle-Cedzich, J. M. Pawlowski, and C. Wetterich, "Dimensional crossover in ultracold Fermi gases from functional renormalization," Phys. Rev. A 103, 033320 (2021), arXiv:1910.07365 [cond-mat.quant-gas].

[2] B. M. Faigle-Cedzich and J. M. Pawlowski, "Spectral function of ultracold Fermi gases from functional renormalisation," (2022), in preparation.

[3] B. M. Faigle-Cedzich and J. M. Pawlowski, "Towards quantitative precision in ultracold atoms with functional renormalisation," (2022).

[4] S. Bose, "Plancks Gesetz und Lichtquantenhypothese," Zeitschrift für Physik 26, 178 (1924).

[5] A. Einstein, "Quantentheorie des einatomigen idealen Gases," Sitzber. Kgl. Preuss. Akad. Wiss. 261 (1924).

[6] P. Kapitza, "Viscosity of Liquid Helium below the λ-Point," Nature Physics 141, 74 (1938).

[7] J. F. Allen and A. D. Misener, "Flow of Liquid Helium II," Nature Physics 141, 75 (1938).

[8] H. Kammerlingh Onnes, "The superconductivity of mercury," Comm. Phys. Lab. Univ. Leiden 122, 122 (1911).

[9] J. Bardeen, L. N. Cooper, and J. R. Schrieffer, "Theory of Superconductivity," Phys. Rev. 108, 1175 (1957).

[10] M. H. Anderson, J. R. Ensher, M. R. Matthews, C. E. Wieman, and E. A. Cornell, "Observation of Bose-Einstein Condensation in a Dilute Atomic Vapor," Science 269, 198 (1995), https://www.science.org/doi/pdf/10.1126/science.269.5221.198.

[11] C. C. Bradley, C. A. Sackett, J. J. Tollett, and R. G. Hulet, "Evidence of Bose-Einstein Condensation in an Atomic Gas with Attractive Interactions," Phys. Rev. Lett. 75, 1687 (1995).

[12] K. B. Davis, M. O. Mewes, M. R. Andrews, N. J. van Druten, D. S. Durfee, D. M. Kurn, and W. Ketterle, "Bose-Einstein Condensation in a Gas of Sodium Atoms," Phys. Rev. Lett. 75, 3969 (1995).

[13] B. DeMarco and D. S. Jin, "Onset of Fermi Degeneracy in a Trapped Atomic Gas," Science 285, 1703 (1999), https://www.science.org/doi/pdf/10.1126/science.285.5434.1703.

[14] F. Schreck, L. Khaykovich, K. L. Corwin, G. Ferrari, T. Bourdel, J. Cubizolles, and C. Salomon, "Quasipure Bose-Einstein Condensate Immersed in a Fermi Sea," Phys. Rev. Lett. 87, 080403 (2001).

[15] A. G. Truscott, K. E. Strecker, W. I. McAlexander, G. B. Partridge, and R. G. Hulet, "Observation of Fermi Pressure in a Gas of Trapped Atoms," Science 291, 2570 (2001), https://www.science.org/doi/pdf/10.1126/science.1059318.

[16] C. Monroe, W. Swann, H. Robinson, and C. Wieman, "Very cold trapped atoms in a vapor cell," Phys. Rev. Lett. 65, 1571 (1990).

[17] E. L. Raab, M. Prentiss, A. Cable, S. Chu, and D. E. Pritchard, "Trapping of Neutral Sodium Atoms with Radiation Pressure," Phys. Rev. Lett. 59, 2631 (1987).

[18] N. Masuhara, J. M. Doyle, J. C. Sandberg, D. Kleppner, T. J. Greytak, H. F. Hess, and G. P. Kochanski, "Evaporative Cooling of Spin-Polarized Atomic Hydrogen," Phys. Rev. Lett. 61, 935 (1988).

[19] P. S. Jessen, C. Gerz, P. D. Lett, W. D. Phillips, S. L. Rolston, R. J. C. Spreeuw, and C. I. Westbrook, "Observation of quantized motion of Rb atoms in an optical field," Phys. Rev. Lett. 69, 49 (1992).

[20] D. Jaksch and P. Zoller, "The cold atom Hubbard toolbox," Annals of Physics 315, 52 (2005), arXiv:cond-mat/0410614 [cond-mat.other].

[21] M. Lewenstein, A. Sanpera, V. Ahufinger, B. Damski, A. Sen, and U. Sen, "Ultracold atomic gases in optical lattices: mimicking condensed matter physics and beyond," Advances in Physics 56, 243 (2007), arXiv:cond-mat/0606771 [cond-mat.other].

[22] D. M. Eagles, "Possible Pairing without Superconductivity at Low Carrier Concentrations in Bulk and Thin-Film Superconducting Semiconductors," Phys. Rev. 186, 456 (1969).

[23] A. J. Leggett, "Diatomic molecules and cooper pairs," in *Modern Trends in the Theory of Condensed Matter*, edited by Pękalski, Andrzej and Przystawa, Jerzy A. (Springer Berlin Heidelberg, Berlin, Heidelberg, 1980) pp. 13–27.

[24] S. Gandolfi, A. Gezerlis, and J. Carlson, "Neutron Matter from Low to High Density," Annual Review of Nuclear and Particle Science 65, 303–328 (2015).

[25] G. A. Baker, "Neutron matter model," Phys. Rev. C 60, 054311 (1999).

[26] H. Heiselberg, "Fermi systems with long scattering lengths," Phys. Rev. A 63, 043606 (2001).

[27] M. J. H. Ku, A. T. Sommer, L. W. Cheuk, and M. W. Zwierlein, "Revealing the Superfluid Lambda Transition in the Universal Thermodynamics of a Unitary Fermi Gas," Science 335, 563 (2012), https://science.sciencemag.org/content/335/6068/563.full.pdf.

[28] G. E. Astrakharchik, J. Boronat, J. Casulleras, Giorgini, and S., "Equation of State of a Fermi Gas in the BEC-BCS Crossover: A Quantum Monte Carlo Study," Physical Review Letters 93 (2004), 10.1103/physrevlett.93.200404.

[29] S. Y. Chang, V. R. Pandharipande, J. Carlson, and K. E. Schmidt, "Quantum Monte Carlo studies of superfluid Fermi gases," Physical Review A 70 (2004), 10.1103/physreva.70.043602.

[30] P. Pieri, L. Pisani, and G. C. Strinati, "Comparison between a diagrammatic theory for the BCS-BEC crossover and quantum Monte Carlo results," Physical Review B 72 (2005), 10.1103/physrevb.72.012506.

[31] H. Hu, X.-J. Liu, and P. D. Drummond, "Equation of state of a superfluid Fermi gas in the BCS-BEC crossover," Europhysics Letters (EPL) 74, 574–580 (2006).

[32] S. Pilati and S. Giorgini, "Phase Separation in a Polarized Fermi Gas at Zero Temperature," Physical Review Letters 100 (2008), 10.1103/physrevlett.100.030401.

[33] R. Haussmann, M. Punk, and W. Zwerger, "Spectral functions and rf response of ultracold fermionic atoms," Physical Review A 80 (2009), 10.1103/physreva.80.063612.

[34] N. Navon, S. Nascimbene, F. Chevy, and C. Salomon, "The Equation of State of a Low-Temperature Fermi Gas with Tunable Interactions," Science 328, 729–732 (2010).

[35] C. Wetterich, "Exact evolution equation for the effective potential," Phys. Lett. B301, 90 (1993), arXiv:1710.05815 [hep-th].

[36] J. M. Pawlowski, "Aspects of the functional renormalisation group," Annals Phys. 322, 2831 (2007), arXiv:hep-th/0512261 [hep-th].

[37] B.-J. Schaefer and J. Wambach, "Renormalization group approach towards the QCD phase diagram," Phys. Part. Nucl. 39, 1025 (2008), arXiv:hep-ph/0611191 [hep-ph].

[38] H. Gies, "Introduction to the functional RG and applications to gauge theories," Lect. Notes Phys. 852, 287 (2012), arXiv:hep-ph/0611146 [hep-ph].

[39] B. Delamotte, "An Introduction to the nonperturbative renormalization group," Lect. Notes Phys. 852, 49 (2012), arXiv:cond-mat/0702365 [cond-mat.stat-mech].

[40] P. Kopietz, L. Bartosch, and F. Schütz, "Introduction to the functional renormalization group," Lect. Notes Phys. 798, 1 (2010).

[41] W. Metzner, M. Salmhofer, C. Honerkamp, V. Meden, and K. Schonhammer, "Functional renormalization group approach to correlated fermion systems," Rev. Mod. Phys. 84, 299 (2012), arXiv:1105.5289 [cond-mat.str-el].

[42] J. Braun, "Fermion Interactions and Universal Behavior in Strongly Interacting Theories," J. Phys. G39, 033001 (2012), arXiv:1108.4449 [hep-ph].

[43] I. Boettcher, J. M. Pawlowski, and S. Diehl, "Ultracold atoms and the Functional Renormalization Group," Nucl. Phys. Proc. Suppl. 228, 63 (2012), arXiv:1204.4394 [cond-mat.quant-gas].

[44] N. Dupuis, L. Canet, A. Eichhorn, W. Metzner, J. M. Pawlowski, M. Tissier, and N. Wschebor, "The nonperturbative functional renormalization group and its applications," Phys. Rept. (2021), 10.1016/j.physrep.2021.01.001, arXiv:2006.04853 [cond-mat.stat-mech].

[45] M. C. Birse, B. Krippa, J. A. McGovern, and N. R. Walet, "Pairing in many-fermion systems: an exact renormalisation group treatment," Physics Letters B 605, 287 (2005), arXiv:hep-ph/0406249 [hep-ph].

[46] S. Diehl and C. Wetterich, "Universality in phase transitions for ultracold fermionic atoms," Phys. Rev. A73, 033615 (2006), arXiv:cond-mat/0502534 [cond-mat.supr-con].

[47] S. Diehl and C. Wetterich, "Functional integral for ultracold fermionic atoms," Nucl. Phys. B770, 206 (2007), arXiv:cond-mat/0510407 [cond-mat.supr-con].

[48] S. Diehl, H. Gies, J. M. Pawlowski, and C. Wetterich, "Renormalisation flow and universality for ultracold fermionic atoms," Phys. Rev. A76, 053627 (2007), arXiv:cond-mat/0703366 [COND-MAT].

[49] S. Diehl, H. Gies, J. M. Pawlowski, and C. Wetterich, "Flow equations for the BCS-BEC crossover," Phys. Rev. A76, 021602 (2007), arXiv:cond-mat/0701198 [cond-mat].

[50] S. Floerchinger, M. Scherer, S. Diehl, and C. Wetterich, "Particle-hole fluctuations in the BCS-BEC Crossover," Phys. Rev. B78, 174528 (2008), arXiv:0808.0150 [cond-mat.supr-con].

[51] S. Floerchinger, R. Schmidt, S. Moroz, and C. Wetterich, "Functional renormalization for trion formation in ultracold fermion gases," Phys. Rev. A79, 013603 (2009), arXiv:0809.1675 [cond-mat.supr-con].

[52] S. Floerchinger, M. M. Scherer, and C. Wetterich, "Modified Fermi-sphere, pairing gap and critical temperature for the BCS-BEC crossover," Phys. Rev. A81, 063619 (2010), arXiv:0912.4050 [cond-mat.quant-gas].

[53] S. Diehl, S. Floerchinger, H. Gies, J. M. Pawlowski, and C. Wetterich, "Functional renormalization group approach to the BCS-BEC crossover," Annalen Phys. 522, 615 (2010), arXiv:0907.2193 [cond-mat.quant-gas].

[54] I. Boettcher, S. Diehl, J. M. Pawlowski, and C. Wetterich, "Tan contact and universal high momentum behavior of the fermion propagator in the BCS-BEC crossover," Phys. Rev. A87, 023606 (2013), arXiv:1209.5641 [cond-mat.quant-gas].

[55] D. Schnoerr, I. Boettcher, J. M. Pawlowski, and C. Wetterich, "Error estimates and specification parameters for functional renormalization," Annals Phys. 334, 83 (2013), arXiv:1301.4169 [cond-mat.quant-gas].

[56] I. Boettcher, J. Braun, T. K. Herbst, J. M. Pawlowski, D. Roscher, and C. Wetterich, "Phase structure of spin-imbalanced unitary Fermi gases," Phys. Rev. A91, 013610 (2015), arXiv:1409.5070 [cond-mat.quant-gas].

[57] D. Roscher, J. Braun, and J. E. Drut, "Phase structure of mass- and spin-imbalanced unitary Fermi gases," Phys. Rev. A91, 053611 (2015), arXiv:1501.05544 [cond-mat.quant-gas].

[58] I. Boettcher, T. K. Herbst, J. M. Pawlowski, N. Strodthoff, L. von Smekal, and C. Wetterich, "Sarma phase in relativistic and non-relativistic systems," Physics Letters B 742, 86 (2015), arXiv:1409.5232 [cond-mat.quant-gas].

[59] I. Boettcher, J. M. Pawlowski, and C. Wetterich, "Critical temperature and superfluid gap of the unitary Fermi gas from functional renormalization," Phys. Rev. A 89, 053630 (2014).

[60] M. M. Scherer, S. Floerchinger, and H. Gies, "Functional renormalization for the BCS-BEC crossover," Phil. Trans. Roy. Soc. Lond. A368, 2779 (2011), arXiv:1010.2890 [cond-mat.quant-gas].

[61] M. Lewenstein, A. Sanpera, V. Ahufinger, B. Damski, A. Sen, and U. Sen, "Ultracold atomic gases in optical lattices: mimicking condensed matter physics and beyond," Advances in Physics 56, 243 (2007), arXiv:cond-mat/0606771 [cond-mat.other].

[62] I. Bloch, J. Dalibard, and W. Zwerger, "Many-body physics with ultracold gases," Rev. Mod. Phys. 80, 885 (2008), arXiv:0704.3011 [cond-mat.other].

[63] I. Boettcher, L. Bayha, D. Kedar, P. A. Murthy, M. Neidig, M. G. Ries, A. N. Wenz, G. Zürn, S. Jochim, and T. Enss, "Equation of State of Ultracold Fermions in the 2D BEC-BCS Crossover Region," Phys. Rev. Lett. 116, 045303 (2016), arXiv:1509.03610 [cond-mat.quant-gas].

[64] M. Holten, L. Bayha, A. C. Klein, P. A. Murthy, P. M. Preiss, and S. Jochim, "Anomalous Breaking of Scale Invariance in a Two-Dimensional Fermi Gas," Phys. Rev. Lett. 121, 120401 (2018), arXiv:1803.08879 [cond-mat.quant-gas].

[65] U. Toniolo, B. C. Mulkerin, X.-J. Liu, and H. Hu, "Breathing-mode frequency of a strongly interacting Fermi gas across the two- to three-dimensional crossover," Phys. Rev. A 97, 063622 (2018), arXiv:1803.07714 [cond-mat.quant-gas].

[66] S. Tung, G. Lamporesi, D. Lobser, L. Xia, and E. A. Cornell, "Observation of the Presuperfluid Regime in a Two-Dimensional Bose Gas," Phys. Rev. Lett. 105, 230408 (2010).

[67] M. G. Ries, A. N. Wenz, G. Zürn, L. Bayha, I. Boettcher, D. Kedar, P. A. Murthy, M. Neidig, T. Lompe, and S. Jochim, "Observation of Pair Condensation in the Quasi-2D BEC-BCS Crossover," Phys. Rev. Lett. 114, 230401 (2015).

[68] K. Fenech, P. Dyke, T. Peppler, M. G. Lingham, S. Hoinka, H. Hu, and C. J. Vale, "Thermodynamics of an Attractive 2D Fermi Gas," Phys. Rev. Lett. 116, 045302 (2016), arXiv:1508.04502 [cond-mat.quant-gas].

[69] T. Plisson, B. Allard, M. Holzmann, G. Salomon, A. Aspect, P. Bouyer, and T. Bourdel, "Coherence properties of a two-dimensional trapped Bose gas around the superfluid transition," Phys. Rev. A 84, 061606 (2011), arXiv:1110.3201 [physics.atom-ph].

[70] P. A. Murthy, M. Neidig, R. Klemt, L. Bayha, I. Boettcher, T. Enss, M. Holten, G. Zürn, P. M. Preiss, and S. Jochim, "High-temperature pairing in a strongly interacting two-dimensional Fermi gas," Science 359, 452 (2018), arXiv:1705.10577 [cond-mat.quant-gas].

[71] B. C. Mulkerin, X.-J. Liu, and H. Hu, "Collective modes of a two-dimensional Fermi gas at finite temperature," Phys. Rev. A 97, 053612 (2018), arXiv:1708.06978 [cond-mat.quant-gas].

[72] Z. Hadzibabic, P. Krüger, M. Cheneau, B. Battelier, and J. Dalibard, "Berezinskii–Kosterlitz–Thouless crossover in a trapped atomic gas," Nature 441, 1118 (2006).

[73] P. Cladé, C. Ryu, A. Ramanathan, K. Helmerson, and W. D. Phillips, "Observation of a 2D Bose Gas: From Thermal to Quasicondensate to Superfluid," Phys. Rev. Lett. 102, 170401 (2009), arXiv:0805.3519 [cond-mat.other].

[74] R. Desbuquois, L. Chomaz, T. Yefsah, J. Léonard, J. Beugnon, C. Weitenberg, and J. Dalibard, "Superfluid behaviour of a two-dimensional Bose gas," Nature Physics 8, 645 (2012), arXiv:1205.4536 [cond-mat.quant-gas].

[75] R. J. Fletcher, M. Robert-de-Saint-Vincent, J. Man, N. Navon, R. P. Smith, K. G. H. Viebahn, and Z. Hadzibabic, "Connecting Berezinskii-Kosterlitz-Thouless and BEC Phase Transitions by Tuning Interactions in a Trapped Gas," Phys. Rev. Lett. 114, 255302 (2015), arXiv:1501.02262 [cond-mat.quant-gas].

[76] P. A. Murthy, I. Boettcher, L. Bayha, M. Holzmann, D. Kedar, M. Neidig, M. G. Ries, A. N. Wenz, G. Zürn, and S. Jochim, "Observation of the Berezinskii-Kosterlitz-Thouless Phase Transition in an Ultracold Fermi Gas," Phys. Rev. Lett. 115, 010401 (2015), arXiv:1505.02123 [cond-mat.quant-gas].

[77] L. P. Pitaevskii and A. Rosch, "Breathing modes and hidden symmetry of trapped atoms in two dimensions," Phys. Rev. A 55, R853 (1997), arXiv:cond-mat/9608135 [cond-mat].

[78] M. Olshanii, H. Perrin, and V. Lorent, "Example of a Quantum Anomaly in the Physics of Ultracold Gases," Phys. Rev. Lett. 105, 095302 (2010), arXiv:1006.1072 [cond-mat.quant-gas].

[79] E. Taylor and M. Randeria, "Apparent Low-Energy Scale Invariance in Two-Dimensional Fermi Gases," Phys. Rev. Lett. 109, 135301 (2012), arXiv:1205.1525 [cond-mat.quant-gas].

[80] J. Hofmann, "Quantum anomaly, universal relations and breathing mode of a two-dimensional Fermi gas," Phys. Rev. Lett. 108, 185303 (2012), arXiv:1112.1384 [cond-mat.quant-gas].

[81] C. Gao and Z. Yu, "Breathing mode of two-dimensional atomic Fermi gases in harmonic traps," Phys. Rev. A 86, 043609 (2012), arXiv:1208.5640 [cond-mat.quant-gas].

[82] C. Chafin and T. Schäfer, "Scale breaking and fluid dynamics in a dilute two-dimensional Fermi gas," Phys. Rev. A 88, 043636 (2013), arXiv:1308.2004 [cond-mat.quant-gas].

[83] W. Daza, J. E. Drut, C. Lin, and C. Ordóñez, "Virial expansion for the Tan contact and Beth-Uhlenbeck formula from two-dimensional SO(2,1) anomalies," Phys. Rev. A 97, 033630 (2018), arXiv:1801.08086 [cond-mat.quant-gas].

[84] H. Hu, B. C. Mulkerin, U. Toniolo, L. He, and X.-J. Liu, "Reduced Quantum Anomaly in a Quasi-Two-Dimensional Fermi Superfluid: Significance of the Confinement-Induced Effective Range of Interactions," Phys. Rev. Lett. 122, 070401 (2019), arXiv:1806.04383 [cond-mat.quant-gas].

[85] T. Peppler, P. Dyke, M. Zamorano, I. Herrera, S. Hoinka, and C. J. Vale, "Quantum Anomaly and 2D-3D Crossover in Strongly Interacting Fermi Gases," Phys. Rev. Lett. 121, 120402 (2018), arXiv:1804.05102 [cond-mat.quant-gas].

[86] P. A. Murthy, N. Defenu, L. Bayha, M. Holten, P. M. Preiss, T. Enss, and S. Jochim, "Quantum scale anomaly and spatial coherence in a 2D Fermi superfluid," Science 365, 268 (2019), arXiv:1805.04734 [cond-mat.quant-gas].

[87] X. Barillier-Pertuisel, S. Pittel, L. Pollet, and P. Schuck, "Boson-fermion pairing in Bose-Fermi mixtures on one-dimensional optical lattices," Phys. Rev. A 77, 012115 (2008), arXiv:0706.2133 [cond-mat.other].

[88] C. Ufrecht, M. Meister, A. Roura, and W. P. Schleich, "Comprehensive classification for Bose–Fermi mixtures," New Journal of Physics 19, 085001 (2017).

[89] B. Zhu, S. Häfner, B. Tran, M. Gerken, J. Ulmanis, E. Tiemann, and M. Weidemüller, "High partial-wave Feshbach resonances in an ultracold ^{6}Li-^{133}Cs mixture," arXiv e-prints , arXiv:1912.01264 (2019), arXiv:1912.01264 [cond-mat.quant-gas].

[90] L. He and P. Zhuang, "Phase diagram of a cold polarized Fermi gas in two dimensions," Physical Review A 78 (2008), 10.1103/physreva.78.033613.

[91] K. Sun and C. J. Bolech, "Oscillatory pairing amplitude and magnetic compressible-incompressible transitions in imbalanced fermionic superfluids in optical lattices of elongated tubes," Phys. Rev. A 85, 051607 (2012), arXiv:1112.1622 [cond-mat.quant-gas].

[92] W. Ong, C. Cheng, I. Arakelyan, and J. E. Thomas, "Spin-Imbalanced Quasi-Two-Dimensional Fermi Gases," Phys. Rev. Lett. 114, 110403 (2015).

[93] D. Mitra, P. T. Brown, P. Schauß, S. S. Kondov, and W. S. Bakr, "Phase Separation and Pair Condensation in a Spin-Imbalanced 2D Fermi Gas," Phys. Rev. Lett. 117, 093601 (2016), arXiv:1604.01479 [cond-mat.quant-gas].

[94] C.-T. Wu, R. Boyack, and K. Levin, "Two-dimensional spin-imbalanced Fermi gases at nonzero temperature: Phase separation of a noncondensate," Phys. Rev. A 94, 033604 (2016), arXiv:1605.01479 [cond-mat.quant-gas].

[95] S. Dutta and E. J. Mueller, "Dimensional crossover in a spin-imbalanced Fermi gas," Phys. Rev. A 94, 063627 (2016), arXiv:1508.03352 [cond-mat.quant-gas].

[96] L. Chomaz, I. Ferrier-Barbut, F. Ferlaino, B. Laburthe-Tolra, B. L. Lev, and T. Pfau, "Dipolar physics: A review of experiments with magnetic quantum gases," arXiv e-prints , arXiv:2201.02672 (2022), arXiv:2201.02672 [cond-mat.quant-gas].

[97] J. Bjerlin, S. M. Reimann, and G. M. Bruun, "Few-Body Precursor of the Higgs Mode in a Fermi Gas," Phys. Rev. Lett. 116, 155302 (2016).

[98] L. Bayha, M. Holten, R. Klemt, K. Subramanian, J. Bjerlin, S. M. Reimann, G. M. Bruun, P. M. Preiss, and S. Jochim, "Observing the emergence of a quantum phase transition shell by shell," Nature 587, 583 (2020), arXiv:2004.14761 [cond-mat.quant-gas].

[99] A. Mil, T. V. Zache, A. Hegde, A. Xia, R. P. Bhatt, M. K. Oberthaler, P. Hauke, J. Berges, and F. Jendrzejewski, "A scalable realization of local U(1) gauge invariance in cold atomic mixtures," Science 367, 1128 (2020), arXiv:1909.07641 [cond-mat.quant-gas].

[100] C. Schweizer, F. Grusdt, M. Berngruber, L. Barbiero, E. Demler, N. Goldman, I. Bloch, and M. Aidelsburger, "Floquet approach to &Z;$_2$ lattice gauge theories with ultracold atoms in optical lattices," Nature Physics 15, 1168 (2019), arXiv:1901.07103 [cond-mat.quant-gas].

[101] F. Görg, K. Sandholzer, J. Minguzzi, R. Desbuquois, M. Messer, and T. Esslinger, "Realization of density-dependent peierls phases to engineer quantized gauge fields coupled to ultracold matter," Nature Physics 15, 1 (2019).

[102] J. C. Halimeh, R. Ott, I. P. McCulloch, B. Yang, and P. Hauke, "Robustness of gauge-invariant dynamics against defects in ultracold-atom gauge theories," Phys. Rev. Res. 2, 033361 (2020), arXiv:2005.10249 [cond-mat.quant-gas].

[103] Z.-Y. Zhou, G.-X. Su, J. C. Halimeh, R. Ott, H. Sun, P. Hauke, B. Yang, Z.-S. Yuan, J. Berges, and J.-W. Pan, "Thermalization dynamics of a gauge theory on a quantum simulator," arXiv e-prints , arXiv:2107.13563 (2021), arXiv:2107.13563 [cond-mat.quant-gas].

[104] H. T. C. Stoof, D. B. M. Dickerscheid, and K. Gubbels, *Ultracold Quantum Fields*, 1st ed. (Springer, 2009).

[105] A. Altland and B. D. Simons, *Condensed Matter Field Theory*, 2nd ed. (Cambridge University Press, 2010).

[106] W. Zwerger, ed., *The BCS-BEC Crossover and the Unitary Fermi Gas* (Springer Berlin Heidelberg, Berlin, Heidelberg, 2012).

[107] J. Levinsen and M. M. Parish, "Strongly interacting two-dimensional Fermi gases," (2014), 10.1142/9789814667746_0001, arXiv:1408.2737 [cond-mat.quant-gas].

[108] J. Dalibard, "Collisional dynamics of ultracold atomic gases," (2002).

[109] C. Chin, R. Grimm, P. Julienne, and E. Tiesinga, "Feshbach resonances in ultracold gases," Reviews of Modern Physics 82, 1225 (2010), arXiv:0812.1496 [cond-mat.other].

[110] N. D. Mermin and H. Wagner, "Absence of Ferromagnetism or Antiferromagnetism in One- or Two-Dimensional Isotropic Heisenberg Models," Phys. Rev. Lett. 17, 1133 (1966).

[111] P. C. Hohenberg, "Existence of Long-Range Order in One and Two Dimensions," Phys. Rev. 158, 383 (1967).

[112] J. M. Pawlowski, J. A. Bonnet, S. Rechenberger, M. Reichert, and N. Wink, "-The functional renormalization group- & applications to gauge theories and gravity," In preparation.

[113] A. Das, *Finite Temperature Field Theory* (WORLD SCIENTIFIC, 1997) https://www.worldscientific.com/doi/pdf/10.1142/3277.

[114] J. Zinn-Justin, "Quantum Field Theory at Finite Temperature: An Introduction," (2000).

[115] J. Zinn-Justin, *Quantum Field Theory and Critical Phenomena; 4th ed.*, International series of monographs on physics (Clarendon Press, Oxford, 2002).

[116] J. I. Kapusta and C. Gale, *Finite-Temperature Field Theory: Principles and Applications*, 2nd ed., Cambridge Monographs on Mathematical Physics (Cambridge University Press, 2006).

[117] S. Lammers, I. Boettcher, and C. Wetterich, "Dimensional crossover of nonrelativistic bosons," Physical Review A 93, 063631 (2016), arXiv:1603.02409 [cond-mat.quant-gas].

[118] D. F. Litim, "Mind the Gap," International Journal of Modern Physics A 16, 2081 (2001), arXiv:hep-th/0104221 [hep-th].

[119] D. F. Litim, "Optimized renormalization group flows," Phys. Rev. D64, 105007 (2001), arXiv:hep-th/0103195 [hep-th].

[120] C. Wetterich, "Functional renormalization for quantum phase transitions with non-relativistic bosons," Phys. Rev. B 77, 064504 (2008).

[121] N. Defenu, A. Trombettoni, I. Nándori, and T. Enss, "Nonperturbative renormalization group treatment of amplitude fluctuations for $|\varphi|^4$ topological phase transitions," Phys. Rev. B 96, 174505 (2017), arXiv:1706.00618 [cond-mat.quant-gas].

[122] A. M. Fischer and M. M. Parish, "BCS-BEC crossover in a quasi-two-dimensional Fermi gas," Phys. Rev. A 88, 023612 (2013).

[123] A. M. Fischer and M. M. Parish, "Quasi-two-dimensional Fermi gases at finite temperatures," Phys. Rev. B 90, 214503 (2014).

[124] J. Braun, S. Diehl, and M. M. Scherer, "Finite-size and particle-number effects in an ultracold Fermi gas at unitarity," Phys. Rev. A 84, 063616 (2011).

[125] M. Bauer, M. M. Parish, and T. Enss, "Universal Equation of State and Pseudogap in the Two-Dimensional Fermi Gas," Phys. Rev. Lett. 112, 135302 (2014), arXiv:1311.1000 [cond-mat.quant-gas].

[126] H. Shi, S. Chiesa, and S. Zhang, "Ground-state properties of strongly interacting Fermi gases in two dimensions," Phys. Rev. A 92, 033603 (2015).

[127] F. Marsiglio, P. Pieri, A. Perali, F. Palestini, and G. C. Strinati, "Pairing effects in the normal phase of a two-dimensional Fermi gas," Phys. Rev. B 91, 054509 (2015), arXiv:1406.7761 [cond-mat.quant-gas].

[128] C.-T. Wu, B. M. Anderson, R. Boyack, and K. Levin, "Quasicondensation in Two-Dimensional Fermi Gases," Physical Review Letters 115 (2015), 10.1103/physrevlett.115.240401.

[129] L. He, H. Lü, G. Cao, H. Hu, and X.-J. Liu, "Quantum fluctuations in the BCS-BEC crossover of two-dimensional Fermi gases," Physical Review A 92 (2015), 10.1103/physreva.92.023620.

[130] G. Bighin and L. Salasnich, "Finite-temperature quantum fluctuations in two-dimensional Fermi superfluids," Phys. Rev. B 93, 014519 (2016), arXiv:1507.07542 [cond-mat.quant-gas].

[131] L. Salasnich and G. Bighin, "Quantum Fluctuations and Vortex-Antivortex Unbinding in the 2D Bcs-Bec Crossover," Journal of Superconductivity and Novel Magnetism 29, 3103–3106 (2016).

[132] B. C. Mulkerin, L. He, P. Dyke, C. J. Vale, X.-J. Liu, and H. Hu, "Superfluid density and critical velocity near the Berezinskii-Kosterlitz-Thouless transition in

a two-dimensional strongly interacting Fermi gas," Physical Review A 96 (2017), 10.1103/physreva.96.053608.

[133] G. Bighin and L. Salasnich, "Renormalization of the superfluid density in the two-dimensional BCS-BEC crossover," International Journal of Modern Physics B 32, 1840022 (2018), arXiv:1710.11171 [cond-mat.quant-gas].

[134] F. Wu, J. Hu, L. He, X.-J. Liu, and H. Hu, "Effective theory for ultracold strongly interacting fermionic atoms in two dimensions," Physical Review A 101 (2020), 10.1103/physreva.101.043607.

[135] J. P. Gaebler, J. T. Stewart, T. E. Drake, D. S. Jin, A. Perali, P. Pieri, and G. C. Strinati, "Observation of pseudogap behaviour in a strongly interacting Fermi gas," Nature Physics 6, 569 (2010), arXiv:1003.1147 [cond-mat.quant-gas].

[136] S. Tsuchiya, R. Watanabe, and Y. Ohashi, "Single-particle properties and pseudogap effects in the BCS-BEC crossover regime of an ultracold Fermi gas above T_c," Phys. Rev. A 80, 033613 (2009), arXiv:0907.4595 [cond-mat.quant-gas].

[137] M. Matsumoto, R. Hanai, D. Inotani, and Y. Ohashi, "Pairing fluctuations in a strongly interacting two-dimensional Fermi gas," Journal of Physics: Conference Series 969, 012012 (2018).

[138] A. Richie-Halford, J. E. Drut, and A. Bulgac, "Emergence of a pseudogap in the BCS-BEC crossover," Phys. Rev. Lett. 125, 060403 (2020), arXiv:2004.05014 [cond-mat.quant-gas].

[139] Y. Chen, A. Shanenko, A. Perali, and F. Peeters, "Superconducting nanofilms: Molecule-like pairing induced by quantum confinement," Journal of physics. Condensed matter : an Institute of Physics journal 24, 185701 (2012).

[140] A. Guidini and A. Perali, "Band-edge BCS-BEC crossover in a two-band superconductor: physical properties and detection parameters," Superconductor Science Technology 27, 124002 (2014), arXiv:1407.3109 [cond-mat.supr-con].

[141] A. Guidini, L. Flammia, M. V. Milošević, and A. Perali, "BCS-BEC Crossover in Quantum Confined Superconductors," Journal of Superconductivity and Novel Magnetism 29 (2016), 10.1007/s10948-015-3308-y, 1512.06759 [cond-mat.supr-con].

[142] H. Tajima, A. Perali, and P. Pieri, "BCS-BEC Crossover and Pairing Fluctuations in a Two Band Superfluid/Superconductor: A T Matrix Approach," Condensed Matter 5 (2020), 10.3390/condmat5010010.

[143] S. Rinott, K. B. Chashka, A. Ribak, E. D. L. Rienks, A. Taleb-Ibrahimi, P. Le Fevre, F. Bertran, M. Randeria, and A. Kanigel, "Tuning across the BCS-BEC crossover

in the multiband superconductor Fe1+ySexTe1-x: An angle-resolved photoemission study," Science Advances 3 (2017), 10.1126/sciadv.1602372.

[144] J. M. Blatt and C. J. Thompson, "Shape Resonances in Superconducting Thin Films," Phys. Rev. Lett. 10, 332 (1963).

[145] C. Thompson and J. Blatt, "Shape resonances in superconductors - II simplified theory," Physics Letters 5, 6 (1963).

[146] D. Innocenti, N. Poccia, A. Ricci, A. Valletta, S. Caprara, A. Perali, and A. Bianconi, "Resonant and crossover phenomena in a multiband superconductor: Tuning the chemical potential near a band edge," Phys. Rev. B 82, 184528 (2010), arXiv:1007.0510 [cond-mat.supr-con].

[147] A. Bianconi, D. Innocenti, A. Valletta, and A. Perali, "Shape Resonances in superconducting gaps in a 2DEG at oxide- oxide interface," in *Journal of Physics Conference Series*, Journal of Physics Conference Series, Vol. 529 (2014) p. 012007, arXiv:1312.6669 [cond-mat.supr-con].

[148] N. Pinto, S. J. Rezvani, A. Perali, L. Flammia, M. V. Milošević, M. Fretto, C. Cassiago, and N. De Leo, "Dimensional crossover and incipient quantum size effects in superconducting niobium nanofilms," Scientific Reports 8, 4710 (2018), arXiv:1710.00265 [cond-mat.supr-con].

[149] D. Eom, S. Qin, M.-Y. Chou, and C. K. Shih, "Persistent Superconductivity in Ultrathin Pb Films: A Scanning Tunneling Spectroscopy Study," Phys. Rev. Lett. 96, 027005 (2006).

[150] A. Perali, A. Bianconi, A. Lanzara, and N. L. Saini, "The gap amplification at a shape resonance in a superlattice of quantum stripes: A mechanism for high T_c," Solid State Communications 100, 181 (1996), arXiv:1107.3292 [cond-mat.supr-con].

[151] N. Tetradis and C. Wetterich, "The high temperature phase transition for phi**4 theories," Nucl. Phys. B398, 659 (1993).

[152] V. L. Berezinsky, "Destruction of long range order in one-dimensional and two-dimensional systems having a continuous symmetry group. I. Classical systems," Sov. Phys. JETP 32, 493 (1971), [Zh. Eksp. Teor. Fiz.59,907(1971)].

[153] V. L. Berezinsky, "Destruction of Long-range Order in One-dimensional and Two-dimensional Systems Possessing a Continuous Symmetry Group. II. Quantum Systems." Sov. Phys. JETP 34, 610 (1972).

[154] J. M. Kosterlitz and D. J. Thouless, "Ordering, metastability and phase transitions in two-dimensional systems," Journal of Physics C Solid State Physics 6, 1181 (1973).

[155] J. M. Kosterlitz, "The critical properties of the two-dimensional xy model," Journal of Physics C Solid State Physics 7, 1046 (1974).

[156] K. Miyake, "Fermi Liquid Theory of Dilute Submonolayer 3He on Thin 4He II Film: Dimer Bound State and Cooper Pairs," Progress of Theoretical Physics 69, 1794 (1983).

[157] L. P. Gor'kov and T. K. Melik-Barkhudarov, "Contribution to the theory of superconductivity in an imperfect Fermi gas," Sov. Phys. JETP 13, 1018 (1961), [Zh. Eksp. Teor. Fiz. 40, 1452- 1458 (1961)].

[158] D. S. Petrov, M. A. Baranov, and G. V. Shlyapnikov, "Superfluid transition in quasi-two-dimensional Fermi gases," Phys. Rev. A 67, 031601 (2003).

[159] A. A. Shanenko, M. D. Croitoru, A. V. Vagov, V. M. Axt, A. Perali, and F. M. Peeters, "Atypical BCS-BEC crossover induced by quantum-size effects," Phys. Rev. A 86, 033612 (2012), arXiv:1203.3325 [cond-mat.quant-gas].

[160] H. Biss, L. Sobirey, N. Luick, M. Bohlen, J. J. Kinnunen, G. M. Bruun, T. Lompe, and H. Moritz, "Excitation Spectrum and Superfluid Gap of an Ultracold Fermi Gas," Phys. Rev. Lett. 128, 100401 (2022), arXiv:2105.09820 [cond-mat.quant-gas].

[161] M. Jarrell and J. E. Gubernatis, "Bayesian inference and the analytic continuation of imaginary-time quantum Monte Carlo data," Phys. Rept. 269, 133 (1996).

[162] M. Asakawa, Y. Nakahara, and T. Hatsuda, "Maximum entropy analysis of the spectral functions in lattice QCD," Progress in Particle and Nuclear Physics 46, 459 (2001), arXiv:hep-lat/0011040 [hep-lat].

[163] F. Karsch, E. Laermann, P. Petreczky, S. Stickan, and I. Wetzorke, "A lattice calculation of thermal dilepton rates," Physics Letters B 530, 147 (2002), arXiv:hep-lat/0110208 [hep-lat].

[164] S. Datta, F. Karsch, P. Petreczky, and I. Wetzorke, "Behavior of charmonium systems after deconfinement," Phys. Rev. D 69, 094507 (2004), arXiv:hep-lat/0312037 [hep-lat].

[165] H. T. Ding, A. Francis, O. Kaczmarek, F. Karsch, H. Satz, and W. Soeldner, "Charmonium properties in hot quenched lattice QCD," Phys. Rev. D 86, 014509 (2012), arXiv:1204.4945 [hep-lat].

[166] H. J. Vidberg and J. W. Serene, "Solving the Eliashberg equations by means of N-point Padé approximants," Journal of Low Temperature Physics 29, 179 (1977).

[167] N. Dupuis, "Infrared behavior and spectral function of a Bose superfluid at zero temperature," Phys. Rev. A 80, 043627 (2009), arXiv:0907.2779 [cond-mat.quant-gas].

[168] A. Sinner, N. Hasselmann, and P. Kopietz, "Spectral Function and Quasiparticle Damping of Interacting Bosons in Two Dimensions," Phys. Rev. Lett. 102, 120601 (2009), arXiv:0811.0624 [cond-mat.other].

[169] R. Schmidt and T. Enss, "Excitation spectra and rf response near the polaron-to-molecule transition from the functional renormalization group," Phys. Rev. A 83, 063620 (2011), arXiv:1104.1379 [cond-mat.quant-gas].

[170] C. Chin, M. Bartenstein, A. Altmeyer, S. Riedl, S. Jochim, J. H. Denschlag, and R. Grimm, "Observation of the Pairing Gap in a Strongly Interacting Fermi Gas," Science 305, 1128 (2004), arXiv:cond-mat/0405632 [cond-mat.supr-con].

[171] Y. Shin, C. H. Schunck, A. Schirotzek, and W. Ketterle, "Tomographic rf Spectroscopy of a Trapped Fermi Gas at Unitarity," Phys. Rev. Lett. 99, 090403 (2007).

[172] J. T. Stewart, J. P. Gaebler, and D. S. Jin, "Using photoemission spectroscopy to probe a strongly interacting Fermi gas," Nature 454, 744 (2008), arXiv:0805.0026 [cond-mat.other].

[173] T.-L. Dao, A. Georges, J. Dalibard, C. Salomon, and I. Carusotto, "Measuring the One-Particle Excitations of Ultracold Fermionic Atoms by Stimulated Raman Spectroscopy," Phys. Rev. Lett. 98, 240402 (2007).

[174] S. Floerchinger, "Analytic Continuation of Functional Renormalization Group Equations," JHEP 05, 021 (2012), arXiv:1112.4374 [hep-th].

[175] R.-A. Tripolt, N. Strodthoff, L. von Smekal, and J. Wambach, "Spectral functions from the functional renormalization group," Nucl. Phys. A 931, 790 (2014), arXiv:1407.8387 [hep-ph].

[176] M. Greiner, C. A. Regal, and D. S. Jin, "Probing the Excitation Spectrum of a Fermi Gas in the BCS-BEC Crossover Regime," Phys. Rev. Lett. 94, 070403 (2005), arXiv:cond-mat/0407381 [cond-mat.stat-mech].

[177] H. Biss, L. Sobirey, N. Luick, M. Bohlen, J. J. Kinnunen, G. M. Bruun, T. Lompe, and H. Moritz, "Excitation Spectrum and Superfluid Gap of an Ultracold Fermi Gas," Phys. Rev. Lett. 128, 100401 (2022), arXiv:2105.09820 [cond-mat.quant-gas].

[178] P. Pieri, L. Pisani, and G. C. Strinati, "BCS-BEC crossover at finite temperature in the broken-symmetry phase," Phys. Rev. B 70, 094508 (2004), arXiv:cond-mat/0406099 [cond-mat.supr-con].

[179] T. S. Evans, "N point finite temperature expectation values at real times," Nucl. Phys. B 374, 340 (1992).

[180] N. Wink, "Towards the spectral properties and phase structure of QCD," (2020), 10.11588/heidok.00028503, PhD thesis.

[181] G. Kallen, "On the definition of the Renormalization Constants in Quantum Electrodynamics," Helv. Phys. Acta 25, 417 (1952).

[182] H. Lehmann, "Über Eigenschaften von Ausbreitungsfunktionen und Renormierungskonstanten quantisierter Felder," Il Nuovo Cimento (1943-1954) 11, 342 (1954).

[183] A. L. Fetter and J. D. Walecka, *Quantum Theory of Many-Particle Systems* (McGraw-Hill, Boston, 1971).

[184] S. Weinberg, *The Quantum Theory of Fields*, Vol. 1 (Cambridge University Press, 1995).

[185] A. K. Cyrol, J. M. Pawlowski, A. Rothkopf, and N. Wink, "Reconstructing the gluon," SciPost Phys. 5, 065 (2018), arXiv:1804.00945 [hep-ph].

[186] L. Kades, J. M. Pawlowski, A. Rothkopf, M. Scherzer, J. M. Urban, S. J. Wetzel, N. Wink, and F. P. G. Ziegler, "Spectral Reconstruction with Deep Neural Networks," Phys. Rev. D 102, 096001 (2020), arXiv:1905.04305 [physics.comp-ph].

[187] J. Horak, J. M. Pawlowski, and N. Wink, "Spectral functions in the ϕ^4-theory from the spectral DSE," Phys. Rev. D 102, 125016 (2020), arXiv:2006.09778 [hep-th].

[188] J. Horak, J. Papavassiliou, J. M. Pawlowski, and N. Wink, "Ghost spectral function from the spectral Dyson-Schwinger equation," (2021), 10.1103/PhysRevD.104.074017, arXiv:2103.16175 [hep-th].

[189] T. Gasenzer and J. M. Pawlowski, "Functional renormalisation group approach to far-from-equilibrium quantum field dynamics," arXiv e-prints , arXiv:0710.4627 (2007), arXiv:0710.4627 [cond-mat.other].

[190] J. Berges and G. Hoffmeister, "Nonthermal fixed points and the functional renormalization group," Nuclear Physics B 813, 383 (2009), arXiv:0809.5208 [hep-th].

[191] L. Corell, A. K. Cyrol, M. Heller, and J. M. Pawlowski, "Flowing with the Temporal Renormalisation Group," arXiv e-prints , arXiv:1910.09369 (2019), arXiv:1910.09369 [hep-th].

[192] M. Heller and J. M. Pawlowski, "Causal Temporal Renormalisation Group Flow of the Energy-Momentum Tensor," arXiv e-prints , arXiv:2112.12652 (2021), arXiv:2112.12652 [hep-th].

[193] G. Baym and N. D. Mermin, "Determination of Thermodynamic Green's Functions," Journal of Mathematical Physics 2, 232 (1961).

[194] N. Lerch, L. Bartosch, and P. Kopietz, "Absence of Fermionic Quasiparticles in the Superfluid State of the Attractive Fermi Gas," Phys. Rev. Lett. 100, 050403 (2008), arXiv:0710.1801 [cond-mat.supr-con].

[195] W.-j. Fu and J. M. Pawlowski, "Relevance of matter and glue dynamics for baryon number fluctuations," Phys. Rev. D92, 116006 (2015), arXiv:1508.06504 [hep-ph].

[196] L. Fister and J. M. Pawlowski, "Yang-Mills correlation functions at finite temperature," (2011), arXiv:1112.5440 [hep-ph].

[197] A. Schirotzek, Y.-i. Shin, C. H. Schunck, and W. Ketterle, "Determination of the Superfluid Gap in Atomic Fermi Gases by Quasiparticle Spectroscopy," Physical Review Letters 101 (2008), 10.1103/physrevlett.101.140403.

[198] S. Hoinka, P. Dyke, M. G. Lingham, J. J. Kinnunen, G. M. Bruun, and C. J. Vale, "Goldstone mode and pair-breaking excitations in atomic Fermi superfluids," Nature Physics 13, 943–946 (2017).

[199] L. Pisani, P. Pieri, and G. C. Strinati, "Gap equation with pairing correlations beyond the mean-field approximation and its equivalence to a Hugenholtz-Pines condition for fermion pairs," Physical Review B 98 (2018), 10.1103/physrevb.98.104507.

[200] R. B. Diener, R. Sensarma, and M. Randeria, "Quantum fluctuations in the superfluid state of the BCS-BEC crossover," Physical Review A 77 (2008), 10.1103/physreva.77.023626.

[201] A. Gezerlis and J. Carlson, "Strongly paired fermions: Cold atoms and neutron matter," Physical Review C 77 (2008), 10.1103/physrevc.77.032801.

[202] Q. Chen, "Effect of the particle-hole channel on BCS–Bose-Einstein condensation crossover in atomic Fermi gases," Scientific Reports 6 (2016), 10.1038/srep25772.

[203] H. Tajima, P. van Wyk, R. Hanai, D. Kagamihara, D. Inotani, M. Horikoshi, and Y. Ohashi, "Strong-coupling corrections to ground-state properties of a superfluid Fermi gas," Physical Review A 95 (2017), 10.1103/physreva.95.043625.

[204] A. Bulgac, J. E. Drut, and P. Magierski, "Quantum Monte Carlo simulations of the BCS-BEC crossover at finite temperature," Physical Review A 78 (2008), 10.1103/physreva.78.023625.

[205] A. Behrle, T. Harrison, J. Kombe, K. Gao, M. Link, J.-S. Bernier, C. Kollath, and M. Köhl, "Higgs mode in a strongly interacting fermionic superfluid," Nature Physics 14, 781–785 (2018).

[206] R. Haussmann, W. Rantner, S. Cerrito, and W. Zwerger, "Thermodynamics of the BCS-BEC crossover," Physical Review A 75 (2007), 10.1103/physreva.75.023610.

[207] L. Bartosch, P. Kopietz, and A. Ferraz, "Renormalization of the BCS-BEC crossover by order-parameter fluctuations," Phys. Rev. B 80, 104514 (2009).